



HAL
open science

Molecular Modeling of Interfacial Phenomena

Balázs Fábián

► **To cite this version:**

Balázs Fábián. Molecular Modeling of Interfacial Phenomena. Other. Université Bourgogne Franche-Comté; Budapesti műszaki és gazdaságtudományi egyetem (Budapest), 2018. English. NNT: 2018UBFCD041 . tel-02550813

HAL Id: tel-02550813

<https://theses.hal.science/tel-02550813>

Submitted on 22 Apr 2020

HAL is a multi-disciplinary open access archive for the deposit and dissemination of scientific research documents, whether they are published or not. The documents may come from teaching and research institutions in France or abroad, or from public or private research centers.

L'archive ouverte pluridisciplinaire **HAL**, est destinée au dépôt et à la diffusion de documents scientifiques de niveau recherche, publiés ou non, émanant des établissements d'enseignement et de recherche français ou étrangers, des laboratoires publics ou privés.



PhD thesis prepared under shared supervision at
Carnot Pasteur Doctoral School
University of Bourgogne Franche-Comté
and
George Olah Doctoral School
Budapest University of Technology and Economics

Molecular Modeling of Interfacial Phenomena

Balázs FÁBIÁN

Advisors:

Dr Sylvain Picaud, PhD, HDR (France)

Dr Pál Jedlovszky, PhD, DSc (Hungary)

Internal consultant:

Dr George Horvai (Hungary)

Composition of the Committee :

Professor	László NYULÁSZI	President
Professor	Céline TOUBIN	Reviewer
Professor	Imre BAKÓ	Reviewer
Dr	Jean-Marc SIMON	Member
Dr	Oldamur HOLLÓCZKI	Member
Dr	François-Alexandre MIANNAY	Member
Professor	Sylvain PICAUD	Advisor
Professor	Pál JEDLOVSZKY	Advisor

Acknowledgements

First, I would like to express my sincerest gratitude to my advisors, Dr Sylvain Picaud and Dr Pál Jedlovszky, and consultant Dr George Horvai for their support in my PhD research. Their invaluable guidance helped me at all times both in the research and in the writing of this thesis.

I am deeply grateful to Dr Marcello Sega and to Dr Milán Szóri. Without their precious support it would not have been possible to conduct this research.

I thank my fellow students and friends, in particular Antoine, Bastien, and Saad. They made my time in France an unforgettable journey.

Most importantly, I would like to thank my family: my parents, my brother and above all, my dearest wife for their unwavering love and support.

Contents

Introduction	1
1 Methods of Molecular Simulations	3
1.1 Quantum Mechanics	3
1.2 From Quantum to Classical	5
1.3 Phase Space Representation of Physical Systems	8
1.3.1 The Microcanonical (NVE) Ensemble	9
1.3.2 The Canonical (NVT) Ensemble	10
1.3.3 The Isothermal-Isobaric (NPT) Ensemble	10
1.3.4 The Grand Canonical (μ VT) Ensemble	11
1.3.5 Exploration of Phase Space	11
1.4 Classical Molecular Dynamics	12
1.4.1 Boundary Conditions	12
1.4.2 Calculating the Forces	12
1.4.3 Integrating the Equations of Motion	15
1.4.4 Molecular Dynamics in NVT and NPT Ensembles	16
1.5 Monte Carlo Methods in Classical Mechanics	18
1.5.1 Sampling of the Canonical (NVT) Ensemble	18
1.5.2 Sampling of the Isothermal-Isobaric (NPT) Ensemble	19
1.5.3 Sampling of the Grand Canonical (μ VT) Ensemble	20

2	Interfaces in Computer Simulations	21
2.1	Capillary Wave Theory of Interfaces	21
2.2	Algorithms and the PYTIM Software Package	24
2.2.1	ITIM	25
2.2.2	GITIM	26
2.2.3	Willard and Chandler's Instantaneous Liquid Interface	27
2.2.4	Algorithms to determine phases	28
2.2.5	Algorithms to compute interfacial properties	29
3	Dynamics of Molecules at the Intrinsic Surface	31
3.1	Computational Details	32
3.1.1	Molecular Dynamics Simulations	32
3.1.2	ITIM Analyses	33
3.1.3	Calculation of the Mean Surface Residence Time	34
3.1.4	Calculation of the Diffusion Coefficient and Characteristic Time of Surface Diffusion	35
3.1.5	Calculation of the Velocity Autocorrelation Function	37
3.2	Results and Discussion	38
3.2.1	Surface Diffusion	39
3.2.2	Spatial Correlation between Long-Residing Surface Molecules	43
3.2.3	Hydrogen Bonding at the Intrinsic Liquid Surface	44
3.2.4	Velocity Autocorrelation Function at the Intrinsic Liquid Interface .	48
3.3	Conclusions	50
4	Calculation of Lateral Pressure Profiles	52
4.1	The reciprocal space contribution	54
4.2	The pressure profile of water/vapor interface	57
4.3	Conclusions	62
5	Non-zero Ideal Gas Contribution to the Surface Tension of Water	63

6	How Is the Surface Tension of Various Liquids Distributed along the Interface Normal?	70
6.1	Computational Details	71
6.1.1	Molecular Dynamics Simulations	71
6.1.2	Detection of the Intrinsic Liquid Surface by the ITIM Method	71
6.1.3	Calculation of the Tangential Pressure Profiles	72
6.2	Results and Discussion	72
6.2.1	Intrinsic Tangential Pressure Profiles	75
6.2.2	Contributions of the Individual Molecular Layers to the Surface Tension	78
6.3	Conclusions	81
7	Relation Between the Liquid Spinodal Pressure and the Lateral Pressure Profile at the Liquid-Vapor Interface	83
7.1	Computational Details	85
7.1.1	Molecular Dynamics Simulations	85
7.1.2	Calculation of the Lateral Pressure Profile	87
7.2	Results and Discussion	87
7.3	Conclusion	89
8	Lateral Pressure Profile and Free Volume Properties in Phospholipid Membranes Containing Anesthetics	92
8.1	Computational Details	94
8.1.1	Molecular Dynamics Simulations	94
8.1.2	Calculation of the Lateral Pressure Profile	95
8.1.3	Calculation of the Free Volume Characteristics	95
8.2	Results and Discussion	97
8.3	Lateral Pressure profiles	97
8.4	Free Volume Properties	100
8.5	Conclusion	105

9 Ammonia Clathrate Hydrate As Seen from Grand Canonical Monte Carlo Simulations	107
9.1 Grand Canonical Monte Carlo Simulations	109
9.2 Results and Discussion	111
9.2.1 Occupancy Isotherms	111
9.2.2 Structural Characterization	114
9.3 Conclusions	122
Summary	125
Bibliography	134

Introduction

The desire to unravel the mysteries of nature is as old an endeavour as humanity itself. While the understanding of natural processes was paramount for the survival of our ancestors, the current development of various scientific branches is fueled by the prospect of technological advancement, and human curiosity. The simplest available approach to study naturally occurring phenomena was their direct observation, which paved the way for the myriad of experimental techniques available today. Nonetheless, for either technical or theoretical reasons, several fascinating problems lay well outside the reach of experimental methods. These limitations, amongst others, are the resolution of physically inaccessible length scales or the need for experimentally unfeasible thermodynamic conditions, such as extreme temperature or pressure.

Complementary to the experimental methods is the theoretical approach, where one attempts to investigate a given problem based on its similarities compared to other, already well-understood phenomena. This way of thinking requires abstractions like point-masses, ideal gases, and perfect crystals, that are physically impossible, yet serve as important references for more elaborate concepts.

The third, and most recent possible path of scientific research only became possible with the advent of modern computers, which are capable of performing and storing the results of detailed simulations. With the aid of the simulations, we can experience directly what would happen if we substituted the real system of interest with its theoretical model. Therefore, a suitable model can provide novel insight into the behavior of the original system. Moreover, the result of calculations performed with the model can also have an impact on the development of the theory. This dual role of computer simulations forms a connection between various theoretical predictions and the available experimental results. The relationships between computer simulations and other approaches are succinctly summarized by figure 1, taken from reference [1].

In my PhD thesis I investigate problems related to interfaces and lateral pressure profiles by Molecular Dynamics simulations. As neither of these issues can be adequately

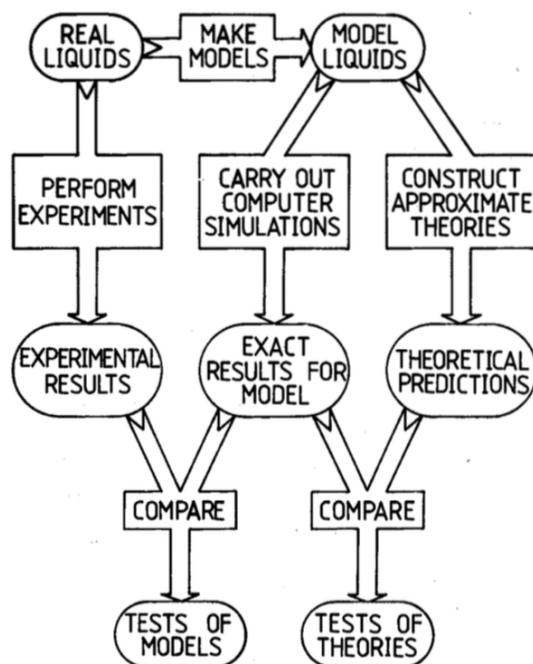


Figure 1. The place of computer simulations in the hierarchy of scientific research. (Image taken from [1])

addressed my experimental methods, they must be tackled by means of computer simulations.

Any thesis dealing with molecules must acknowledge their quantum mechanical nature. Thus, in the first chapter, I establish the classical mechanical approaches based on the quantum description of dynamical systems. In order to achieve this, I first provide a motivation of the central equation of all quantum mechanics, the *Schrödinger equation*. Following this, I show how classical mechanics arises as a limiting case of quantum mechanics. Finally, the classical methods of Monte Carlo and Molecular Dynamics are presented in detail. In the second chapter, I discuss the theoretical bases of intrinsic surface analysis and introduce the PYTIM surface analysis software package that I coauthored. The third chapter concerns the dynamical behavior of molecules at the intrinsic surface. Chapters four and five contain the methodological developments for the calculation of lateral pressure profiles, a quantity that is completely inaccessible with the required resolution. The subsequent chapters discuss applications of the previously developed methods. The last chapter tackles another aspect of binary systems: phase equilibrium without explicit interface. With the help of the well-established method of Grand Canonical Monte Carlo, molecules can be thought of as cross through an imaginary interface, without the need to explicitly have a boundary in the system.

Chapter 1

Methods of Molecular Simulations

1.1 Quantum Mechanics

On the turn of the 20th century, the unanswered conundrums of physics gave rise to the discipline of quantum mechanics, which is the branch of physics that aims to explain phenomena occurring at the smallest scales of nature. One of these, back then unsolved mysteries was the apparent contradiction of the so called *double-slit experiment* [2] with Einstein's explanation of the *photoelectric effect* [3]. While the former established the wave theory of light, the latter demonstrated the corpuscular nature of it. In 1924, Louis de Broglie announced his hypothesis, claiming that not only light, but *all* matter has a wave-like aspect:

$$p = mc = \frac{h}{\lambda} = \frac{h\nu}{c}. \quad (1.1)$$

According to this equation, in the case of a photon, the momentum p – which is equal to the mass m of the particle* times the speed of light c – is inversely proportional to its wavelength λ , or proportional to the ratio of its frequency and the speed of light, ν/c . The constant of proportionality is Planck's constant h . Embracing De Broglie's idea Erwin Schrödinger presented the wave-particle duality at a colloquium talk. After the lecture, Peter Debye, a colleague of Schrödinger remarked that "*This way of talking was rather childish... to deal properly with waves one had to have a wave equation.*" [4] Indeed, following a few weeks of intense research, Schrödinger succeeded in formulating such an equation, the famous *Schrödinger equation* [5]:

$$i\hbar \frac{\partial}{\partial t} |\Psi(\mathbf{r}, t)\rangle = \hat{H} |\Psi(\mathbf{r}, t)\rangle, \quad (1.2)$$

*The photon does not have rest mass, but it possesses a relativistic mass that is proportional to its momentum.

where $\Psi(\mathbf{r}, t)$ is the position and time dependent *wave function*, \hbar is the reduced Planck's constant and \hat{H} is the *Hamiltonian operator*.

"Where did we get that (equation) from? Nowhere. It is not possible to derive it from anything you know. It came out of the mind of Schrödinger.", said famously Richard Feynman [6]. In this spirit, in the following, a short *motivation* is provided that demonstrates key concept behind equation 1.2. The starting point is the Hamiltonian formulation of classical mechanics, which represents the *principle of least action*. In this framework, the system under study is described by a set of canonical positions \mathbf{q} and their conjugate momenta \mathbf{p} . The time evolution of the system is uniquely determined by the Hamiltonian function $\mathcal{H}(\mathbf{q}, \mathbf{p}, t)$ and Hamilton's equations of motion [7]:

$$\frac{d\mathbf{q}}{dt} = \frac{\partial \mathcal{H}}{\partial \mathbf{p}} \quad , \quad \frac{d\mathbf{p}}{dt} = -\frac{\partial \mathcal{H}}{\partial \mathbf{q}}. \quad (1.3)$$

The value of the Hamiltonian $\mathcal{H}(\mathbf{q}, \mathbf{p}, t)$ represents the total energy of the system, and as such – in the absence of explicitly time-dependent terms – can be written as the sum of kinetic and potential energies. For a single degree of freedom, it is

$$\mathcal{H} = T + V \quad , \quad T = \frac{p^2}{2m} \quad , \quad V = V(q). \quad (1.4)$$

Rooted in classical mechanics, this equation does not directly apply to waves, only to point-like particles. Moreover, it looks nothing like equation 1.2. However, the connection becomes clear when we attempt to use a *wave* instead of a point particle. To demonstrate this, we take a simple one dimensional plane wave (*a wave function*) with wavelength λ and frequency ν of the form

$$\Psi(x, t) = C \exp \left(\left[2\pi i \left(\frac{x}{\lambda} - \nu t \right) \right] \right). \quad (1.5)$$

Substituting the physical relationships in equation 1.1 into this, it becomes

$$\Psi(x, t) = C \exp \left(\left[\frac{2\pi i}{h} (px - Et) \right] \right), \quad (1.6)$$

where we used the relation $E = h\nu$. The next step is to devise a method that can determine the momentum and energy of such a wave. As the plane wave is exponential, taking the partial derivative of the plane wave with respect to the position (or time) results in an overall multiplicative factor containing the momentum (or energy) along with some constants:

$$\left(\frac{\partial \Psi}{\partial x} \right)_t = \frac{2\pi i}{h} p \Psi \quad , \quad \left(\frac{\partial \Psi}{\partial t} \right)_x = \frac{-2\pi i}{h} E \Psi. \quad (1.7)$$

This essentially provides us with recipes on how to calculate p and E of such a wave:

$$p \leftrightarrow \frac{\hbar}{2\pi i} \frac{\partial}{\partial x} \quad , \quad E \leftrightarrow -\frac{\hbar}{2\pi i} \frac{\partial}{\partial t}. \quad (1.8)$$

The right-hand sides of the equations are called *operators* of the left-hand side quantities. Noting that the object corresponding to the potential energy is a multiplicative operator, we can create a composite operator that returns the total energy of the system at an instant of time:

$$\hat{H} = -\frac{\hbar^2}{8\pi^2 m} \nabla_i^2 + \hat{E}_p. \quad (1.9)$$

Having \hat{H} act on the wave function, it produces the (kinetic energy + potential energy) times the original function. In the time dependent formulation of the equation (*Time Dependent Schrödinger Equation, TDSE*), this must equal the result of the energy operator acting on the wave function, hence giving us equation 1.2. On the other hand, when the problem is independent of time (*Time Independent Schrödinger Equation, TISE*), the total energy can be expressed as a simple multiplicative factor of the wave function:

$$\hat{H}|\Psi(\mathbf{r}, t)\rangle = E|\Psi(\mathbf{r}, t)\rangle. \quad (1.10)$$

The above equation is the starting point of virtually all of quantum chemistry. In position representation the standard non-relativistic Hamiltonian operator has the following form:

$$\begin{aligned} \hat{H} = & -\sum_I \frac{\hbar^2}{2M_I} \nabla_I^2 - \sum_i \frac{\hbar^2}{2m_e} \nabla_i^2 \\ & + \frac{1}{4\pi\epsilon_0} \sum_{i<j} \frac{e^2}{|\mathbf{r}_i - \mathbf{r}_j|} - \frac{1}{4\pi\epsilon_0} \sum_{I,i} \frac{e^2 Z_I}{|\mathbf{R}_I - \mathbf{r}_i|} + \frac{1}{4\pi\epsilon_0} \sum_{I<J} \frac{e^2 Z_I Z_J}{|\mathbf{R}_I - \mathbf{R}_J|}. \end{aligned} \quad (1.11)$$

The first two operators representing the kinetic energy of the nuclei and the electrons correspond to the classical $T = p^2/2m$ term, while the remaining three are the electron-electron, nucleus-electron and nucleus-nucleus interactions, respectively. Quantum chemical methods based on the molecular Schrödinger equation are called *ab initio*, meaning that they do not make use of empirical models or fitting parameters and only rely on physical constants [8].

1.2 From Quantum to Classical

From a computational viewpoint, this detailed description of a physical system has an inherent drawback: in an N -particle system, besides the $6N$ classical degrees of freedom, we also need to explicitly treat the electronic degrees of freedom, thus severely limiting

the accessible correlation lengths and relaxation times. In the current section I show how the classical picture of the dynamical description of the system arises as a limiting case of quantum mechanics [9], forming an explicit connection between *ab initio* and classical simulations.

As a starting point, we make use of equations 1.2 and 1.11 in the following form:

$$i\hbar \frac{\partial}{\partial t} |\Psi(\{\mathbf{r}_i\}, \{\mathbf{R}_I\}; t)\rangle = \hat{H} |\Psi(\{\mathbf{r}_i\}, \{\mathbf{R}_I\}; t)\rangle, \quad (1.12)$$

$$\hat{H} = - \sum_I \frac{\hbar^2}{2M_I} \nabla_I^2 + \hat{H}_e(\{\mathbf{r}_i\}, \{\mathbf{R}_I\}; t), \quad (1.13)$$

where the dependence on the nuclear $\{\mathbf{R}_I\}$ and electronic $\{\mathbf{r}_i\}$ coordinates is made explicit. Moreover, the last four terms of 1.11 are regrouped into a single $\hat{H}_e(\{\mathbf{R}_I\}, \{\mathbf{r}_i\}; t)$ called the *electronic Hamiltonian*. In general, such a derivation supposes that the exact solution of the stationary electronic Schrödinger equation corresponding to \hat{H}_e ,

$$\hat{H}_e |\Psi(\{\mathbf{r}_i\}; \{\mathbf{R}_I\})\rangle = E_k(\{\mathbf{R}_I\}) |\Psi(\{\mathbf{r}_i\}; \{\mathbf{R}_I\})\rangle, \quad (1.14)$$

is known for the nuclei at positions $\{\mathbf{R}_I\}$, which only enter as parameters into the equation. It is also assumed, that the spectrum of \hat{H}_e is discrete and its eigenfunctions are taken to be orthonormalized:

$$\int \phi_k^*(\{\mathbf{r}_i\}; \{\mathbf{R}_I\}) \phi_l(\{\mathbf{r}_i\}; \{\mathbf{R}_I\}) d\mathbf{r} = \delta_{kl}. \quad (1.15)$$

The knowledge of these *adiabatic*[†] wave functions at every nuclear configuration enables us to expand the total wave function in the form [11]

$$\Psi(\{\mathbf{r}_i\}, \{\mathbf{R}_I\}; t) = \sum_{n=1}^{\infty} \phi_n(\{\mathbf{r}_i\}; \{\mathbf{R}_I\}) \chi_n(\{\mathbf{R}_I\}; t), \quad (1.16)$$

where we consider the χ_n as time-dependent expansion coefficients. However, a more direct route to extract classical dynamics of a quantum mechanical system is taken by directly separating the nuclear and electronic contributions and imposing the classical limit on the nuclei [12]. This separation takes the form

$$\Psi(\{\mathbf{r}_i\}, \{\mathbf{R}_I\}; t) \approx \phi(\{\mathbf{r}_i\}; t) \chi(\{\mathbf{R}_I\}; t) \exp \left[\frac{i}{\hbar} \int_{t_0}^t \tilde{E}_e(t') dt' \right], \quad (1.17)$$

[†]The term *adiabatic* is not to be confused with the adiabaticity in thermodynamics. In quantum mechanics, during an adiabatic process the gradually changing conditions allow the system to completely adapt its wave function. Therefore, a system starting in an eigenstate of the initial Hamiltonian will end up in the corresponding eigenstate of the final Hamiltonian [10].

where \tilde{E}_e is an appropriately chosen phase factor and the nuclear and electronic parts are always normalized separately to unity. Inserting this function into equation 1.12, projecting onto ϕ and χ , and finally imposing the conservation of the total energy $d\langle H \rangle / dt \equiv 0$ yields

$$\begin{aligned} i\hbar \frac{\partial \phi}{\partial t} &= - \sum_i \frac{\hbar^2}{2m_e} \nabla_i^2 \phi + \left\{ \int \chi^* \hat{V}_{n-e}(\{\mathbf{r}_i\}, \{\mathbf{R}_I\}) \chi d\mathbf{R} \right\} \phi \\ i\hbar \frac{\partial \chi}{\partial t} &= - \sum_i \frac{\hbar^2}{2m_I} \nabla_i^2 \chi + \left\{ \int \phi^* \hat{H}_e(\{\mathbf{r}_i\}, \{\mathbf{R}_I\}) \phi d\mathbf{r} \right\} \chi, \end{aligned} \quad (1.18)$$

where \hat{V}_{n-e} contains the potential terms of equation 1.11. Under this separation, both electrons and nuclei move in a time-dependent self-consistently obtained potential, presenting a mean-field description of the system [13]. Using the quantum fluid dynamic representation [14]

$$\chi(\{\mathbf{R}_I\}; t) = A(\{\mathbf{R}_I\}; t) \exp \left[\frac{iS(\{\mathbf{R}_I\}; t)}{\hbar} \right], \quad (1.19)$$

where A is an amplitude and S is a phase, equations 1.18 are rewritten into

$$\begin{aligned} \frac{\partial S}{\partial t} + \sum_i \frac{1}{2M_I} (\nabla_I S)^2 + \int \phi^* \hat{H}_e \phi d\mathbf{r} &= \hbar^2 \sum_I \frac{1}{2M_I} \frac{\nabla_I^2 A}{A} \\ \frac{\partial A}{\partial t} + \sum_i \frac{1}{M_I} (\nabla_I S)(\nabla_I A) + \sum_i \frac{1}{2M_I} (\nabla_I^2 S) A &= 0. \end{aligned} \quad (1.20)$$

Finally, taking the classical limit $\hbar \rightarrow 0$ results in the following equation:

$$\frac{\partial S}{\partial t} + \sum_i \frac{1}{2M_I} (\nabla_I S)^2 + \int \phi^* \hat{H}_e \phi d\mathbf{r} = 0, \quad (1.21)$$

which is isomorphic to the classical mechanical Hamilton-Jacobi [15] equation of motion

$$\frac{\partial S}{\partial t} + \mathcal{H}(\{\mathbf{R}_I\}, \{\nabla_I S\}) = 0, \quad (1.22)$$

where \mathcal{H} is the classical Hamiltonian $\mathcal{H} = T + V$, similarly to equation 1.4. Indeed, upon closer inspection, the second term in equation 1.21 closely resembles the classical kinetic term $\sum_I \mathbf{p}_I^2 / 2M_I$, while the third one represents the potential influencing the nuclear motions:

$$\mathbf{p}_I \equiv \nabla_I S, \quad (1.23)$$

$$M_I \ddot{\mathbf{R}} = - \nabla_I \int \phi^* \hat{H}_e \phi d\mathbf{r} \equiv - \nabla_I V_e^E(\{\mathbf{R}_I\}). \quad (1.24)$$

In this description, the nuclei move along a *classical* trajectory according to an effective

potential V_e^E , called the *Ehrenfest potential*. The exact V_e^E representing the global potential energy surface can be expanded into many-body contributions and truncated [1]:

$$V_e^E \approx V_e^{\text{FF}} = \sum_I v_1(\mathbf{R}_I) + \sum_{I<J} v_2(\mathbf{R}_I, \mathbf{R}_J) + \sum_{I<J<K} v_3(\mathbf{R}_I, \mathbf{R}_J, \mathbf{R}_K) + \dots, \quad (1.25)$$

where v_1 is the effect of external fields, v_2 is the pair potential, and the subsequent terms correspond to higher order many-body interactions. This potential is also called a *forcefield*.

In classical Molecular Dynamics, the sum – for the sake of computational simplicity – is truncated usually after v_2 . Nonetheless, a clever way to account for a part of the higher order terms in equation 1.25 is by defining an *effective potential* that partially incorporates them into the two-body potential:

$$V_{\text{eff}}^{\text{FF}} = \sum_I v_1(\mathbf{R}_I) + \sum_{I<J} v_2(\mathbf{R}_I, \mathbf{R}_J). \quad (1.26)$$

The change from V_e^E to $V_{\text{eff}}^{\text{FF}}$ means that we are no longer working with the explicit electronic degrees of freedom: only their average effect enters through the set of $\{v_i\}$ interaction potentials used. As is seen, constraining the potential to only contain two-body terms amounts to a drastic simplification of the physical system, effectively excluding chemical reactions from the realm of classical simulations.

1.3 Phase Space Representation of Physical Systems

Besides the connection to quantum mechanics another, more traditional viewpoint to discuss classical Molecular Dynamics is provided by statistical mechanics. A pivotal concept needed for this is the notion of phase space [16]. In the phase space every degree of freedom of the physical system under study – the positions and the momenta – are represented as an axis of a multidimensional space. In case of a system composed of N particles, this space has $6N$ dimensions, while the system itself is represented by a single point in this space denoted by Γ .

The instantaneous value of a general observable $\mathcal{A}(\Gamma)$ can be thought of as a function over phase space. During the time evolution of the system, the value of $\mathcal{A}(\Gamma)$ changes, hence, the “macroscopic” value $\mathcal{A}_{\text{macro}}$ of the observable will be the average of the instantaneous value over a sufficiently long interval:

$$\mathcal{A}_{\text{macro}} = \overline{\mathcal{A}(\Gamma(t))} = \lim_{t_{\text{obs}} \rightarrow \infty} \frac{1}{t_{\text{obs}}} \int_0^{t_{\text{obs}}} \mathcal{A}(\Gamma(t)) dt. \quad (1.27)$$

This procedure is called *time averaging*. However, this is not the approach used inherently

by equilibrium statistical mechanics. Depending on the imposed macroscopic conditions on the system, not all of the individual states of phase space might be available for the system to explore: the phase space is partitioned by a so called *partition function* associated to the macroscopic conditions, and the suitable averages are taken over the accessible states. The collection of states available to the system through a given partition function constitute an *ensemble* [17] †. The commonly used statistical mechanical ensembles are presented in the following [1].

1.3.1 The Microcanonical (NVE) Ensemble

The microcanonical (or *NVE*) ensemble is the collection of all microstates where the number of molecules, the volume and the total energy are constant, in other words, the system is *isolated*. In an isolated system where the total energy is conserved, the system can be described by a Hamiltonian without explicit time dependence:

$$\frac{d\mathcal{H}(\mathbf{q}, \mathbf{p}, t)}{dt} = \frac{\partial \mathcal{H}}{\partial \mathbf{q}} \dot{\mathbf{q}} + \frac{\partial \mathcal{H}}{\partial \mathbf{p}} \dot{\mathbf{p}} + \frac{\partial \mathcal{H}}{\partial t} = -\dot{\mathbf{p}}\dot{\mathbf{q}} + \dot{\mathbf{q}}\dot{\mathbf{p}} + \frac{\partial \mathcal{H}}{\partial t} \quad (1.28)$$

by virtue of equation 1.3.

Given a system of constant energy, only the microstates corresponding to this energy are accessible to the system. These individual microstates are postulated to have *a priori* equal probabilities. The partition function "collects" the available states, essentially reducing the need to work in the complete phase space to working with the microstates contained in the ensemble. The quasi-classical microcanonical partition function can be written as

$$Q_{\text{NVE}} = \frac{1}{N!} \frac{1}{h^{3N}} \int \delta(\mathcal{H}(\mathbf{q}, \mathbf{p}) - E) d\mathbf{q}d\mathbf{p}, \quad (1.29)$$

where E is the prescribed total energy, δ is the Dirac-delta function, h is Planck's constant and N is the number of particles. By integrating over the entirety of phase space, Q_{NVE} selects the systems whose positions and momenta produce the desired energy E . The factor $1/N!$ comes from the indistinguishability of similar particles and $1/h^{3N}$ defines the reference measure in phase space. On every ensemble, there is a function called *thermodynamic potential* which is minimized in equilibrium. For the microcanonical ensemble, the relevant thermodynamic potential is

$$-S/k_B = -\ln Q_{\text{NVE}}, \quad (1.30)$$

which is Boltzmann's formula of entropy [18]. According to the equation, the isolated sys-

†The concept of ensembles formalizes the notion of repeating an experiment under the same macroscopic conditions without the ability to control the exact microscopic state of the system.

tem tends to minimize the negative of its entropy – maximize its entropy –, in accordance with classical thermodynamics [19].

1.3.2 The Canonical (NVT) Ensemble

The canonical ensemble represents the available states of a system in contact with a heat bath. As a result of this, the energy is no longer of a constant value, but fluctuates in a manner consistent with the ensemble and the prescribed temperature. In this ensemble, all values of energy are allowed with a probability density corresponding to the Boltzmann distribution:

$$Q_{\text{NVT}} = \frac{1}{N!} \frac{1}{h^{3N}} \int \exp(-\beta \mathcal{H}(\mathbf{q}, \mathbf{p})) d\mathbf{q} d\mathbf{p}, \quad (1.31)$$

where $\beta \equiv 1/k_{\text{B}}T$ is the statistical mechanical temperature. The corresponding thermodynamic potential is proportional to the Helmholtz free energy, A :

$$\beta A = -\ln Q_{\text{NVT}}. \quad (1.32)$$

On the canonical ensemble, the Helmholtz free energy $A \equiv U - TS$ is minimum at equilibrium conditions. It is important to note that although the most likely *microstate* that the system will occupy is the global minimum of the energy, the density of states also increases almost exponentially. The former contribution corresponds to U , while the latter to $-TS$. It is the interplay of these two effects that determines the probability of observing the system at a given energy.

1.3.3 The Isothermal-Isobaric (NPT) Ensemble

The isothermal-isobaric ensemble corresponds to conducting experiments on a system at a given temperature and pressure. The partition function resembles that of the canonical ensemble, only one has to take into account the changing of the volume of the system, which fluctuates in a fashion characteristic of the ensemble:

$$Q_{\text{NPT}} = \frac{1}{N!} \frac{1}{h^{3N}} \frac{1}{V_0} \int \int \exp(-\beta(\mathcal{H}(\mathbf{q}, \mathbf{p}) + PV)) d\mathbf{q} d\mathbf{p} dV, \quad (1.33)$$

where V_0 is a reference volume. The associated thermodynamic potential is proportional to the Gibbs free energy, G :

$$\beta G = -\ln Q_{\text{NPT}}. \quad (1.34)$$

In equilibrium, the combination $G \equiv U + PV - TS$ is minimized.

1.3.4 The Grand Canonical (μVT) Ensemble

The grand canonical ensemble represents the mechanical states of an system that can exchange both energy and particles with a reservoir. As we will see later, this ensemble is particularly well-suited for the study of adsorption processes. The grand canonical partition function is

$$Q_{\mu VT} = \sum_N \frac{1}{N!} \frac{1}{h^{3N}} \exp(\beta\mu N) \int \exp(-\beta\mathcal{H}(\mathbf{q}, \mathbf{p})) d\mathbf{q}d\mathbf{p} \quad (1.35)$$

Of course, a sum has to be used instead of an integral to account for the changing number of particles in the system. The relevant thermodynamic potential is the *grand potential* which does not correspond to any common thermodynamic function, but to the product of the pressure and the volume:

$$-\beta PV = -\ln Q_{\mu VT}. \quad (1.36)$$

1.3.5 Exploration of Phase Space

The approach of calculating averages in statistical mechanics is called *ensemble averaging*: it is the expectation value of the quantity of interest averaged over the possible microstates of the system. In the case of the canonical ensemble, it is

$$\mathcal{A}_{\text{macro}} = \langle \mathcal{A}(\Gamma) \rangle = \frac{\int \mathcal{A}(\Gamma) \exp(-\beta\mathcal{H}(\Gamma)) d\Gamma}{\int \exp(-\beta\mathcal{H}(\Gamma)) d\Gamma}, \quad (1.37)$$

where Γ represents a $d\mathbf{r}d\mathbf{p}$ point in phase space.

If there is only a single trajectory that passes through all of phase space, then each point will be visited by the system during its time evolution. Such systems are termed *ergodic*, and the average of a quantity can be computed either by time averaging (Molecular Dynamics approach, eq. 1.27) or by ensemble averaging (Monte Carlo approach, eq. 1.37) [20]. Ergodicity of a system is often assumed in computations, although there are some systems which are *fundamentally* non-ergodic while others are non-ergodic *in practice*, as there are some bottlenecks in phase space limiting the transition between different areas.

Nonetheless, in the study of a particular, well-localised chemical entity, sampling of the entire phase space is not necessary. When investigating the mechanism of chemical reactions, the ultimate aim is the characterization of the reactants and products, along with the description of the transition state connecting them.

1.4 Classical Molecular Dynamics

The goal of Molecular Dynamics is to generate a representative equilibrium sample of the trajectory of the system in phase space. The relevant properties can be calculated as time averages based on the obtained trajectory.

1.4.1 Boundary Conditions

In order to simulate bulk condensed phases, physical phase boundaries must be avoided. The way to achieve this is by applying *Periodic Boundary Conditions* or *PBC* [21]. The particles making up the system are placed into a space-filling unit cell that is repeated infinitely in every directions. A molecule that leaves through one face of the cell enters through the one opposite to it. This geometry resembles a 3-torus $\mathbb{T}^3 = S^1 \times S^1 \times S^1$.

In order to minimize the artificial effect, the box size should be large enough to prevent a particle from interacting with itself: their interaction should be sufficiently weak to be neglected. A natural extension of this in case of short-ranged interactions is the *minimum image convention* [22], where a particle interacts only with the closest image of all the others. Moreover, the wavelength of possible fluctuations must be compatible with the dimensions of the simulation box. This can cause problems if long wavelengths are expected to be important, for example near the critical point.

1.4.2 Calculating the Forces

The natural time evolution on the microcanonical ensemble can be obtained by using Newton's equations of motion: they arise from the Hamiltonian underlying the ensemble with the help of equations 1.3. For example, for a system containing only water molecules a simple Hamiltonian in the harmonic approximation can be written in the following form [23]:

$$\begin{aligned} \mathcal{H} = & \sum_i \frac{\mathbf{p}_i^2}{2m_i} \\ & + \frac{1}{2} \sum_{\text{bonds}} k_b (b - b_0)^2 + \frac{1}{2} \sum_{\text{angles}} k_\theta (\theta - \theta_0)^2 \\ & + \sum_{i>j} \frac{e_i e_j}{4\pi\epsilon_0 r_{ij}} + \sum_{i>j} 4\epsilon_{ij} \left[\left(\frac{\sigma_{ij}}{r_{ij}} \right)^{12} - \left(\frac{\sigma_{ij}}{r_{ij}} \right)^6 \right], \end{aligned} \quad (1.38)$$

where the various parameters make up the forcefield as demonstrated in equation 1.25. The terms seen in equation 1.38 are the kinetic energy and the potential energies com-

ing from the bonds and angles (*bonded interactions*)[§] followed by the electrostatic and dispersion contributions (*non-bonded interactions*). Applying equations 1.3 results in

$$\frac{d\mathbf{p}_i}{dt} = m\ddot{\mathbf{q}}_i = -\nabla V(\mathbf{q}) \quad , \quad \frac{d\mathbf{q}_i}{dt} = \frac{\mathbf{p}_i}{m_i}. \quad (1.39)$$

According to the first equation, the forces can be calculated as the negative gradient of the potential, while the second one establishes the connection between positions, velocities and momenta.

In an N -particle system, there are $N(N - 1)/2$ distances to be evaluated during the force calculation, so the computation of the force scales as N^2 . This makes force evaluation by far the most time consuming step in Molecular Dynamics. Luckily, there are schemes using *neighbor lists* [24] that effectively reduce the scaling to N by separating the short- and long-range interactions. The long-range part of these interactions change slowly compared to the short ones, so they can be evaluated less frequently.

A particularly important aspect of the force calculation is the handling of the long-range interactions, like Coulomb or dipole-dipole interactions. For potentials decaying slower than r^{-3} , the usual tail correction diverges because the spherical shell around a point increases as r^2 . In order to make the tail correction convergent, the potential must decay faster than r^{-3} . Simply neglecting the long-range contribution would result in significant errors.

The most common technique to take into account the long-range part of the electrostatic interactions is the Ewald summation [25, 26]. The total Coulomb interaction of a system of point charges under the periodic boundary condition can be written as

$$V = \frac{1}{4\pi\epsilon_0} \frac{1}{2} \sum_{\mathbf{n}} \sum'_{i,j} \frac{q_i q_j}{|\mathbf{r}_{ij} - \mathbf{n}L|} = \frac{1}{4\pi\epsilon_0} \frac{1}{2} \sum_{\mathbf{n}} \sum'_{i,j} \frac{q_i q_j}{r_{ij,\mathbf{n}}}, \quad (1.40)$$

where ϵ_0 is vacuum permittivity, q_i are the point charges and $\mathbf{r}_{ij} = \mathbf{r}_i - \mathbf{r}_j$. The vector \mathbf{n} is a repeat vector of the supercell of the simulation and for the sake of simplicity, the box is assumed to be cubic with box length L . In these expressions the $1/2$ factor accounts for double-counting the pairwise interactions, while the $'$ symbol indicates the omission of $i = j$ if $\mathbf{n} = \mathbf{0}$, also known as the *self-interaction* term. The above sum is *conditionally convergent*, meaning that it depends on the order of the summation.

Consider the electric potential generated by a single point charge in space,

$$\phi_i(\mathbf{r}) = \frac{1}{4\pi\epsilon_0} \frac{q_i}{|\mathbf{r} - \mathbf{r}_i|}. \quad (1.41)$$

[§]More complex molecules also can contain proper and improper dihedrals.

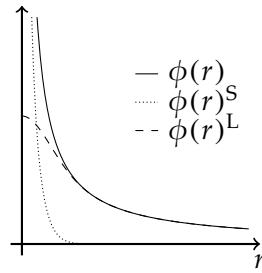


Figure 1.1. Decomposition of the total potential $\phi(r)$ into a short-ranged singular $\phi(r)^S$ and a long-ranged non-singular $\phi(r)^L$ part.

The potential is both long-ranged and singular. With the use of the identity $\text{erf}(x) + \text{erfc}(x) \equiv 1$ [¶], the total electric potential can be decomposed into two terms:

$$\begin{aligned}\phi_i^S(\mathbf{r}) &= \frac{1}{4\pi\epsilon_0} \frac{q_i}{|\mathbf{r} - \mathbf{r}_i|} \text{erfc}\left(\frac{|\mathbf{r} - \mathbf{r}_i|}{\sigma}\right) \\ \phi_i^L(\mathbf{r}) &= \frac{1}{4\pi\epsilon_0} \frac{q_i}{|\mathbf{r} - \mathbf{r}_i|} \text{erf}\left(\frac{|\mathbf{r} - \mathbf{r}_i|}{\sigma}\right),\end{aligned}\quad (1.42)$$

where σ is a parameter determining the ratio of the short- and long-ranged terms. This way, the total potential $\phi(r)$ is decomposed into a short-ranged singular and a long-ranged non-singular part, as seen in figure 1.1. Note that this approach corresponds to a set of screened point charges (short-range) minus the smoothly varying screening distribution (long-range). Following this decomposition, the total Coulomb energy can be written as a sum of three terms:

$$V = V_{\text{dir}} + V_{\text{rec}} + V_{\text{self}}. \quad (1.43)$$

with

$$\begin{aligned}V_{\text{dir}} &= \frac{1}{4\pi\epsilon_0} \frac{1}{2} \sum_{\mathbf{n}} \sum'_{i,j} q_i q_j \frac{\text{erfc}(r_{ij,\mathbf{n}}/\sigma)}{r_{ij,\mathbf{n}}} \\ V_{\text{rec}} &= \frac{1}{4\pi\epsilon_0} \frac{1}{2\pi V} \sum_{\mathbf{m} \neq 0} \sum_{i,j} q_i q_j \frac{\exp(-(\pi\mathbf{m}\sigma)^2 + 2\pi i\mathbf{m} \cdot (\mathbf{r}_i - \mathbf{r}_j))}{\mathbf{m}^2} \\ V_{\text{self}} &= -\frac{1}{4\pi\epsilon_0} \frac{1}{\sigma\sqrt{\pi}} \sum_i q_i^2.\end{aligned}\quad (1.44)$$

The first term is the so called *direct space* contribution associated to $\phi(r)^S$. As the name implies, it is calculated in real space for those neighbors where the $\text{erfc}()$ truncating factor is non-negligible. The periodic long-ranged part of the electric potential $\phi(r)^L$ is no longer

[¶] $\text{erf}(x)$ and $\text{erfc}(x)$ are the error function and the complementary error function, respectively.

singular, thus it can be readily dealt with in reciprocal space producing V_{rec} . To ensure the correct periodicity in reciprocal space, the self interaction cannot be excluded from the sum, hence the unprimed summation. This is corrected for by the presence of V_{self} .

The technique of Ewald summation is already a great improvement over the naive direct sum approach. However, as it scales like N^2 (or $N^{3/2}$ at best) for larger systems, it is still not fast enough for macromolecular simulations. As a solution, *Particle-Mesh Ewald* [27, 28] methods were developed inspired by the particle-mesh approach of Hockney and Eastwood [29]. These methods approximate the long-range interactions by a discrete convolution on an interpolating grid using 3D fast Fourier transform. The accuracy of these schemes also depend on the mesh size and the interpolation scheme, which makes them more complicated to optimize.

1.4.3 Integrating the Equations of Motion

Having determined the forces acting on each particle in the system, Newton's equations of motion can be numerically integrated. There are a handful of criteria that an integrator should satisfy when doing Molecular Dynamics [1]:

- It should be fast and need little memory. In spite of its obviousness, this condition is not the most essential, as the integration step is negligible compared to the force-calculation.
- It should allow the use of a long integration timestep Δt . This requirement is far more important than speed, as a simulation of a given time-interval can be performed with less integration steps, hence less evaluations of the forces. In practice, this is limited by the presence of rapidly changing degrees of freedom resulting from steep potentials, high temperature or small mass of the particles.
- It should follow the exact trajectory as closely as possible. In regimes studied in Molecular Dynamics two trajectories that are initially close will diverge exponentially during the time evolution. Considering the numerical errors as the small initial differences, the calculated trajectory will also diverge exponentially from the exact solution. However, as long as the integrator is generating states of the desired ensemble on longer time scales, it is only necessary to closely match a given trajectory on times scales comparable with the characteristic temporal correlations of the system.
- The integrator should satisfy the conservation laws of energy and momentum as well as be time reversible and *symplectic*. As it was shown in equation 1.28, Newton's

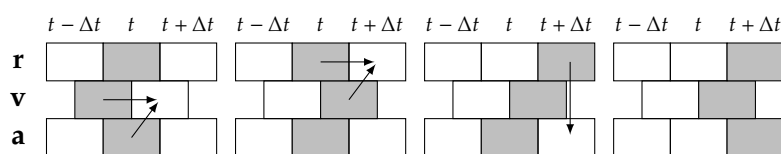


Figure 1.2. The Leap-Frog integrator [1]. The name comes from the fact that the velocities “leap” over the positions and accelerations like frogs leaping over each other’s backs.

equations of motions for a closed system conserve the total energy and are time reversible, so should be the integrator. Moreover, a symplectic integrator preserves the magnitude of volume elements in phase space, which is a necessary requirement for compatibility with energy conservation [20].

One of the most popular algorithms is the so-called *Leap-Frog* integrator [30]. This scheme evaluates the velocities at half-integer steps, which are used to calculate the positions at integer steps. The necessary equations are derived from a Taylor series expansion of the trajectory around the point t :

$$\begin{aligned} \mathbf{r}(t + \Delta t) &= \mathbf{r}(t) + \Delta t \mathbf{v}(t + \frac{1}{2} \Delta t) \\ \mathbf{v}(t + \frac{1}{2} \Delta t) &= \mathbf{v}(t - \frac{1}{2} \Delta t) + \frac{\Delta t}{m} \mathbf{F}(t). \end{aligned} \quad (1.45)$$

The Leap-Frog algorithm is of third order and is both time-reversible and symplectic [31]. The algorithm is illustrated in figure 1.2. The scheme starts with the positions given at time step t and velocities at time step $t - \Delta t/2$. Then, the accelerations are calculated from the previously evaluated forces. The integrator takes the velocities and propels them one step forward, “jumping” over the positions. Finally, the positions also advance one step with the help of the velocities. While the explicit calculation of velocities could be eliminated, it is not advisable to do so, as they are necessary to compute the total energy. To perform simulations in ensembles other than the NVE, the equations of motion are extended with temperature and pressure couplings that are described in the following section.

1.4.4 Molecular Dynamics in NVT and NPT Ensembles

The techniques so far discussed only permit the study of the natural time evolution of a classical system, that is, when the total energy is conserved. However, sometimes it is more convenient to perform simulations in the NVT or NPT ensembles. Classical Molecular Dynamics can be extended to these ensembles by reformulating the Lagrangian of the system [32–34].

The most important method for constant temperature simulations is the *Nosé-Hoover thermostat* [32, 33]. It is obvious from statistical mechanical considerations that the system must be in contact with a heat bath. Under these conditions, the energy is Boltzmann distributed, while the velocities follow the Maxwell-Boltzmann distribution. The imposed, macroscopic temperature is proportional to the average kinetic energy per particle:

$$k_B T = m \langle v_\alpha^2 \rangle, \quad (1.46)$$

where v_α is the α th component of the velocity of a particle with mass m . However, this does *not* mean that the kinetic energy per particle must be constant. In order to sample the canonical ensemble, the instantaneous kinetic temperature T_k should fluctuate around its macroscopic value with relative variance

$$\frac{\sigma_{T_k}^2}{\langle T_k \rangle_{\text{NVT}}^2} = \frac{2}{3N}. \quad (1.47)$$

To ensure the correct statistical distribution, the Lagrangian is extended by the introduction of a thermal reservoir and a corresponding friction term. The resulting Hamiltonian is

$$H = \sum_{i=1}^N \frac{\mathbf{p}_i^2}{2m_i} + U(\mathbf{r}^N) + \frac{p_\xi^2}{2Q} + N_f k T \xi, \quad (1.48)$$

where Q is the effective mass associated to the bath, ξ is the friction parameter and p_ξ is the momentum of the reservoir. The latter two are dynamic variables that enable the calculation of the difference between the instantaneous kinetic temperature and the reference temperature:

$$\begin{aligned} \frac{d^2 \mathbf{r}_i}{dt^2} &= \frac{\mathbf{F}_i}{m_i} - \frac{p_\xi}{Q} \frac{d\mathbf{r}_i}{dt} \\ \frac{dp_\xi}{dt} &= (T - T_0). \end{aligned} \quad (1.49)$$

The mass parameter Q can be related to the characteristic period τ_T of oscillations in the kinetic energy at reference temperature T_0 by

$$Q = \frac{\tau_T^2 T_0}{4\pi^2}, \quad (1.50)$$

providing an intuitive way for choosing the *strength* of the coupling between the system and the surrounding heat reservoir. One possible issue with the Nosé-Hoover thermostat is that it can be non-ergodic even for a simple system, such as a collection of harmonic

oscillators. A possible solution to this is the use of *Nosé-Hoover chains* [35], which correspond physically to a nested set of heat baths, with the system of interest being inside the innermost bath.

Similarly to temperature coupling, a barostat can maintain a constant macroscopic pressure in the system simulated. The *Parrinello-Rahman barostat* [34] allows not only the change of the size of the simulation box, but also to change its shape. This way, the effects of shearing are taken into account. To maintain constant pressure in the simulation box, the box vectors represented by a matrix \mathbf{b} must become dynamic variables that need to obey the

$$\frac{d^2\mathbf{b}}{dt^2} = V\mathbf{W}^{-1}\mathbf{b}'^{-1}(\mathbf{P} - \mathbf{P}_{\text{ref}}) \quad (1.51)$$

relation, where V is the volume of the simulation box, \mathbf{W} is a matrix determining the coupling strength, \mathbf{P} and \mathbf{P}_{ref} are the actual and reference pressures. The equations of motion governing the trajectory of the particles are also changed:

$$\begin{aligned} \frac{d^2\mathbf{r}_i}{dt^2} &= \frac{\mathbf{F}_i}{m_i} - \mathbf{M} \frac{d\mathbf{r}_i}{dt} \\ \mathbf{M} &= \mathbf{b}^{-1} \left[\mathbf{b} \frac{d\mathbf{b}'}{dt} + \frac{d\mathbf{b}}{dt} \mathbf{b}' \right] \mathbf{b}'^{-1}. \end{aligned} \quad (1.52)$$

1.5 Monte Carlo Methods in Classical Mechanics

The aim of Monte Carlo simulations [22] is similar to that of a Molecular Dynamics simulations: the representative sampling of the underlying ensemble. Both being classical forcefield based techniques, they share a large part of their respective toolboxes, such as the periodic boundary conditions and the energy evaluation. However, sampling in Monte Carlo methods is achieved in a fundamentally different way, by generating random configurations with a probability characteristic of the ensemble. The desired observables can be calculated as *ensemble averages* on the obtained sample. The major advantage of Monte Carlo simulations with respect to Molecular Dynamics is the possibility to sample the Grand Canonical and Gibbs ensembles. In these cases, unphysical Monte Carlo moves are performed to enhance the sampling of the underlying ensemble.

1.5.1 Sampling of the Canonical (NVT) Ensemble

In the canonical ensemble the number of molecules, the total volume and the temperature is constant. In this ensemble, the expectation value of an observable can be calculated by equation 1.37. However, by noticing that the kinetic term in the Hamiltonian is a quadratic function of the momenta, the integration over these degrees of freedom can be calculated

analytically [20], and hence equation 1.37 reduces to:

$$\langle \mathcal{A}(\mathbf{r}^N) \rangle = \frac{\int \mathcal{A}(\mathbf{r}^N) \exp(-\beta U(\mathbf{r}^N)) d\mathbf{r}^N}{\int \exp(-\beta U(\mathbf{r}^N)) d\mathbf{r}^N}, \quad (1.53)$$

where the potential energy is denoted by $U(\mathbf{r}^N)$ to avoid confusion with the volume V . The integration is in line with the generation of random configurations: the samples are not connected by temporal relations, so time cannot appear as a variable. A consequence of this is that only time-independent properties can be obtained from Monte Carlo simulations.

Expression 1.53 constituting of generating random configurations with equal probability and weighing them by their Boltzmann factor is still a multidimensional integral that cannot be evaluated by traditional methods. The problem becomes more manageable by switching up the two parts: the configurations are generated with a probability proportional to their Boltzmann factor which is followed by an unweighted averaging. Starting from a suitable initial state, a chain of random configurations is generated by the displacement or rotation of a particle. If the energy decreases, the new state is included in the sample. Otherwise, when the energy increases, the state still can be accepted with the probability of $\exp(-\beta\Delta U)$:

$$P_{\text{acc}} = \min [1, \exp(-\beta\Delta U)] \quad (1.54)$$

This is called *Markov Chain Importance Sampling* [22]. When phase space is sampled by using a Markov Chain with rule 1.54, the individual states will be Boltzmann distributed, as required by the canonical ensemble.

1.5.2 Sampling of the Isothermal-Isobaric (NPT) Ensemble

The importance of Monte Carlo simulation in the NPT ensemble [36] stems from the fact that the majority of real experiments are carried out under conditions of constant pressure and temperature. Instead of the evaluation of the pressure, it requires the calculation of the density, which is not only easier, but far more precise. Therefore, it is useful in determining the (P,T) phase diagram of the systems under study.

In these computations, the volume of the simulation box can be decoupled from the position of the molecules by using fractional coordinates: $s_{\alpha i} = \mathbf{a}_{\alpha}^* \cdot \mathbf{r}_i$ for $\alpha = 1, 2, 3$, where $s_{\alpha i}$ are the fractional coordinates of the i -th molecule, \mathbf{a}_{α}^* are the reciprocal vectors of the box and \mathbf{r}_i is the position vector. In practice, changing the ensemble from NVT to NPT is

as simple as extending the acceptance rule to include volume changes:

$$P_{\text{acc}} = \min \left[1, \exp \left(-\beta \Delta U(\mathbf{s}^N, V) - \beta P \Delta V + N \ln \frac{V_{\text{new}}}{V_{\text{old}}} \right) \right] \quad (1.55)$$

When volume changes are not permitted, the acceptance rule 1.54 is recovered. Thus, an NPT Monte Carlo sampling can be implemented in two steps: performing, with a higher probability, NVT Monte Carlo steps according to the basic acceptance rule and modifying the volume with smaller probability on the basis of the NPT acceptance rule.

1.5.3 Sampling of the Grand Canonical (μ VT) Ensemble

In the previous ensembles, the total number of particles inside the simulations box was kept constant. However, to obtain information on the equilibrium particle numbers in the box, it must be treated as a function of external variables [37, 38]. Contrary to Molecular Dynamics, where the number of particles is typically fixed, such methods are uniquely suited for adsorptions studies [39, 40]. The fixing of the chemical potential amounts to coupling the system to a particle reservoir, where the temperature and the chemical potential of the gas inside the adsorbent and in the reservoir must be equal. Just as in the case of the NPT ensemble, the acceptance rule is modified to produce a sample with a distribution corresponding to the partition function 1.35:

$$\begin{aligned} P_{\text{acc}} &= \min [1, \exp(-\beta \Delta U)] \\ P_{\text{acc,insert}} &= \min \left[1, \exp \left(\ln \frac{V}{\Lambda^3} - \ln(N+1) - \beta \Delta U + \beta \mu \right) \right] \\ P_{\text{acc,delete}} &= \min \left[1, \exp \left(-\ln \frac{V}{\Lambda^3} + \ln(N+1) - \beta \Delta U - \beta \mu \right) \right], \end{aligned} \quad (1.56)$$

with Λ being the *thermal de Broglie wavelength*:

$$\Lambda = \frac{h}{\sqrt{2\pi m k_B T}}. \quad (1.57)$$

The second and third rules correspond to the cases of particle insertion and deletion, respectively. To ensure microscopic reversibility, they must be performed with equal probability.

Naturally, at high enough densities the acceptance of particle insertion moves becomes virtually zero, preventing the grand canonical simulation of dense systems. This and similar obstacles can be overcome by *biased Monte Carlo* techniques, such as the cavity insertion method [41].

Chapter 2

Interfaces in Computer Simulations

2.1 Capillary Wave Theory of Interfaces

Similarly to the case of the bulk liquids, the ultimate goal of the theoretical treatment of liquid/vapor interfaces is to determine the relations between the thermodynamic properties and the microscopic structure of the system under study. The first attempts to study surfaces and the related capillary phenomena relied on crude mechanical models based on a static view of matter [42]. In these early investigations, the density along the direction normal to the surface was thought to be infinitely sharp, represented by a step function. However, a deficiency of this model was quickly pointed out by Poisson [43]: if a molecule within the distance of $\pm d$ of the interface – where d is the range of intermolecular forces – experiences the forces originating from the interface then, under equilibrium conditions, the surface layer cannot be of a uniform molecular density. Thus, the step function was replaced by a continuous function

$$\rho(z) = \frac{1}{2} [\rho_1 + \rho_2 - (\rho_1 - \rho_2)\tanh(2z/L)], \quad (2.1)$$

where ρ_1 and ρ_2 are the densities of the two phases and L is the width of the interface. Nevertheless, because of its conceptual simplicity, the infinitely sharp interface is still employed in continuum frameworks, such as the *Gibbs dividing surface* model. Later, as the continuous description still completely disregarded the molecular motions, it became obsolete with the development of classical thermodynamics and kinetic theory. Therefore, instead of the assumption of random or uniform molecular distributions, correlation functions were introduced. The modern theory of liquids is formulated in terms of these functions that are measures of the conditional probability of occurrence of molecular pairs at specified positions in the system [44].

One possible description of the interfaces is in the context of the *Capillary Wave Theory* [45, 46]. It is a well known fact that the fluid/fluid interfaces are perturbed by long wavelength fluctuations parallel to the surface. A wave with wavelength λ on the surface moves according to [42]

$$qc^2 = g + \frac{\gamma}{m\rho}q^2 = g \left[1 + \frac{1}{2}(aq)^2 \right], \quad (2.2)$$

where q is the wave number, g is the gravitational constant, γ is the surface tension, c is the phase velocity and a is the capillary length. The first term in equation 2.2 represents the long wavelength *gravity waves**, while the second corresponds to the *capillary waves*. The capillary length is the length scale where one regime turns into the other. In the model, the transition between the fluid/fluid phases is locally abrupt with fluctuating height $h(x, y)$ along the surface normal.

The Capillary Wave Theory deals with these fluctuations by means of the intrinsic surface, represented through its Fourier components as

$$z = \xi(\mathbf{R}) = \sum_q \hat{\xi}_q e^{i\mathbf{q}\cdot\mathbf{R}}, \quad (2.3)$$

with $\mathbf{R} = (x, y)$ and the transverse wave vectors $\mathbf{q} = 2\pi(n_x, n_y)/L_x$ where $n_x, n_y = 0, \pm 1, \pm 2, \dots$, which is compatible with the periodic boundary conditions used in molecular simulations. It must be noted that the interface between two fluids is not a well-defined concept as soon as one leaves the continuum description and reaches the molecular level detail[47]. The determination of atoms belonging to an interface is intrinsically dependent on the scale at which the observer probes the interface itself. The level of resolution of the intrinsic surface in Capillary Wave Theory is controlled by q_u , the upper cutoff of the wave vectors. It is evident that qualitatively q_u should be less than the threshold $2\pi/\sigma$, with σ being the molecular diameter. In principle, the lower bound for q is set by the capillary constant a . However, in computer simulations the finite dimensions of the simulation box limit the wave vectors to $q \geq 2\pi/L$, L being the characteristic transverse length of the box.

Along the direction normal to the macroscopic plane of the surface, the microscopic structure of the liquid is described by $\tilde{\rho}(z)$, the so called *intrinsic profile*. The two basic assumptions of Capillary Wave Theory are that $\xi(\mathbf{R})$ and $\tilde{\rho}(z)$ are uncorrelated, and each

*Gravity plays an important role in the creation of a planar surface. The system must be in a strong enough gravitational field to permit the existence of a planar interface, but weak enough not to distort the interfacial gradients.

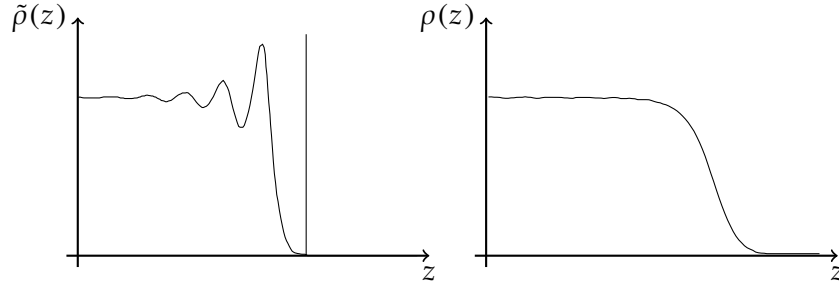


Figure 2.1. Comparison of the intrinsic ($\tilde{\rho}(z)$) and the standard, non-intrinsic density profiles ($\rho(z)$). The latter is obtained from the former by convolution with a Gaussian function.

Fourier component admits uncorrelated Gaussian probabilities with

$$\left\langle |\tilde{\xi}_q|^2 \right\rangle = (\beta\gamma A q^2)^{-1}. \quad (2.4)$$

Under these key assumptions, the shape of the intrinsic density profile is given by

$$\hat{\rho}(z) = \left\langle \frac{1}{A} \sum_{i=1}^N \delta[z - z_i + \xi(\mathbf{R}_i)] \right\rangle. \quad (2.5)$$

It is instructive to compare the intrinsic density profile to the conventional, laboratory frame fixed, *non-intrinsic* density profile,

$$\rho(z) = \left\langle \frac{1}{A} \sum_{i=1}^N \delta(z - z_i) \right\rangle. \quad (2.6)$$

While the latter measures the distance from a fixed external plane, the reference of the intrinsic profile is always taken to be the instantaneous local surface. As a result, the interfacial layer is represented by a δ -function, which is followed by an oscillatory behavior that is reminiscent of the layered structure of fluids near planar walls. In this respect, the non-intrinsic profile can be considered as the intrinsic one smoothed by the instantaneous fluctuations of the position of the intrinsic surface. Schematic comparison of $\tilde{\rho}(t)$ and $\rho(z)$ can be seen in figure 2.1.

Based on the assumption of statistically uncorrelated $\tilde{\rho}(z)$ and $\xi(\mathbf{R})$, the relationship between the sharp intrinsic profile and the non-intrinsic case can be expressed by a convolution with a Gaussian function with width $\Delta_{CW}(q_u) = \sum_q \langle \hat{\xi}_q^2 \rangle$:

$$\rho(z, q_u) = \int \frac{\tilde{\rho}(z', q_u)}{\sqrt{2\pi\Delta_{CW}}} \exp\left(-\frac{(z - z')^2}{2\Delta_{CW}}\right) dz'. \quad (2.7)$$

A prediction of Capillary Wave Theory is that the non-intrinsic density profile of the interface is a Gaussian function: it is the convolution of a Gaussian with a δ -function. This is a fact that can be used to check the applicability of Capillary Wave Theory to the system under study.

2.2 Algorithms and the PYTIM Software Package

The development of computational tools for interfacial analysis closely parallels that of the theoretical advances. The first obstacle was that the Gibbs dividing surface was a completely planar, two-dimensional object that could not be applied in the context of molecular simulations: the mathematical probability of finding a molecule exactly on this surface is zero. The ideal 2D dividing surface is readily extended to the slab of the density profile where the density is between 90% and 10% of that in the bulk phase [48–50]. It was shown subsequently that this definition of the interface leads to systematic errors in the calculated observables [51]. Therefore, there was a dire need for methods that unambiguously identify in computer simulations the molecules that are at the intrinsic surface, which is corrugated by thermally activated capillary waves.

The selected methods presented in the following define the surface on geometrical grounds, and are free from explicit functional forms concerning the intrinsic surface and the density profile. The approach of directly extracting them from molecular simulations enables the comparison with theoretical results. Moreover, such methods readily permit the analysis of various properties of interfacial molecules, such as their orientational and hydrogen bonding preferences or clustering behavior at the intrinsic surface [52–55].

From a computational point of view, determining the interface between fluid phases described at the molecular level is a complicated problem with no unique solution. The experimental nature of many of the available codes represents a severe limitation to the wider diffusion of such kind of analysis. We have developed a python package that implements several algorithms for the analysis of intrinsic interfaces, allowing to analyze the most popular simulation trajectory formats with minimal scripting efforts.

The PYTIM package includes a series of algorithms to identify phases and surfaces or surface atoms, and perform various types of analyses related to interfacial simulations. The main algorithms implemented in PYTIM are: (a) the Identification of Truly Interfacial Molecules [51] (ITIM) for macroscopically planar systems; (b) the Generalized ITIM [56] (GITIM), for arbitrarily shaped systems; (c) the algorithm of Willard and Chandler [57], to compute continuous surfaces based on a smoothed estimate of the atomic volumetric density; (d) an efficient cutoff-based clustering algorithm to distinguish liquid and vapor

phases [58], as well as (e) an improved, density based clustering algorithm for highly miscible systems [59].

All algorithms that identify surface atoms can be used not only to compute the interfacial layer, but also the successive layers beneath it. The algorithms and the peculiarities related to their implementation in PYTIM are briefly reviewed in the next section.

The underlying philosophy of PYTIM is to provide a flexible, extendable and easily scriptable system for the calculation of interfaces and interfacial properties in molecular systems that frees the user from the burden of writing ad-hoc code for different simulation packages. PYTIM is built on top, and extends, the MDAnalysis library [60], which provides the backend for reading different trajectory formats. All algorithms are implemented by making use of the efficient numerical libraries wrapped by `numpy` and `scipy`, resulting in a code, which has a speed comparable to that of a compiled one. The user interface has been designed to be intuitive and straightforward, in the spirit of the python language, and allows to perform the fundamental analyses using just a couple of scripting lines. This task is also facilitated by providing meaningful default values for all options. However, the user has complete control over the details of the algorithms and can quickly perform complex tasks by combining the basic building blocks of PYTIM. In particular, the structure of the interface is meant to encourage the user to experiment with the possibilities offered by combining PYTIM with other libraries and create their own analysis tools.

2.2.1 ITIM

The Identification of Truly Interfacial Molecules algorithm [51] can be loosely described as a molecular version of the popular pinscreen toy. It consists in determining the atoms in contact with a virtual surface made of probe spheres bound to move perpendicularly to the surface plane along test lines, as illustrated by figure 2.2. The present implementation follows that of Jorge et al. [61], which is based on sorting atoms according to their distance from the center of mass of the slab. Then, starting from the furthest atom, one finds which test lines allow a sphere of radius α moving along the line to touch the atom of radius $\sigma/2$. Here, σ corresponds typically to the Lennard-Jones distance parameter [62]. The sorting of N atoms can be performed in $\mathcal{O}(N \log N)$ steps, while finding which of the N_{tl} test lines are within a given radius requires $\mathcal{O}(\log N_{\text{tl}})$ steps using a kd-tree algorithm [63]. Since the test lines are usually 10 times more than the surface atoms (for the algorithm to work accurately), one has typically $N_{\text{tl}} \simeq 10N^{2/3}$, and, in the worst case, $N_{\text{tl}} \simeq 10N$. Therefore, the algorithm scales globally like $\mathcal{O}(N \log N)$. By assuming convergence at a large number of test lines, this method is left with one free parameter, the probe sphere radius α , which sets the scale at which the interface is probed, similarly to the cutoff q_u in the Fourier representation of the surface. Although the presence of one free parameter

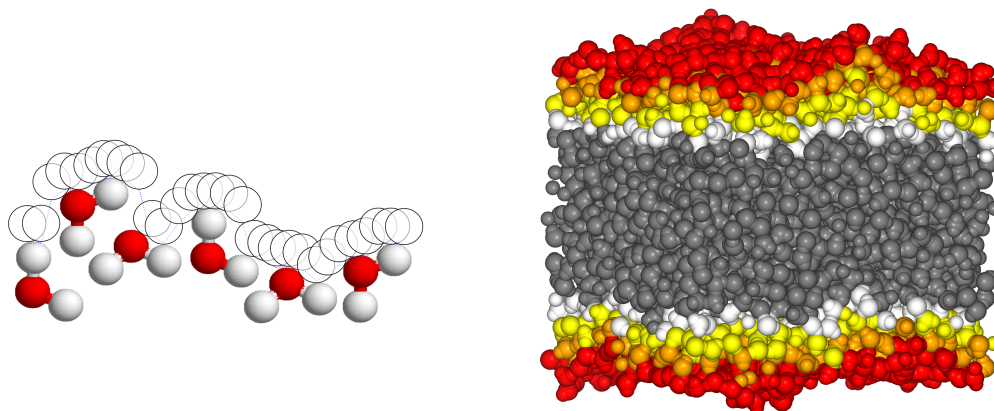


Figure 2.2. Probe spheres in contact with the molecules at the intrinsic surface (left). The first four molecular layers in water/vapor system as determined by ITIM (right).

is inherent in any definition of a surface covering a discrete collection of points, there is undoubtedly a physically reasonable range – in this case, that of α being comparable with the size of the surface molecules – where the obtained results depend only weakly on its value.

2.2.2 GITIM

The constraint of macroscopically flat interfaces poses limit to the applicability of the ITIM method. In the generalization of the algorithm [56] no macroscopic orientation is assumed, therefore it is suitable for the analysis of spherical systems, such as the one seen in figure 2.3. The touching spheres, instead of *raining down* along probe lines, can be thought of as being *inflated* at all points in space, up to their maximum radius α (in which case the surrounding atoms are considered to be interfacial ones) or until they start touching neighboring atoms. This procedure is realized in the GITIM (Generalized ITIM) method using a modification of the α -shapes algorithm [64] that takes into account the excluded volume of the atoms, and implements in its essence a filter of the Delaunay [65] triangulation of atomic positions. In other words, all the triangular faces belonging to those tetrahedra, whose inner touching sphere has a radius larger than α , are considered to be interfacial ones, and so are considered the atoms at the vertices of those triangular faces. Although the original α -shapes algorithm determines all the k -simplices where $k \leq 3$ (tetrahedra, triangles, line segments and points), GITIM stops at the level of tetrahedra. The present implementation of the method can calculate the Delaunay triangulation using the `scipy` library, which uses, in turn, a wrapper to the Quickhull [66] implementation `Qhull`. It can also use the faster `pytetgen` python wrapper to the `tetgen` software [67].

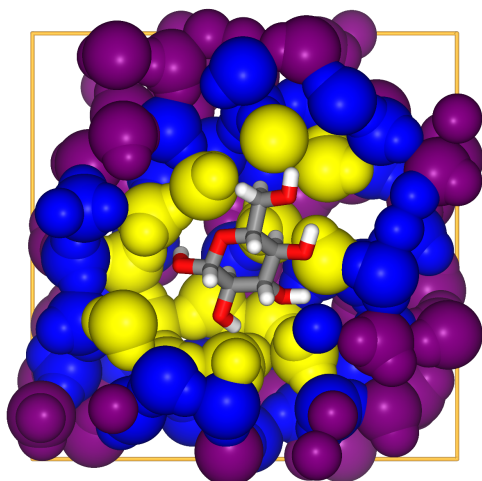


Figure 2.3. A section cut of the three solvation shells of a glucose molecule as identified by the GITIM method.

Both algorithms scale, on average, as $\mathcal{O}(N \log N)$, and in the worst case as $\mathcal{O}(N^2)$, setting, therefore, the scaling of GITIM. When applied to planar interfaces, the method provides results that are practically identical to those of ITIM. Similarly to ITIM, the algorithm has a free parameter, which is the radius α .

2.2.3 Willard and Chandler’s Instantaneous Liquid Interface

This algorithm [57] defines a continuous interface as the isodensity surface of a Gaussian kernel density estimate [68, 69], as illustrated by figure 2.4. A continuous Gaussian density function, with height h_G and width w_G determined by the atomtype, is associated with each atom. Summing over the contributions of all atoms, one obtains a continuous density field, which is usually sampled on a regular grid. The isosurface where the density is in the neighborhood of a given, target density (typically half between the maximum and the minimum) is then used as the definition of the interface itself. In the present implementation, we use both an exact method, by deriving a class from `scipy.stat.gaussian_kde` that implements periodic boundary conditions, and an approximated one that calculates the Gaussian contribution from points closer than $2.5w_G$. We make use of the topologically consistent version [70] of the marching cubes algorithm [71] as implemented in `scikit-image`[72] to extract the isosurface from the kernel density estimate. The computation of the kernel density estimate scales like $\mathcal{O}(NN_g)$. Here, N_g is either the number of grid points in the simulation box (in the exact implementation), or the number of grid points within the sphere of radius $2.5w_G$ (in the approximated implementation). The marching cube algorithm scales like $\mathcal{O}(N_g)$, so that $\mathcal{O}(NN_g)$ is the global scaling. In the most common scenario, the grid spacing is kept constant, independently on the system

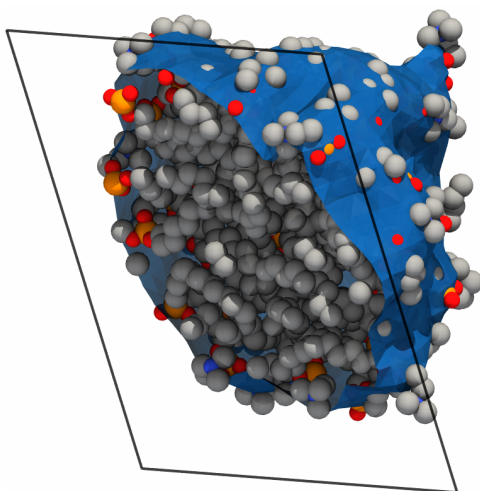


Figure 2.4. The isodensity surface of a solvated dodecylphosphocholine(DPC) micelle as determined by the method of Willard and Chandler.

size, meaning that the computational complexity of the exact implementation scales like $O(N^2)$, while the approximated one scales like $O(N)$.

The algorithm has, in principle, three free parameters: w_G , h_G , and the target density. However, by choosing the target density as half of the maximum one, h_G becomes irrelevant, leaving w_G as the only free parameter. The algorithm does not directly determine surface atoms, but one could define them as those within a certain distance from the isodensity surface. Like GITIM, the Willard-Chandler algorithm can be applied to arbitrary shaped interfaces.

2.2.4 Algorithms to determine phases

To determine the interface between two phases containing the same chemical compound, it is, of course, necessary to assign which atoms belong to which phase. This task is trivial for liquid/vapor interfaces far from the critical temperature, as typical simulated system sizes are small, and often the vapor phase is just empty. For liquid/liquid interfaces, the equivalent condition is that of a perfectly demixing system. In these cases, it is not necessary to perform any particular pre-filtering of the particles before proceeding to the identification of surfaces or surface molecules using any of the above algorithms. One has to be careful, however, that the presence of a single molecule either in the vapor phase or solvated in the opposite phase can jeopardize the whole interfacial determination. In the case of the ITIM analysis of a liquid/vapor interface, this means that a molecule belonging to the vapor phase is identified as a surface atom, artificially widening the surface layer. As the vapor phase grows denser and denser upon approaching the critical temperature,

this problem becomes more serious.

One of the most straightforward ways to separate molecules in the vapor phase from those in the liquid is to group all atoms in clusters and consider the biggest cluster as the liquid phase.

Simple clustering

A simple yet effective strategy is to consider molecules to be in the same cluster if any of their atoms are closer than a chosen cutoff distance [58]. Usually, a reasonable choice for the cutoff value is the position of the minimum after the first peak of the pair correlation function in the bulk liquid phase. This way, the cluster surely includes all atoms belonging to the first solvation shell of the molecules. In this case, the liquid fraction will form a percolating network of connected molecules, whereas the molecules in the vapor phase will be part of smaller, separated clusters.

DBSCAN

The simple cutoff clustering scheme is limited to the case of low temperatures and low miscibilities. At high enough temperatures, for example, the density of the vapor phase can become so high that the whole system percolates using any reasonable choice of cutoff. In this case, it is more effective to look at the local density rather than at the connectivity. The DBSCAN (Density-Based Spatial Clustering of Applications with Noise)[73] is well suited for this task, and has been already employed to study supercritical fluids [74] as well as a 2-phase system of highly miscible fluids [59]. The main idea of the algorithm is to include in a cluster all atoms with overlapping neighborhoods where the density is higher than a given threshold, while treating as outliers the points that are in low-density regions. In Pytim we implemented an approach for the automatic determination of the density threshold, based on a k-mean analysis [75, 76] of the density distribution [59].

2.2.5 Algorithms to compute interfacial properties

Once the surface atoms are determined, these are available through the python interface for further analysis. In the Pytim package, we provide the user with an extendable set of classes for the computation of observables, suited both for the calculation of bulk properties, as well as interfacial ones. In particular, one can combine each observable with the calculation of intrinsic and non-intrinsic density profiles, as well as pair distribution and time correlation functions of atoms *within* the interfacial layers. Based on equation 2.6, the non-intrinsic profile of an observable O across a macroscopically planar interface

is computed in the simulation box-fixed reference frame as

$$\rho_O(z) = \left\langle \frac{1}{A} \sum_i O_i \delta(z - z_i) \right\rangle, \quad (2.8)$$

where A is the surface area, $\langle \dots \rangle$ represents an ensemble average, $\delta(z)$ is the Dirac delta function, and the sum is extended over the set of atoms of interest. This corresponds to the ordinary notion of a density profile, where the bin volume is given by $A\Delta z$. Here the discretized version of the Dirac delta function is $\delta(z) \simeq 1/\Delta z$ if $|z| < \Delta z/2$.

The intrinsic profile, on the contrary, is obtained by referring the position of the particles to the surface capillary waves, obtaining in this way the local, interfacial structure of the fluid without the smearing effect of the capillary waves themselves. If a particle is located at $\mathbf{r}_i = (x_i, y_i, z_i)$ in the box reference frame, we denote the position of the local reference frame on the corrugated surface as $(x_i, y_i, \xi(x_i, y_i))$. In this way, the intrinsic profile of an observable can be written as [77]

$$\rho_O^I(z) = \left\langle \frac{1}{A} \sum_i O_i \delta(z - z_i + \xi(x_i, y_i)) \right\rangle. \quad (2.9)$$

Notice that z can be either negative or positive, depending on the location with respect to the interface, and can be, therefore, thought of as a signed distance.

This concept can be generalized to non-planar macroscopic interfaces by choosing the distance of an atom i located at \mathbf{r}_i from the surface as its distance to the closest surface atom, j . However, care has to be taken in determining the bin width and its sign. Since there is, in the general case, no analytical expression for the area of the iso-distance surfaces, we estimate the bin volume numerically, by using a simple Monte Carlo scheme [56]. The second point one has to take care of is the determination of the sign of the distance that determines whether a point is located below or above the interface. While in the planar case this is straightforward, in the general case we resort to the following. We compute the center of mass of the local environment around the closest surface atom, \mathbf{r}_{cm} , and determine the sign of the distance as the sign of the scalar product $(\mathbf{r}_i - \mathbf{r}_j) \cdot (\mathbf{r}_{cm} - \mathbf{r}_j)$. This choice is made because if both \mathbf{r}_i and \mathbf{r}_{cm} are on the same side with respect to the atom representing the location \mathbf{r}_j of the local surface, one could consider the i -th atom to be within the liquid phase.

Chapter 3

Dynamics of Molecules at the Intrinsic Surface

In spite of the abundance of simulation studies concerning the structural and thermodynamic properties of soft interfaces, little care has been taken to understand their dynamical properties. In fact, although several studies focused on the dynamics of interfacial molecules [78–89], only a handful of them were considering the true, capillary wave corrugated, *intrinsic liquid surface* [86–89]. Therefore, the question of how the surface dynamics of the molecules depend on the intermolecular interactions characteristic of the liquid phase, arises naturally. To address this issue and improve our understanding of the surface dynamics of liquids, we present in this chapter a detailed investigation of the dynamics of the molecules located at the intrinsic liquid-vapor interface of five molecular liquids: carbon tetrachloride, acetone, acetonitrile, methanol, and water. This set of molecules covers a broad range of interactions from weak van der Waals through dipolar yet aprotic to hydrogen bonding ones.

In the following, we focus our attention to the following questions:

- How is the mean surface residence time of the molecules related to the time scale of various dynamical processes of the surface molecules (e.g., diffusion, vibrational motion, H-bond lifetime in the case of hydrogen bonding liquids)?
- How is the diffusion of the molecules within the surface layer related to their diffusion in the bulk liquid phase?
- How different or similar are single molecular motions at the liquid surface and in the bulk liquid phase?

- How, if at all, these dynamical properties of the surface molecules are related to their surface residence?
- How the answers to the above questions depend on the intermolecular interactions acting in the liquid phase?

The computational approach developed in chapter 2 provides a suitable framework to tackle the above points. Moreover, the possibility to investigate the dynamics of interfacial molecules serves as a demonstration of the capabilities of intrinsic analysis.

3.1 Computational Details

3.1.1 Molecular Dynamics Simulations

The molecular dynamics simulations performed here follow those of a preliminary study, where the dynamical behavior of different water models was assessed [89]. MD simulations of the liquid-vapor interface of the five molecular liquids have been performed on the canonical (N,V,T) ensemble. The set of molecules considered corresponds to markedly different intermolecular interactions: while in CCl_4 only van der Waals interaction acts between the molecules, acetone and acetonitrile are characterized by dipolar forces, while methanol and water are strongly hydrogen bonding liquids, with the important difference that in water the H-bonds form a space-filling, percolating network [90, 91], while in methanol they do not [92].

The simulations have been performed at the temperature of 280 K, with the exception of water for which it has been 300 K. The rectangular basic simulation box has consisted of 4000 molecules in every case. The Y and Z edge lengths of the simulation box have been 50 Å whereas the length of the X edge, being perpendicular to the macroscopic plane of the liquid surface, has been varied from 300 to 500 Å, depending on the density of the liquid, in order to ensure a sufficiently wide vapor layer between the two liquid surfaces present in the basic box. This is necessary to avoid artificial interactions between the liquid slabs under the Periodic Boundary Conditions, which have been applied in all directions. The CCl_4 , acetone, and water molecules have been modeled by the OPLS [93], TraPPE [94], and SPC/E [95] potentials, respectively, whereas the acetonitrile and methanol molecules have been described by the potential models proposed by Böhm et al. [96] and by Walser et al. [97], respectively. Our previous study on the surface dynamics of water showed that the results are qualitatively insensitive to the particular choice of the potential model [89].

According to these potential models, the CH_3 groups of acetone and methanol have

been treated as *united atoms*^{*}, whereas the H atoms of the CH₃ group of acetonitrile have been explicitly taken into account. All molecular models used were kept rigid; the internal geometry of the molecules has been kept fixed by means of the SHAKE constraint algorithm [98]. The intermolecular potential energy of the system has been calculated as the sum of the contributions of each molecule pairs, the interaction energy of a molecule pair being equal to the sum of the Coulomb and Lennard-Jones contributions of their respective interaction sites. The long-range part of the electrostatic interaction has been accounted for using the Particle-Mesh Ewald (PME) method in its smooth variant [28].

The simulations have been performed using the GROMACS 5.1 software package [99]. The equations of motion have been integrated by using time steps of 1 fs. The temperature of the systems has been controlled using the Nose-Hoover thermostat [32, 33] discussed in chapter 1. The interfacial systems were created after equilibrating the liquid phase in a basic box, the edges *Y* and *Z* of which being already set to a length of 50 Å. The *X* edge length corresponded to the bulk liquid density and was subsequently increased the *X* edge length to its final value. The systems have been equilibrated for at least 5 ns, after which 2000 sample configurations per system, separated from each other by 1 ps long trajectories, have been collected for the calculation of the diffusion coefficients and surface residence times. Furthermore, 1000 sample configurations, separated by 10 fs long trajectories each, have been saved for evaluating the velocity autocorrelation functions. Finally, for methanol and water an additional set of 1000 sample configurations, now separated by 0.1 ps long trajectories, have been saved for the analysis of the hydrogen bond dynamics.

It should finally be noted that for reference purposes the bulk liquid phases of the systems considered have also been simulated, without the presence of an interface and the vapor phase, in exactly the same way as the corresponding interfacial systems, at the density equal to that of the bulk liquid phase of the corresponding interfacial system.

3.1.2 ITIM Analyses

To determine the molecules located at the macroscopically planar interface, the ITIM method was applied. In the current study a probe sphere of the radius of 2 Å has been used for CCl₄, acetone, and acetonitrile, while that of 1.25 Å for methanol and water, in accordance with the results available in the literature concerning the dependence of the results on the probe size [51, 62, 100]. The radius of the atoms has been defined as half of their Lennard-Jones distance diameter, σ . In determining whether a given molecule belongs to the liquid or to the vapor phase, a cluster analysis algorithm [58] has been

^{*}A united atom can be thought of as a single particle representing the molecular mechanical properties of a group of atoms.

employed to filter out molecules from the vapor phase. Thus, two molecules have been defined as being in contact with each other if the distance between any of their atoms was smaller than a predefined cutoff value. Two molecules belong to the same cluster if they are connected through a chain of molecules in contact. The largest cluster found in the simulation box is regarded as the liquid phase itself, whereas the molecules belonging to any other cluster are regarded as being part of the vapor phase [58, 101]. The cutoff distance used in defining the contact position of the molecules has been set equal to the smallest of the minima positions of the atom-atom partial pair correlation functions, excluding the ones involving OH hydrogens. This way, the cutoff values of 8.0, 5.0, 3.6, 5.8, and 3.5 Å have been used for CCl₄, acetone, acetonitrile, methanol, and water, respectively. Test lines have been arranged in a 100 × 100 grid along the YZ plane corresponding to the macroscopic plane of the liquid surface. Thus, two neighboring test lines have been separated by 0.5 Å from each other.

3.1.3 Calculation of the Mean Surface Residence Time

The survival probability of the molecules at the liquid surface, $L(t)$, can simply be defined as the conditional probability, that a molecule that belongs to the surface layer at time t_0 remains at the liquid surface until time $t_0 + t$. In order to distinguish between the cases when a molecule leaves the surface layer permanently, and when it only leaves it temporarily due to an oscillatory move and returns to the surface immediately, a departure from the surface between t_0 and $t_0 + t$ is conventionally allowed if the molecule returns within a short time window of Δt . However, since the 1 ps length of the trajectories separating two subsequent sample configurations is already larger than/comparable to the time scale of these oscillations, here we have not allowed such departures of the molecules from the liquid surface: once a molecule has not been found in the surface layer, it has been regarded as having left the surface. Since the departure of the molecules from the liquid surface is governed by first-order processes, the $L(t)$ survival probability is of exponential decay, and, in the simplest case, it can be fitted by the function $\exp(-t/\tau_{\text{surf}})$, where τ_{surf} is the mean residence time of the molecules at the liquid surface. However, since some of the molecules leave and rejoin the surface layer due to a fast oscillatory move, the $L(t)$ data can be fitted by the sum of two exponentials, which have two characteristic time values: the first of which corresponds to this fast oscillation, while the second one to the *permanent* departure of the molecules from the surface.

3.1.4 Calculation of the Diffusion Coefficient and Characteristic Time of Surface Diffusion

The self-diffusion coefficient, D , of homogeneous, isotropic liquids can be estimated by comparing the second moment of the probability distribution function $P(\mathbf{r}, t; \mathbf{r}_0)$ of finding a molecule at time t at position \mathbf{r} , given that at an initial $t = 0$ its position was \mathbf{r}_0 with that of the solution of the Fokker-Planck equation:

$$\frac{\partial}{\partial t} P(\mathbf{r}, t; \mathbf{r}_0) = D \nabla^2 P(\mathbf{r}, t; \mathbf{r}_0). \quad (3.1)$$

At the practical level, this is usually done by sampling directly the second moment of the distribution, that is, the mean-square displacement (MSD) of the molecules within the time t , by using

$$\text{MSD} = \langle (\mathbf{r}_i(t_0 + t) - \mathbf{r}_i(t_0))^2 \rangle \quad (3.2)$$

along the trajectory of the system simulated. In equation 3.2, $\mathbf{r}_i(t_0)$ and $\mathbf{r}_i(t_0 + t)$ stand for the position vectors of the i th molecule at time t_0 and $t_0 + t$, respectively, and the brackets $\langle \dots \rangle$ denote ensemble averaging. The solution of the Fokker-Planck equation in homogeneous, isotropic systems is a Gaussian function:

$$P(\mathbf{r}, t; \mathbf{r}_0) \propto \exp\left(\frac{-(\mathbf{r}_i(t_0 + t) - \mathbf{r}_i(t_0))^2}{kDt}\right), \quad (3.3)$$

and its second moment is simply $\text{MSD} = kDt$, where k is a parameter related to the dimensionality of the diffusive motion, its value being 2, 4, and 6 in the case of one-, two-, and three-dimensional diffusion, respectively. Therefore, the diffusion coefficient can be calculated through the Einstein relation [1]

$$D = \frac{\text{MSD}}{kt} \quad (3.4)$$

from the steepness of a straight line fitted to the MSD vs t data. This fitting should, however, be done in a limited time range in order to ensure that the molecules exit the ballistic regime and lose correlation. In the present study, the time range above 2 ps has turned out to be sufficient for this purpose in every case. One should, of course, make sure that in the presence of periodic boundary conditions the continuous trajectory of particles is reconstructed before calculating the MSD. It should also be noted that in calculating the diffusion coefficient of the molecules within the surface layer, each molecule contributes to the MSD only in the time interval it is part of the surface layer.

In confined systems, which lack both homogeneity and isotropy, there are several

important changes to be taken into account in these equations:

- The scalar diffusion coefficient D becomes a position-dependent diffusion tensor $\mathbf{D}(r)$.
- A full Fokker-Planck equation is needed, that includes the gradient of the position-dependent diffusion coefficient.
- The solution for the probability distribution is not anymore equation 3.3, and as a consequence, the MSD will also not have the simple form of kDt .

Two examples for the application of this formalism are the investigation of the diffusion of water in the proximity of a protein [78] and in the interstitial space between two periodic copies of a lipid bilayer [85]. Since here we are interested in the diffusion within the surface layer, and we update the statistics for the MSD only when a molecule is in that layer, the problem can be expressed in terms of an effective Fokker-Planck equation with reflecting boundary conditions along the layer normal, between $X = X_0$ and $X = X_0 + L_{\text{eff}}$, where L_{eff} is the effective width of the interfacial layer. In this case, the diffusion tensor takes the form $\mathbf{D} = \text{diag}(D_{\perp}, D_{\parallel}, D_{\parallel})$, where D_{\perp} and D_{\parallel} are the diffusion constants along the macroscopic surface normal axis, X , and within the macroscopic plane of the surface, YZ , respectively. Here, we further assume that within the layer itself, the diffusion tensor is independent of the position. The solution can therefore be expressed in terms of marginal probabilities to diffuse parallel to the layer or perpendicular to it along X (while still being located in the layer).

The MSD for the lateral diffusion still possesses the Einstein form, $4D_{\parallel}t$, whereas the expression for the perpendicular component, once averaged over the initial position X_0 , is the series [82]

$$\frac{1}{L_{\text{eff}}} \int \langle (X - X_0)^2 \rangle dX_0 = \frac{L_{\text{eff}}^2}{6} - L_{\text{eff}}^2 \sum \frac{16}{(2n+1)^4 \pi^4} \exp\left(-D_{\perp} t \left[\frac{(2n+1)\pi}{L_{\text{eff}}}\right]^2\right). \quad (3.5)$$

Because of the presence of boundaries, the asymptotic perpendicular (average) MSD is a constant $-L_{\text{eff}}^2/6$ – rather than a linearly growing quantity, and the effective perpendicular diffusion coefficient, D_{\perp} , has to be estimated via a best fit of the sampled MSD to equation 3.5. The series is quickly converging due to the presence of the $1/n^4$ term, and only few terms are needed to obtain an accurate approximation. It is interesting to note that since both the series in equation 3.5 and the Taylor expansion of the exponential function are absolutely convergent, it is possible to exchange the two sums and obtain for small times that the (average) perpendicular MSD is $2D_{\perp}t$. This seems like recovering the result of

the Einstein equation. However, this approximation holds only for times small enough for the diffusing particles not to feel the presence of the boundaries.

The characteristic time of the diffusion can be defined as the time after which the positions visited by a molecule follow a Gaussian distribution with the width of L_m , $\sqrt{A_m}$, and $\sqrt[3]{V_m}$ in the case of one-, two-, and three-dimensional diffusion, respectively. Of course, this definition can only be applied when the diffusion can indeed be regarded as a random walk, the motion is not biased by any external force [89, 102]. Here L_m , A_m , and V_m , stand for the length, area, and volume per molecule in the one-, two-, and three-dimensional cases. Thus, the characteristic time of the (two-dimensional) diffusion of the molecules within the surface layer of the liquid phase, τ_D , can be given as

$$\tau_D = \frac{A_m}{4D_{\parallel}}, \quad (3.6)$$

where

$$A_m = \frac{2YZ}{\langle N_{\text{surf}} \rangle}, \quad (3.7)$$

$\langle N_{\text{surf}} \rangle$ stands for the average number of the surface molecules in the system, and the factor 2 in the numerator of equation 3.7 accounts for the two liquid surfaces present in the simulation box. It is important to point out that the parallel and perpendicular diffusion coefficients in the first molecular layer are still calculated in the global reference frame and not along the local tangent plane or normal direction to the curved interface. Besides the added complexity of projecting the motion on the local reference frame, this approach raises a conceptual problem related to the fact that the surface is changing in time, and it would be difficult to avoid an ambiguous definition of the distance traveled along the surface itself.

3.1.5 Calculation of the Velocity Autocorrelation Function

The velocity autocorrelation function of the molecular center of mass, \mathbf{v}^{cm} , defined as

$$\Psi(t) = \frac{1}{N} \left\langle \sum_i \mathbf{v}_i^{\text{cm}}(t_0 + t) \mathbf{v}_i^{\text{cm}}(t_0) \right\rangle, \quad (3.8)$$

where N is the total number of molecules, is a useful tool for understanding the dynamical behavior of single molecules, providing information on which time scales the memory of the initial velocity of a particle is lost due to interaction with neighboring molecules. The typical traits of the velocity autocorrelation functions in dense fluids are an initial parabolic decay, related to the average force acting on the molecule, followed by a steep decay imposed by collisions with nearest neighbors. At relatively high densities,

the velocity autocorrelation function can become negative because of strong repulsion from the cage formed by the neighboring molecules, and its long time behavior can be characterized by hydrodynamics in the form of an algebraic decay to zero. The velocity autocorrelation function carries similar information on the dynamics of the molecules as the MSD. In practical terms, however, the short-time dynamics is more easily accessible from the velocity autocorrelation function, and for this reason we introduce a velocity autocorrelation function perpendicular to the surface, $\Psi_{\parallel}(t)$, which is the analogue of the perpendicular MSD of the first layer:

$$\Psi(t)_{\parallel} = \frac{1}{N(t_0)} \left\langle \sum_i^{N(t_0)} \mathbf{v}_{\parallel i}^{\text{cm}}(t_0 + t) \mathbf{v}_{\parallel i}^{\text{cm}}(t_0) \theta_i(t_0 + t, t_0) \right\rangle, \quad (3.9)$$

where $N(t)$ is the number of molecules in the first layer at time t and the function $\theta_i(t_2, t_1)$ is equal to 1 if molecule i has been residing continuously in the first layer from time t_1 to t_2 and zero otherwise.

3.2 Results and Discussion

The profiles of the molecular number density, ρ , of the five systems simulated along the macroscopic surface normal axis, X , are shown in figure 3.1, along with those of the first molecular layer at the liquid surface. The different positions of the surface region along the X axis reflect the different sizes of the molecules and the different densities of the liquid phases considered. As is clearly seen, the X range of the surface layer largely overlaps with the constant density region of the system, while the intermediate density part of the overall profile is far from being fully accounted for by the contribution of the surface layer in every case. In other words, the definition of the surface of the systems in the usual, nonintrinsic way as the region of intermediate density would indeed cause a misidentification of a surprisingly large number of molecules, ultimately leading to the analysis of an ad hoc set of molecules rather than that of the real, capillary wave corrugated, intrinsic liquid surface layer [51, 103]. To avoid such erroneous identifications, the intrinsic surface analysis methods of chapter 2 must be used. Furthermore, as it is expected based on the capillary wave theory [104], the density profile of the surface layer is of Gaussian shape in every case. The Gaussian functions fitted to the profiles are also shown in figure 3.1. The width parameter of the Gaussian function fitted to such a density profile, δ , can serve as a measure of the width of the surface layer.

The $L(t)$ survival probabilities of the molecules at the liquid surface are presented in figure 3.2. In the following, this function is used to define the set of the longest residing 10% of the surface molecules in every sampled configuration in order to analyze to what

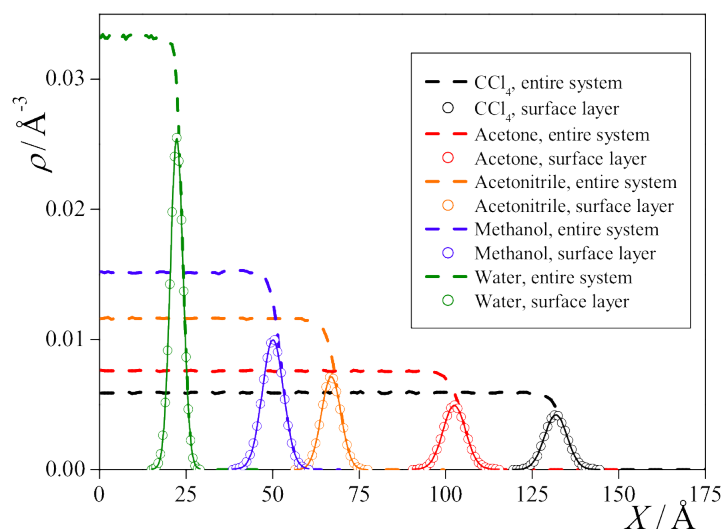


Figure 3.1. Molecular number density profiles of the simulated systems. The Gaussian curves fitted to the molecular layers are shown by solid lines.

extent the properties of these long residing molecules differ from those of the entire set of the surface molecules. We could fit the $L(t)$ data well with the sum of two exponential functions in every case, as shown also in the figure. The characteristic times of these two processes are collected in table 3.1. The shorter of these two characteristic times never exceeds 2.5 ps, indicating that the corresponding process is probably related to the fast librational motion of the molecules. This process usually does not lead to the permanent departure of the molecules from the surface layer, instead, they only leave the surface layer due to this librational oscillation but come back shortly thereafter due to the same mechanism. On the other hand, the second process corresponds to the real departure of the molecules from the surface layer. The characteristic time of this second process, τ_{surf} , falls in the range of about 15-25 ps, being the largest for CCl_4 and being rather similar in the other four systems considered. The obtained values of τ_{surf} set the time scale of all molecular processes occurring in the surface layer of the corresponding liquid phase. For example, $\tau_{\text{D}} < \tau_{\text{surf}}$ means that a molecule feels, within its lifetime at surface, the constraints of the interface. Thus, in these cases, it is meaningful to talk about diffusion at the surface.

3.2.1 Surface Diffusion

The perpendicular and parallel MSDs of the molecules within the surface layer are shown as a function of time in figure 3.3. For comparisons, the full, three-dimensional MSDs, obtained in the corresponding bulk liquid phases, are shown in the inset of figure 3.3. The D_{\perp} and D_{\parallel} diffusion coefficient values corresponding to all surface molecules as well

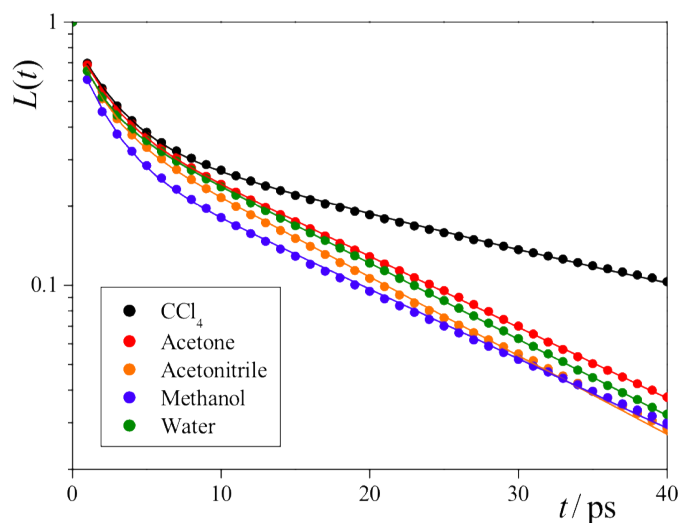


Figure 3.2. Survival probability of molecules within the interfacial layer of their liquid phase, shown on a semi-logarithmic scale. The sum of the two exponential fitting functions are shown by solid lines.

Table 3.1. Characteristic times (ps) of the various molecular processes occurring at the surface layer of liquids and the dipole moment μ of the models used. The values in parentheses correspond to the initial, rapidly decaying process of leaving the interface. (For the definition of τ_{HB} , see section 3.2.3.)

system	τ_{surf}	τ_D	τ_{HB}	μ
CCl_4	26.2 (2.5)	7.20		0.00
acetone	16.1 (2.0)	2.97		2.50
acetonitrile	14.5 (1.8)	3.39		4.14
methanol	16.4 (2.0)	4.34	2.27	2.28
water	15.0 (1.7)	4.11	1.36	2.35

as to the longest residing 10% of them, and also the bulk phase diffusion coefficients, obtained from the best fits of equation 3.5 (D_{\perp}) and equation 3.4 (D_{\parallel} and bulk phase D), are collected in table 3.2. Furthermore, the characteristic times of the parallel diffusion within the surface layer, τ_D , obtained through equation 3.6, are included in table 3.1.

The characteristic diffusion time, τ_D , is considerably smaller than the mean surface residence time, τ_{surf} , indicating that the surface diffusion of the molecules can *indeed* be meaningfully discussed, as it occurs well within the time scale of the molecules remaining part of the surface layer. The $\tau_{\text{surf}}/\tau_D$ ratio is the largest for the strongly dipolar but aprotic molecules, which can diffuse faster than the hydrogen bonding ones, as their diffusion is not hindered by the H-bonds formed with their neighbors (the dipole moment of the molecular models used are also collected in table 3.1). This ratio, on the other hand, is

as small for CCl_4 as for methanol and water, primarily due to the large characteristic time of its surface diffusion. The finding that the $\tau_{\text{surf}}/\tau_D$ ratio decreases, in general, with decreasing dipole moment is in clear accordance also with the earlier finding of Duque et al. that this ratio is around 1 for the totally apolar Lennard-Jones system [86]. It might seem surprising that contrary to Duque et al., we obtained a considerably larger τ_{surf} than τ_D value for the apolar CCl_4 molecules. However, it should be emphasized that although the CCl_4 molecules do not have a net dipole moment, their atoms still bear non-negligible fractional charges, and hence they, unlike the Lennard-Jones spheres, still interact via a considerable multipolar interaction. /

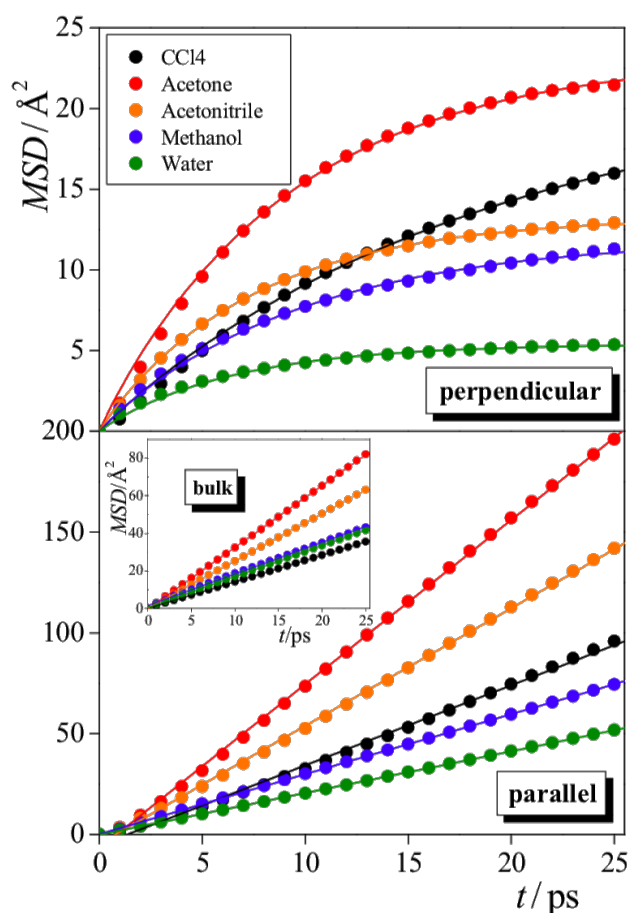


Figure 3.3. Survival probability of molecules within the interfacial layer of their liquid phase, shown on a semi-logarithmic scale. The sum of the two exponential fitting functions are shown by solid lines.

As is seen from table 3.2, the surface residence time of the individual molecules is not correlated with their surface mobility, as the calculation of D_{\perp} and D_{\parallel} for all the surface molecules or for only the longest residing 10% of them results in very similar

Table 3.2. Diffusion coefficients within the surface layer ($\text{\AA}^2/\text{ps}$) and inside the bulk liquid. The values in parentheses correspond to the longest residing 10% of the surface molecules.

		CCl ₄	acetone	acetonitrile	methanol	water
surface	D_{\perp}	0.70 (0.73)	1.52 (1.66)	1.09 (1.18)	0.74 (0.76)	0.51 (0.51)
	D_{\parallel}	0.99 (1.03)	2.04 (2.19)	1.46 (1.56)	0.74 (0.76)	0.52 (0.53)
bulk	D	0.24	0.55	0.42	0.28	0.27

values. Further, it is also found that the molecules diffuse considerably faster at the liquid surface, in both the parallel and perpendicular directions, than inside their bulk liquid phase. A similar relation was found earlier by Duque et al. for the diffusion of the Lennard-Jones system [86]. This is understandable in light of the fact that at the liquid surface the molecules lose a part of their attractive interactions with respect to the bulk liquid phase. It can also be well understood that the ratio of the surface and bulk diffusion coefficients is the smallest in water, since it is known that water molecules adopt such orientations at the liquid surface that they can preserve about 75% of their hydrogen bonds as compared to the bulk liquid phase [51, 105]. On the other hand, it is somewhat surprising that this ratio is substantially larger for methanol than water, considering that methanol molecules can be aligned at the surface in such a way that they preserve all of their hydrogen bonds. The reason for this enhanced surface diffusion for methanol could be related to the hindrance of the mobility of the bulky methyl groups inside the liquid phase due to their accumulation around each other [106–108]. This hindrance can be dramatically reduced at the liquid surface by the very strong preference of the molecules for sticking their methyl groups straight out to the vapor phase [109].

Besides the D_{\perp} value itself, the fitting of the perpendicular MSD data by equation 3.5 also yields the effective width of the surface layer, L_{eff} . The values of L_{eff} are collected in table 3.3 along with the width parameter of the surface layer density profiles, δ , as obtained for the five liquids considered. These values indeed correlate well with each other, their ratio falling between about 1.4 and 1.8 in every case. Integration of the Gaussian-shape density profile of the surface molecules (figure 3.1) in the distance range of the width L_{eff} around its center reveals that L_{eff} represents an effective width that includes 83-92% of the surface molecules for the different system, as detailed in table 3.3.

Figure 3.4 shows the MSD of the surface molecules along the macroscopic surface normal axis, X , as a function of time on two different time scales, normalized by the mean surface residence time, τ_{surf} , and by the characteristic time of surface diffusion, τ_D , respectively. The obtained MSD deviates downward from linearity not only on the real

Table 3.3. Parameters describing the width of the surface layer in the simulated systems. x_{eff} is the fraction of surface molecules within L_{eff} .

	CCl ₄	acetone	acetonitrile	methanol	water
$L_{\text{eff}}(\text{\AA})$	11.5	11.8	8.8	8.4	5.6
$\delta(\text{\AA})$	6.5	6.6	5.6	6.2	3.7
x_{eff}	0.92	0.93	0.89	0.83	0.88

time scale up to 25 ps but also on the scale of the surface residence time of the molecules in every case. More precisely, the simulated data points start deviating from linearity at around 20-40% of τ_{surf} . This finding indicates that although the molecules can seemingly freely diffuse also along the macroscopic surface normal in a non-negligible fraction of their surface lifetime, they start feeling the presence of the boundaries still well within their lifetime at the liquid surface, τ_{surf} . On the other hand, as seen on the right side of figure 3.4, the MSDs are indeed linear up to τ_D , the characteristic time scale of the lateral surface diffusion. To interpret this result, however, we have to emphasize that τ_D is the upper limit of the time range within which the molecules can still have memory of their initial position, for example, within this interval, they might still not exhibit an uncorrelated random walk. The observed linearity of the perpendicular MSD can thus either be related to the fact that within this time scale, the molecules do not feel yet the constraint of being in the surface layer and diffuse freely along the macroscopic surface normal, or it can also be an artifact of the limited time window. Further investigation of the possible physical meaning of the observed linearity of MSD within this time scale can be done by analyzing the velocity autocorrelation function of the surface molecules, which is presented in subsection 3.2.4.

3.2.2 Spatial Correlation between Long-Residing Surface Molecules

The diffusion of the molecules that stay at the liquid surface for unusually long times did not turn out to be markedly different from that of the other surface molecules in any case. To further investigate whether long surface residence times of certain molecules simply occur randomly or they are related to certain properties of these molecules, we investigate how strongly the positions of these molecules are correlated with each other at the liquid surface. In other words, we address the question whether long-residing surface molecules are distributed randomly at the liquid surface, or they form relatively dense patches, leaving large empty spaces between them. For this purpose, we have projected the centers of the longest residing 10% of the surface molecules to the macroscopic plane of the surface, YZ , and have calculated the Voronoi cells [110–112] around each of these projections. If these projections are randomly distributed, the area (A) of the Voronoi cells

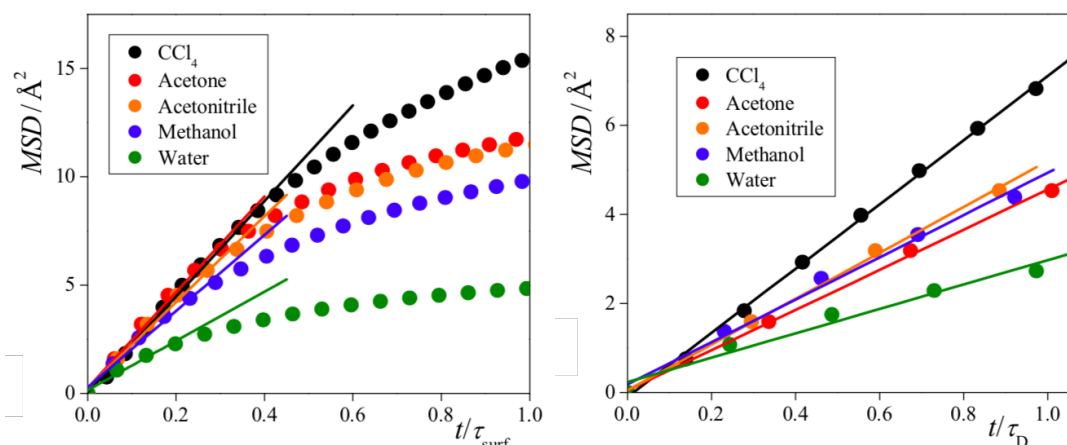


Figure 3.4. One dimensional MSD of the interfacial molecules along the macroscopic surface normal, X , shown on the time scales corresponding to the characteristic times of the surface residence time (left), and the lateral diffusion of the molecules (right).

is expected to follow approximately a gamma distribution [113, 114]

$$P(A) = aA^{\nu-1} \exp(-\nu\rho A) \quad (3.10)$$

where ν and ρ are free parameters, while a is a normalization factor. On the other hand, in the case of correlated arrangement of these projections the $P(A)$ distribution deviates from equation 3.10, exhibiting a long tail of exponential decay at the large area side of its peak [115]. The $P(A)$ Voronoi cell area distributions are shown in figure 3.5 as obtained in the five systems simulated together with their best fits by equation 3.10. The exponential decay of all these data sets (transformed to a linear decrease by the use of a logarithmic scale) as well as the deviation from equation 3.10 is clearly seen from the figure in every case. This finding indicates that the long-residing molecules are distributed in a correlated way at the liquid surface: they prefer to stay in the vicinity of each other. It is also apparent that this correlation is the weakest for the hydrogen bonding liquids, in particular, for water, and strongest for CCl_4 .

3.2.3 Hydrogen Bonding at the Intrinsic Liquid Surface

In this subsection we address the point how the properties of the hydrogen bonds are affected by the liquid surface in the two H-bonding liquids considered, methanol and water. Also, to further study the question how unusually long surface residence time is related to other properties of the molecules, we compare the properties of the H-bonds of the longest residing 10% of the surface molecules with those of all surface molecules.

The average lifetime of a hydrogen bond can be defined in a similar way as the

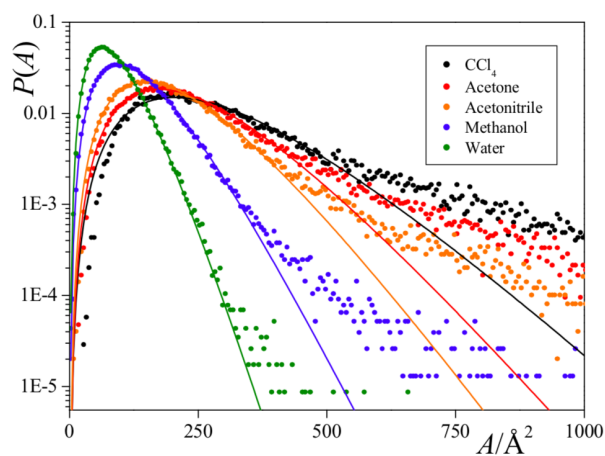


Figure 3.5. Distribution of the area of the Voronoi cells of the projections of the surface molecules onto the macroscopic plane of the interface, YZ . To emphasize the exponential nature of the decaying distributions, the data is plotted on a semi-logarithmic scale. The solid lines are the best fits of equation 3.10.

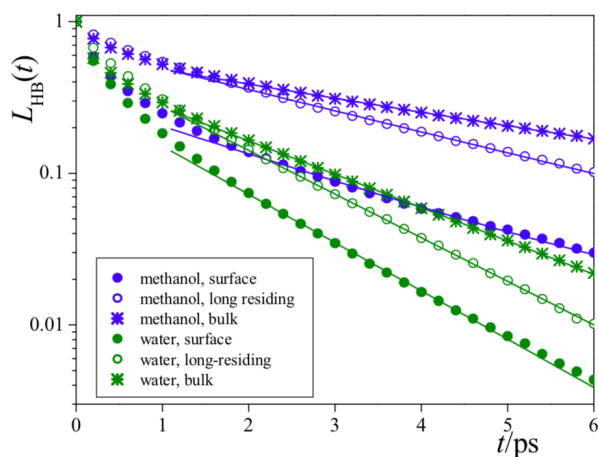


Figure 3.6. Survival probability of the hydrogen bonds. To emphasize the exponential decay, the data are shown on a semi-logarithmic scale. The best fits of the long time part of the data are shown by solid lines.

Table 3.4. Average number of hydrogen-bonded neighbors of a molecule and average interaction energy of a hydrogen bonded pair (kJ/mol) in various regions of the simulated systems.

system		$\langle n_{\text{HB}} \rangle$			$\langle U_{\text{HB}}^{\text{pair}} \rangle$		
		total	in-layer	off-layer	total	in-layer	off-layer
methanol	interfacial	1.86	1.34	0.52	-20.58	-20.75	-20.16
	long-residing	1.81	1.49	0.32	-20.68	-20.87	-19.97
	bulk	1.92			-20.30		
water	interfacial	3.30	2.42	0.88	-19.22	-19.60	-18.17
	long-residing	3.17	2.50	0.67	-19.34	-19.74	-17.84
	bulk	3.79			-18.53		

mean surface residence time. Thus, the survival probability of a H-bond, $L_{\text{HB}}(t)$, is the probability that a H-bond existing at time t_0 will persist up to the time $t_0 + t$. Again, the breaking of a H-bond is a process of first-order kinetics; hence, $L_{\text{HB}}(t)$ is a function of exponential decay. Therefore, the mean H-bond lifetime, τ_{HB} , can simply be estimated by fitting the function $\exp(-t/\tau_{\text{HB}})$ to the simulated $L_{\text{HB}}(t)$ data. Similarly to the survival probability at the liquid surface, $L(t)$, the short time part of $L_{\text{HB}}(t)$ can also deviate from the exponential decay; this transient part of the $L_{\text{HB}}(t)$ data, covering the first 0.1-0.5 ps of the time range, has thus been left out from the exponential fit (see figure 3.6). The τ_{HB} values corresponding to the H-bond between two surface molecules, included also in table 3.1, are typically an order of magnitude smaller for both H-bonding liquids considered than the mean surface residence time of the molecules. Therefore, the H-bonds formed specifically by surface molecules can be distinguished from those involving also bulk phase molecules, and thus their properties can indeed be meaningfully discussed. It should be noted that the average lifetime of a H-bond at the liquid surface is considerably shorter than in the bulk liquid phase for both H-bonding liquids considered: the τ_{HB} values obtained in the bulk liquid phase of methanol and water have turned out to be 5.22 and 2.01 ps (the corresponding surface values being 3.22 and 1.54 ps), respectively. On the other hand, the surface residence time of the molecules is not related to the lifetime of their H-bonds, as the τ_{HB} values corresponding to the H-bonds between two long-residing surface molecules are 3.28 ps in methanol and 1.52 ps in water.

The average number of the H-bonds formed by a surface molecule, $\langle n_{\text{HB}} \rangle$, and the average interaction energy of such a H-bonded molecule pair, $\langle U_{\text{HB}}^{\text{pair}} \rangle$, are collected and compared to the respective bulk phase values in table 3.4. Values corresponding specifically to the longest residing 10% of the surface molecules are also included in the table. Furthermore, the $\langle n_{\text{HB}} \rangle$ and $\langle U_{\text{HB}}^{\text{pair}} \rangle$ values corresponding to the interfacial molecules are

also decomposed according to the location of the H-bonding partner molecule, namely, whether it also belongs to the surface layer or not. As is clear from the data, the liquid surface does not have a considerable influence on the H-bonding structure of the molecules in methanol. The average number of the H-bonded neighbors of a surface methanol molecule is only 3% less than that of a bulk phase one, and correspondingly, the interaction energy of such a molecule pair agrees within 0.3 kJ/mol for molecule pairs being at the liquid surface and in the bulk liquid phase. By contrast, interfacial water molecules have, on average, about 15% less H-bonded neighbors than the bulk phase ones, while their pair interaction energy is, on average, 0.7 kJ/mol deeper than in the bulk liquid phase. This difference can be related to the preferred surface orientations of these molecules: both of these molecules can easily be oriented at the liquid surface in such a way that three of their tetrahedrally aligned H-bonding directions are turned flatly toward the bulk liquid phase [51, 103, 109]. Since methanol molecules have only three H-bonding directions, they can efficiently maintain all of their H-bonds even at the macroscopically flat liquid surface by sticking the fourth of the tetrahedrally aligned electron pairs of their O atom, the O-CH₃ bond, straight out to the vapor phase [109]. On the other hand, in water this fourth electron pair around the O atom also represents a H-bonding direction. Therefore, alignments of the surface water molecules in which three of the H-bonding directions are turned flatly inward involves the "sacrifice" of the fourth of these directions, which is then turned straight toward the vapor phase [51, 103]. All four H-bonding directions can only be turned toward the bulk liquid phase at strongly curved portions of the liquid surface [51, 52, 103], such as at the tips of the ripples of the molecularly wavy surface.

The energy loss corresponding to the fewer number of H-bonding neighbors is partly compensated by a certain ordering of the H-bonding arrangement of the water molecules at the liquid surface, which results, on average, in somewhat stronger H-bonds at the surface than in the bulk phase (see table 3.4). The observed small, about 4% strengthening of the H-bonds at the surface of water is also in accordance with earlier results [106, 116, 117]. It is interesting to note that although the bulk phase H-bonds are, on average, slightly weaker in water and are about the same strength in methanol than the interfacial ones, H-bonds live considerably longer in the bulk phase than at the interface of both liquids. This finding is again in accordance with earlier claims that the strength and lifetime of the H-bonds are independent from each other [117, 118]. Instead of their strength, the shorter lifetime of the surface H-bonds can be explained by the enhanced mobility of the surface molecules, as compared to that of the bulk phase ones (see table 3.2), due to their lack of attractive interactions at the vapor side of the interface.

When comparing the properties of the long-residing molecules with those of all the surface molecules, it is seen that long residing molecules form, on average, slightly, by

3-4% less H-bonds than all the surface molecules. When decomposing these numbers into the values corresponding to in-layer and off-layer H-bonds, it turns out that the average number of H-bonding neighbors of the long residing surface molecules within the surface layer is somewhat larger (11% in methanol and 3% in water), while that of their non-surface H-bonding neighbors is considerably smaller (38% in methanol and 25% in water) than the values corresponding to all surface molecules. The observed increase of the number of in-layer H-bonds is in accordance with our previous finding that long residing molecules prefer to stay in the vicinity of each other. However, the most striking feature of the long residing surface molecules is clearly that they form much less hydrogen bonds with the subsurface molecules than the value corresponding to all of the surface molecules. This fact can also explain their long stay in the surface layer. Namely, having fewer off-layer H-bonded neighbors, these molecules are better separated from the subsurface region and hence cannot leave the surface as easily as the other ones.

3.2.4 Velocity Autocorrelation Function at the Intrinsic Liquid Interface

In figure 3.7 the autocorrelation function of the in-plane molecular center of mass velocity for the molecules belonging to the first layer, $\Psi_{\parallel}(t)$ is shown, along with the autocorrelation function $\Psi(t)$ of the molecular center of mass velocity in the corresponding bulk liquid phases for comparison. The common trait is that the in-plane velocity of surface molecules is always more correlated during the initial, rapid decay, which takes place within the first 0.1-0.3 ps. Of all considered liquids, only CCl_4 and acetone show, in the bulk, no presence of the cage effect, and $\Psi(t)$ is always positive, whereas $\Psi_{\parallel}(t)$ is considerably larger at all times, with values clearly different from zero, also for time lags where $\Psi(t)$ has already vanished. In the case of acetonitrile, the two autocorrelation functions are different both qualitatively and quantitatively from each other, as the negative part of $\Psi(t)$ is not present anymore in $\Psi_{\parallel}(t)$. The latter function decays smoothly, resembling a memory-less process. In both methanol and water the two autocorrelation functions share some common features, namely an oscillation at 0.25 and 0.13 ps, respectively, which is the signature of hydrogen bonding [119]. In methanol, however, the in-plane correlation function of the surface molecules is again always positive, and the cage effect, which characterizes the bulk phase dynamics, is not present within the surface layer. While methanol molecules retain the majority of their hydrogen bonds at the liquid surface, the outward pointing arrangement of the CH_3 groups at the surface results in a much less crowded environment of the molecules. As a consequence, the cage effect disappears, in accordance with the strongly enhanced surface diffusion discussed in subsection 3.2.1. Water is the only case in which the in-plane correlation of the surface molecules becomes negative, showing that the hydrogen bond network is strong enough to influence the

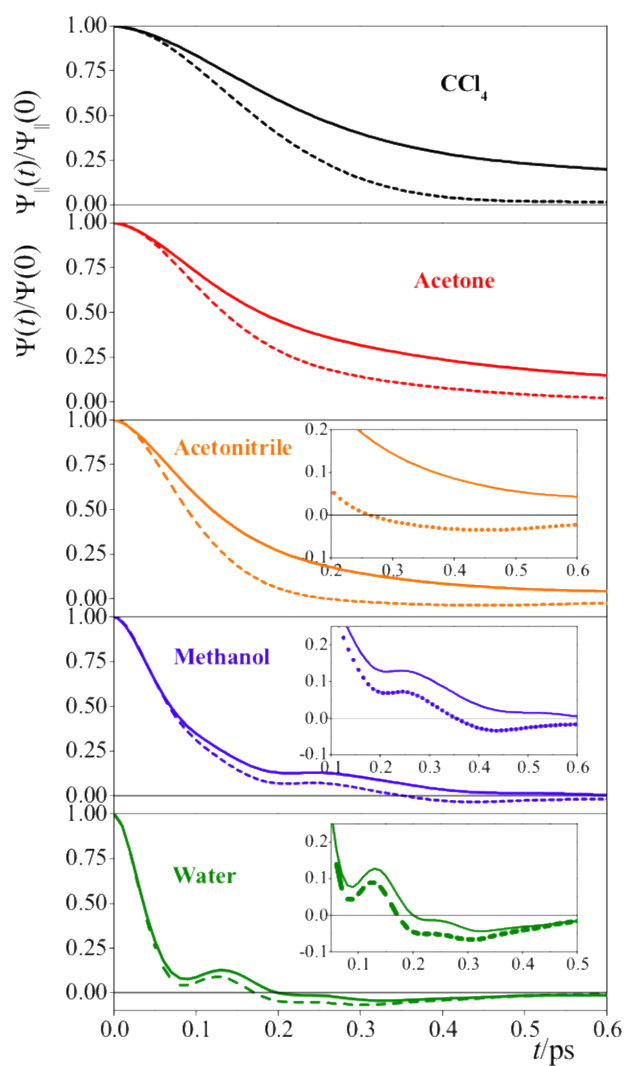


Figure 3.7. Normalized velocity autocorrelation function of the centers of mass of the molecules at the surface and in the bulk liquid phase. The insets show the relevant parts of the curves on an enlarged scale.

dynamics of the water molecules even within the surface layer. These results suggest that water behaves in a rather unique way in this respect, as no such behavior is seen for the other liquids considered. Still, the in-plane velocity correlation of the surface molecules is always larger than its bulk counterpart in the region of positive values and smaller in that of negative ones, showing therefore a larger mobility of the molecules and a less pronounced cage effect, which again explains the larger diffusion coefficient in the surface, with respect to that in the bulk. This effect is, however, less pronounced here than in the case of methanol, where caging is completely eliminated at the liquid surface.

3.3 Conclusions

In this chapter, we have analyzed the single particle dynamical properties of the molecules in the first molecular layer of five molecular liquids, ranging from apolar through aprotic dipolar to hydrogen bonding ones. The analysis of the molecular residence times in the first layer has shown that the dynamics of escape from the first layer is dictated by two characteristic time scales. The first, fast process of escape takes place on the time scale of about 2 ps for all liquids considered here and is most likely representative of molecules leaving the layer for short times due to librational motions. The other process dominates after the first few picoseconds and takes place on the much longer scale of 15-25 ps and is found to be considerably larger than the characteristic time of in-layer diffusion and hydrogen bond lifetime (for methanol and water), which are therefore meaningful observables for this set of molecular liquids and thermodynamic points. We investigated the diffusion in the first layer by sampling both the mean-square displacement and the velocity autocorrelation function of the molecular centers of mass. The mean-square displacement parallel to the macroscopic plane of the interface and perpendicular to it shows two qualitatively different behaviors, namely, the common Einstein linear dependence of bulk systems (for the parallel diffusion), and saturation behavior that fits extremely well with the diffusion between two reflecting walls [78, 82]. The diffusion coefficients estimated from these two separate fits are markedly different from the diffusion coefficient obtained in the bulk liquid phase, showing, in all cases, a much – typically 3-4 times – larger surface diffusion with respect to the bulk. The analysis of the in-plane velocity autocorrelation function confirmed this finding, showing that at the picosecond scale molecules at the surface are in all cases more free to move than in the bulk. At the surface, excluding the case of water, no trace of the cage effect is found, if this was present in the bulk. In those cases, which did not present a cage effect even in the bulk liquid phase, sizable correlation with the initial velocity is found at time lags, where the bulk counterpart shows no correlation any more. The analysis of the spatial distribution of the long-residing surface molecules has revealed that they are clearly characterized by some

degree of clustering. The analysis of the hydrogen-bonded neighbors has shown that in contrast to water, methanol is retaining practically all of its hydrogen-bonded neighbors at the liquid surface. This result might be surprising in the light of the much higher diffusion coefficient of the methanol molecules found at the liquid surface than in the bulk liquid phase; however, it is consistent with the pronounced tendency of methanol to expose the bulky CH_3 group to the vapor side of the interface [109], which also helps eliminating the cage effect. This shows that the main factor in building up the internal friction for bulk methanol is the presence of the CH_3 groups rather than that of the hydrogen bonds (which, unlike in liquid water, do not form a percolating network in bulk methanol [92]). The opposite happens in water, where the dynamics of the molecules is almost completely dominated by the hydrogen bond networking, both in the liquid phase and at its surface, resulting also in its very high surface tension, with respect to all other molecular liquids considered here. In conclusion, the analysis of single particle dynamical properties at the intrinsic liquid surface has proven to be very informative on the microscopic dynamics at liquid/vapor interfaces, showing that mass transport properties are markedly different at the surface, with respect to the bulk. In fact, these differences are surprising, considering the fact that from the structural point of view the first molecular layer is not so much different from the subsequent ones. The 2-4-fold increase in mobility at the surface draws a picture of a much more fluid surface layer, sharing some traits with those of rarefied fluids in the case of non-hydrogen-bonding liquids, which can have important implication for diffusion-limited reactions occurring at interfaces.

Chapter 4

Calculation of Lateral Pressure Profiles

Calculating the profiles of various physical quantities, such as mass, charge, or electrostatic potential, is a standard approach used in computer simulations in order to characterize inhomogeneous systems including fluid (soft) interfaces, membranes, micelles or other self-associates. While some of these profiles have been routinely calculated in the past decades, the importance of determining pressure profiles is only recently being recognized, for example, for the calculation of the mechanical properties of macromolecules [120–123]. Furthermore, conjectures related to pressure profiles also play a key role in the possible explanations of several phenomena. Thus, for instance, it was proposed by Cantor that the molecular mechanism of anesthesia is related to the alteration of the lateral pressure profile inside the cell membrane [124], and Imre et al. claimed that the spinodal pressure of a liquid phase can be extracted from the lateral pressure profile obtained at the liquid-vapor interface of the same system at the same temperature [125]. Experimental verification or falsification of these conjectures is an extremely challenging task as it requires the measurement of the mean lateral pressure across interfaces, or macromolecules at atomic resolution, a task that is rarely accomplished (see, for example, reference [126]). On the other hand, these hypotheses can be efficiently investigated using computer simulation techniques. The aforementioned conjectures are investigated in chapters 7 and 8.

Still, the calculation of pressure profiles in computer simulations is complicated by the fact that it requires the local determination of a quantity that is inherently non-local. More precisely, a local pressure tensor cannot, in general, be uniquely defined. Instead, it can only be given up to a divergence-free second rank tensor in a path dependent form. Several integration paths, such as the Irving-Kirkwood [127] and Harasima [128] paths,

were shown to provide comparable profiles [129]. Besides its conceptual simplicity, the Irving-Kirkwood path has the advantage of leading to a formula for the local pressure that gives access to both the normal and lateral components of the virial, distributed homogeneously along the paths connecting pairs of particles. On the other hand, while the Harasima path allows one to calculate only the lateral components of the pressure tensor, these are concentrated at the positions of the particles. In other words, a certain amount of the total lateral pressure is associated with each particle, making the calculation of the lateral pressure profile straightforward and computationally efficient [130, 131].

Another serious technical problem in calculating pressure profiles in charged systems is how to take into account the long range correction term of the electrostatic interaction. It is now well-established that neglecting this correction to the energy and forces can lead to significant systematic errors. The method of reaction field correction [132], which uses the dielectric constant of the continuum beyond a suitably chosen cutoff sphere, is unsuitable for strongly inhomogeneous systems such as the interfaces. However, the Ewald summation [25] can still be used in such systems. The contribution of its correction term to the pressure profile was derived by Sonne and coworkers for the Harasima path [130]. They also showed that potentials that are not strictly pairwise additive, such as the correction term of the Ewald summation, cannot be used in combination with the Irving-Kirkwood profile. However, because of its poor scaling properties, the use of the plain Ewald summation is prohibitive for systems with a large number of charges.

This problem can be overcome using a method based on the Fast Fourier Transform (FFT), such as mesh Ewald methods [27–29]. In the following, the local pressure from the reciprocal space contribution of mesh Ewald methods is derived.

For approaches based on the Irving-Kirkwood path, where it is not possible to take into account non-pair additive potentials, several authors have opted for running the simulations using their method of choice for the evaluation of long range contributions, but considering cutoff electrostatics for the purpose of evaluating the local pressure (see, for example, Refs.[120, 133, 134]). This is usually done by re-running the simulation and using cutoff values that are larger than usual, thus reducing the artifacts. However, in order to reach a precision of the order of 1 bar, cutoff values larger than 2.5 nm must be used (see figure 7 in Ref. [135]). Sonne et al. [130] showed that the pressure profile calculated using the Irving-Kirkwood approach and a cutoff radius of 2 nm is qualitatively similar to the one calculated using the Harasima path with long-range electrostatic contributions, although with an indetermination of roughly 100 to 200 bar, which makes it only a qualitative test.

In this chapter, we show how the correction term of the smooth Particle Mesh Ewald

[28] (sPME) method can be taken into account in calculating lateral pressure profiles using the Harasima path in an efficient way that does not alter the scaling of the long-range correction calculation. The method itself is presented in subsection 4.1 and the pressure contributions associated to particles are compared with those obtained with a reference, simple Ewald calculation. In subsection 4.2 we apply the method to the example of the water/vapor interface.

4.1 The reciprocal space contribution

We start by decomposing the instantaneous pressure tensor \mathbf{P} , as customary, into the ideal gas and virial (Ξ) contributions,

$$\mathbf{P}V = \sum_i m_i \mathbf{v}_i \otimes \mathbf{v}_i - 2\Xi. \quad (4.1)$$

The difference between lateral and normal components of the pressure tensor plays an important role for interfaces, as it describes the surface tension, and it locally can be written as

$$\gamma(z) = P_N - P_T(z), \quad (4.2)$$

where we have chosen $P_N = P_{zz}$ and $P_T = (P_{xx} + P_{yy})/2$. This formula applies only to planar interfaces. In addition, we will assume – as is customary – that it applies also in the presence of capillary waves, as long as the surface remains macroscopically flat. The presence of curved interfaces introduces additional difficulties in the definition and calculation of the surface tension [42, 129, 136]. Here we note that while P_N is constant throughout the system to ensure mechanical stability [42], Ξ_{zz} is not.

In the Ewald sum, the reciprocal space contributions to energy and virial are expressed as sums over the reciprocal lattice vectors \mathbf{m}

$$\begin{aligned} U^{\text{rec}} &= \sum_{\mathbf{m} \neq 0} \frac{1}{2\pi V} f(\mathbf{m}^2) S(-\mathbf{m}) S(\mathbf{m}) \\ \Xi_{\mu\nu}^{\text{rec}} &= \frac{1}{V} \sum_{\mathbf{m} \neq 0} \frac{1}{2\pi V} f(\mathbf{m}^2) g_{\mu\nu}(\mathbf{m}) S(-\mathbf{m}) S(\mathbf{m}) \end{aligned} \quad (4.3)$$

where the functions f and $g_{\mu\nu}$ are defined as

$$f(\mathbf{m}^2) = \frac{e^{-\pi^2 \mathbf{m}^2 / \beta^2}}{\mathbf{m}^2} \quad (4.4)$$

$$g_{\mu\nu}(\mathbf{m}) = \left(\delta_{\mu\nu} - 2 \frac{1 + \pi^2 \mathbf{m}^2 / \beta^2}{\mathbf{m}^2} \mathbf{m}_\mu \mathbf{m}_\nu \right), \quad (4.5)$$

and the structure factor is

$$S(\mathbf{m}) = \sum_i q_i e^{2\pi i \mathbf{m} \cdot \mathbf{r}_i}. \quad (4.6)$$

In mesh-based algorithms, the reciprocal space term in the Ewald sum is calculated with the aid of the FFT [137] by replacing the point charges, located in the continuum at positions \mathbf{r}_i , with a discretized distribution on a lattice with nodes at positions \mathbf{r}_p

$$\tilde{\rho}(\mathbf{r}_p) = \frac{1}{h^3} \sum_i W(\mathbf{r}_p - \mathbf{r}_i), \quad (4.7)$$

where h is the lattice spacing and $W(\mathbf{r}_p - \mathbf{r}_i)$ is a suitable charge assignment function. The structure factor $S(\mathbf{m})$ is then replaced in equations 4.3 by its estimate $\tilde{S}(\mathbf{m}) = B(\mathbf{m})\text{FFT}[\tilde{\rho}]$, which is now evaluated on the points of the reciprocal lattice, and where the function $B(\mathbf{m})$ depends on the specific interpolation scheme [28, 138].

The choice of the assignment function for the discrete charge distribution is not unique, a fact that has led to the appearance of families of methods such as the Particle-Particle-Particle-Mesh (P3M) of Hockney and Eastwood [29], and the Particle Mesh Ewald (PME) in its original variant [27] that uses Lagrange interpolation or in its "smooth" version [28] (sPME) based on cardinal B-splines, as discussed in section 1.4.2. Once a physical quantity pertaining to single particles has been calculated on the lattice, it has to be interpolated back from the lattice to the real position of the particles. This is usually done by the same assignment function used to generate the distribution on the lattice [138]. If a function $A(\mathbf{r}_p)$ is known at the lattice nodes, it can be distributed back to the atomic positions using

$$A(\mathbf{r}_i) = \sum_{\mathbf{r}_p} A(\mathbf{r}_p) W(\mathbf{r}_i - \mathbf{r}_p). \quad (4.8)$$

The reciprocal space term of the virial in the Ewald sum can be easily written in a form that is suitable for the Harasima path formulation, which associates to particle i the contribution [130]

$$\Xi_{\mu\nu}^{\text{rec},i} = \frac{q_i}{V} \sum_{\mathbf{m} \neq 0} \text{Re} \left\{ \frac{e^{-i\mathbf{m} \cdot \mathbf{r}_i}}{2\pi V} S(\mathbf{m}) \right\} f(\mathbf{m}^2) g_{\mu\nu}(\mathbf{m}). \quad (4.9)$$

As we are interested in the diagonal elements of the tensor only, $\mu = \nu$, the real part operator in equation 4.9 is unnecessary because the f and $g_{\mu\nu}$ are even functions of \mathbf{m} . Another approach was previously used in literature to take into account the reciprocal space contribution to the local pressure for the plain Ewald method [139], but consisted of distributing the reciprocal space virial contribution equally to each particle, which is

not a justified assumption as the reciprocal space force contribution is different for each particle.

Note that, because the contribution in reciprocal space is not pairwise additive, it is not possible to use an Irving-Kirkwood formulation either for the Ewald sum, or for its mesh-based approximations [130].

We now proceed to extending the reciprocal space contribution to mesh-based algorithms, by noting that equation 4.9 is, for $\mu = \nu$, the discrete inverse Fourier transform of the complex function $S(\mathbf{m})f(\mathbf{m}^2)g_{\mu\nu}(\mathbf{m})$, evaluated at the positions of the particles and scaled by the factor q_i . On the lattice, this expression is replaced by the inverse FFT of the function $\tilde{S}(\mathbf{m})f(\mathbf{m}^2)g_{\mu\nu}(\mathbf{m})$. This quantity is eventually interpolated back to the real positions using equation 4.8, leading to the approximate expression for the reciprocal space contribution

$$\tilde{\Xi}_{\mu\mu}^{\text{rec},i} = \frac{q_i}{V} \sum_{\mathbf{r}_p} \tilde{\Xi}_{\mu\mu}^{\text{rec}}(\mathbf{r}_p) W(\mathbf{r}_i - \mathbf{r}_p), \quad (4.10)$$

with

$$\tilde{\Xi}_{\mu\mu}^{\text{rec}}(\mathbf{r}_p) = \text{FFT}^{-1} \left[B(\mathbf{m}) \text{FFT}[\tilde{\rho}] f(\mathbf{m}^2) g_{\mu\mu}(\mathbf{m}) \right]. \quad (4.11)$$

Notice that in order to be consistent with the sum equation 4.3, the argument of the inverse FFT in equation 4.11 for $m = 0$ must be set explicitly to zero. The correction and exclusion terms in real space [28] are expressed as sum of pair contributions and, thus, must be taken into account similarly to other pairwise, short range interactions.

We would like to stress once more that, thanks to the use of the Harasima formulation, it is possible to associate a virial contribution to each particle, and the local stresses are therefore distributed in the continuum. Here, a grid is used only for the mesh-Ewald charge spreading procedure and, once the back-interpolation is performed, the reciprocal space contribution is associated to the individual particles.

In order to check for the correctness and proper implementation of the algorithm, we tested it on a system of point charges (in absence of any other type of interaction but the electrostatic one). As a first step, we checked that the sum of the pressure terms associated to the atoms indeed yields the global virial up to roundoff errors. Subsequently, we computed the root mean square error ΔP per particle, following Holm and Deserno [138], as

$$\Delta P = \sqrt{\frac{1}{N} \sum_i \sum_{\mu} (P_{\mu\mu}^i - \hat{P}_{\mu\mu}^i)^2}, \quad (4.12)$$

where N is the number of charges and $\hat{P}_{\mu\mu}^i$ is a reference value, namely the pressure contribution of particle i calculated on the same configurations using the plain Ewald

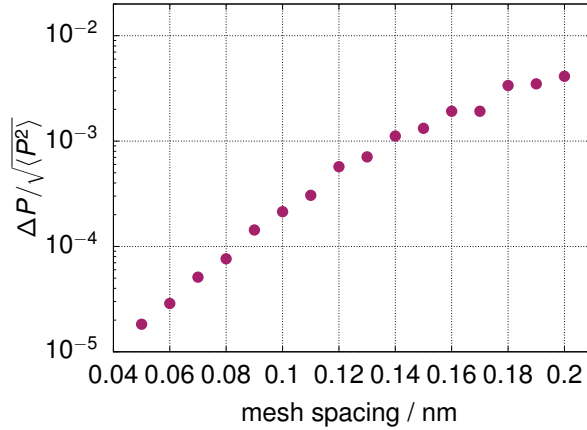


Figure 4.1. Root mean square error per particle for the pressure, as a function of the mesh spacing (charge interpolation order set to 4).

method, with a large number of reciprocal space contributions (12 along x and y direction, 36 along z direction), and a relative accuracy at the cutoff (1.5 nm) of 10^{-5} . In figure 4.1 and figure 4.2 we present, respectively, the relative root mean square error $\Delta P / \sqrt{\langle P^2 \rangle}$ per particle, as a function of the mesh spacing and of the charge interpolation order, where $\langle P^2 \rangle = \frac{1}{N} \sum_i \sum_\mu \hat{P}_{\mu\mu}^2$.

The average error that is made in estimating the pressure contribution is less than 0.5% for all choices of parameters and decreases monotonically with decreasing mesh spacing and increasing interpolation order, down to 0.001%. Similarly, we computed the root means square relative error on the pressure per particle introduced by using a simple cut-off scheme, always calculated on the same set of configurations. If the electrostatic force is truncated at 1.5 nm, the root mean square error on the pressure per particle is about 200%.

4.2 The pressure profile of water/vapor interface

We proceed with the application of the method presented above to the water/vapor interface, where water molecules were modeled by the SPC/E [95] potential. While other models compare better with several experimentally known quantities [140, 141], SPC/E represents an optimal choice for testing new methods, owing to its modest computational requirements.

The initial configuration was generated by increasing the Z box edge of a $5 \times 5 \times 5 \text{ nm}^3$ equilibrated water simulation box to 15 nm. The simulations themselves were performed on the NVT ensemble. To integrate the equations of motion we used an integration step

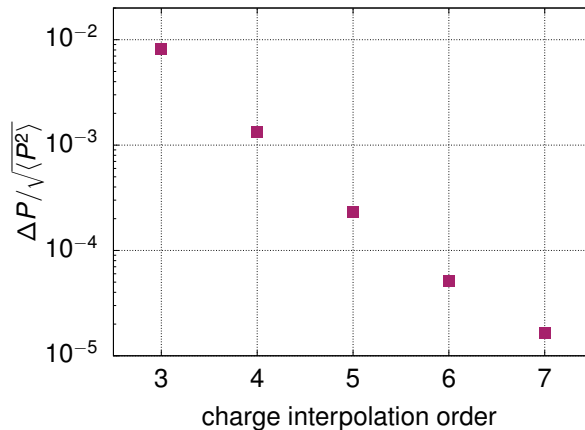


Figure 4.2. Root mean square error per particle for the pressure, as a function of the charge interpolation order (mesh spacing set to 0.15 nm).

of 1 fs, constraining all bonds by means of the SHAKE algorithm [98], and keeping the temperature at the constant value of 300 K by means of the Nosé–Hoover thermostat [32, 33]. The short-range part of the potentials were cut off either at 1.5 or at 2.0 nm and, at that distance, the relative accuracy of the direct space contribution to the electrostatic potential was set to 10^{-5} . The long-range correction to the electrostatic potential was calculated using sPME for all trajectories, with a target lattice spacing of 0.15 nm. No long-range corrections were used for the van der Waals potential. Configurations, including atomic positions and virial contributions, were saved to disk every 0.1 ps. The contributions to the lateral virial stemming from the Lennard-Jones interaction and constraint forces [133] were taken into account with the expression of the virial for the Harasima path $\Xi_{\mu\mu}^i = -1/2 \sum_{j \neq i} f_{\mu}^{ij} r_{\mu}^{ij}$, where f_{μ}^{ij} and r_{μ}^{ij} are the components of the pair forces and of the vectors connecting the two interacting atoms, respectively.

We calculated the surface tension profile with the Harasima path, including the full sPME contributions and Lennard-Jones interactions cut off at $r_c = 1.5$ nm, and compared it with the profile calculated using the procedure of Vanegas and coworkers [135] using the Irving-Kirkwood path and cut-off values of 1.5 and 2.0 nm, respectively. The resulting profiles are illustrated in figure 4.3. The two profiles calculated using the Irving-Kirkwood path are qualitatively similar, differing only in the peak height. On the other hand, the profile calculated with the Harasima path is shifted by about 0.05 nm towards the center of the fluid slab. From the surface tension profiles $\gamma(z)$ it is possible to calculate both the surface tension $\gamma = (1/2) \int \gamma(z) dz$ as well as the position of the surface of tension [42] $z_s = (1/2\gamma) \int \gamma(z) |z| dz$. The values of the surface tension γ computed from the integral of the profile and from the global pressure tensor are collected in table 4.1, together

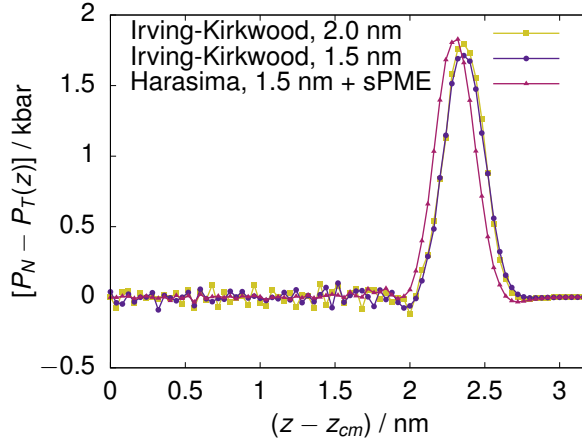


Figure 4.3. Comparison between the surface tension profile $\gamma(z)$ obtained with two different paths (Irving-Kirkwood and Harasima) and two different cut-off values for the short-range forces and (in the case of the Irving-Kirkwood path) for the calculation of the electrostatic contribution to the pressure. The profile is the average of the two halves of the simulation box, and the origin is in the middle of the water slab.

with the values of z_s and of its distance $\delta = z_e - z_s$ from the location of the equimolar surface z_e . The equimolar surface is defined as the one that divides a volume V in two regions (liquid and vapor) of volumes V_l and V_v , respectively, such that $\rho V = \rho_v V_v + \rho_l V_l$, with ρ_v and ρ_l the densities of the two phases as measured far from the interface [42]. Since we have two interfaces, we apply this criterion to half of the simulation box (the liquid phase being centered in the box) and obtain that $\rho_l z_e + \rho_v (L/2 - z_e) = \rho L/2$, or $z_e = L(\rho - \rho_v)/2(\rho_l - \rho_v)$. Since in our case $\rho_v/\rho \simeq \rho_v/\rho_l \simeq 10^{-5}$, we can safely use the approximation $z_e \simeq \rho L/(2\rho_l)$.

The equimolar surface was found to be located at $z_e = 2.43 \pm 0.01$ and 2.40 ± 0.01 nm for the 1.5 and 2.0 nm cutoff cases, respectively. For the sake of comparison, in table 4.1 some data from the literature obtained with different mesh parameters and cutoff treatment are reported, for the surface tension of the SPC/E model at 300 K.

It is interesting to note that analytical results estimate the value of δ to be in the range of the molecular size r_m (at least, for pair potentials). More precisely, $\delta \simeq r_m/3$ and $r_m/4$ for the Irving-Kirkwood and Harasima paths, respectively [42]. This means, in the case of water, $\delta \simeq 0.1$ and 0.08 nm for the two paths, respectively. These values are compatible with those presented here.

In order to show the possibilities opened by the use of the Harasima path, we performed a decomposition of the lateral pressure profile in the contributions coming from successive molecular layers, starting from the surface one. The interfacial analysis was

Table 4.1. Surface tension (bar nm) as derived from the integral of the surface tension profile (γ^\dagger) and from the global pressure tensor components (γ), position of the surface of tension z_s (nm), and offset δ (nm). The quantities have been calculated using the Irving-Kirkwood (I-K) and Harasima (H) paths, for different values of the cutoff radius r_c .

	r_c	γ^\dagger	γ	z_s	δ
I-K	1.5	565	588±3	2.40	0.03±0.05
I-K	2.0	577	611±5	2.38	0.02±0.05
H	1.5	588	588±3	2.30	0.10±0.05
Ref[142]	1.3	-	602	-	-
Ref[143]	0.98	-	567	-	-

performed on a molecular basis using a probe sphere radius of 0.2 nm. Vapor phase molecules were identified using a neighbor list cluster-search algorithm based on a simple oxygen-oxygen distance cutoff of 0.35 nm, corresponding to the first minimum of the oxygen-oxygen radial distribution function of water.

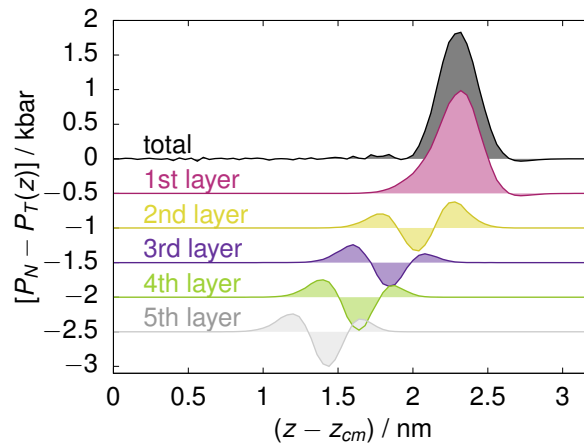


Figure 4.4. Lateral pressure profile ($P_N - P_T(z)$) of the water/vapor interface.

As discussed in chapter 2, the presence of successive layers below the surface is not just a feature encountered in solids, but is also present in liquids and can be clearly seen by calculating the intrinsic density profile 2.5. In a similar fashion, we define the *intrinsic pressure profile* as

$$\gamma_I(z) = P_N - \frac{V}{A} \left\langle \sum_i P_T^i \delta(z - z_i + \xi(x_i, y_i)) \right\rangle. \quad (4.13)$$

Having access to the virial contribution of all particles, it is straightforward to compute both the non-intrinsic and the intrinsic pressure profiles. In figure 4.4, the total value of the non-intrinsic profile of $\gamma(z)$ is presented, together with its decomposition into the successive layers contributions, up to the fifth layer. It is important to notice that while

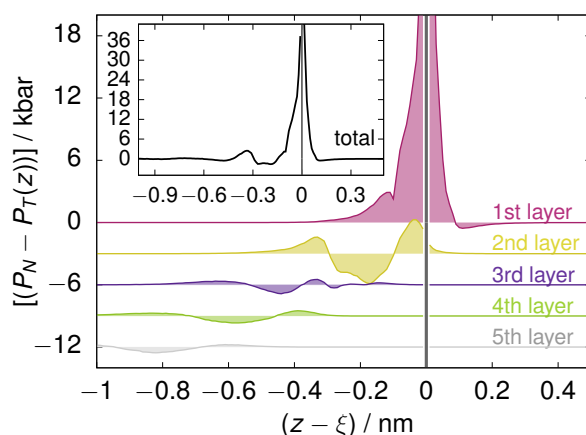


Figure 4.5. Intrinsic lateral pressure profile ($P_N - P_T(z)$) of the water/vapor interface. The total profile is shown in the inset. Delta-like contributions at the interface ($z = \xi$) are replaced by a gray band in the corresponding bin.

the total normal pressure profile must be a constant to ensure mechanical stability, this is no longer true for the separate layer contributions. As we do not have direct access to the normal component using the Harasima path, the layer decomposition has to be understood, strictly speaking, as that of the lateral pressure, which is offset by the value P_N for convenience. Nevertheless, this decomposition is still instructive, as one can find that the first layer profile contributes the most to the total profile, even though the latter is more narrowly distributed than the former. The net contribution of each of the layers far from the interface is close to zero, consistent with the fact that in this region the fluid is already homogeneous and isotropic. The distribution itself, however, is far from being identically zero, and reflects the fact that in the oscillating layer, atoms are undergoing different stresses depending on their distance from the average position of the surface.

The width of the contribution of the different layers is, on the other hand, almost constant and close to the size of the first water coordination shell (of radius 0.35 nm). Note that the distribution is normalized such that its integral, from the center of the liquid slab ($z = 0$) up to the box edge length, yields exactly the surface tension. The intrinsic profile, $\gamma_I(z)$, figure 4.5, provides a complementary point of view on the pressure profile distribution. The intrinsic profile is calculated as a function of the distance from the local surface position, $\xi(x, y)$, according to equation 4.13, removing the corrugating effect of thermal capillary waves. From a comparison between the two plots, one can appreciate the considerable narrowing of the pressure distribution, which decreases from 0.5 nm in the non-intrinsic case, to 0.3 nm in the intrinsic case, clearly showing the smearing effect of capillary waves. A striking difference between the pressure profile of a molecular liquid such as water, and that of an atomic liquid like argon [131], is that the contributions of the

layers are much less separated. Since the touching condition between the probe sphere and a surface atom takes into account the atomic radius, some (point-like) hydrogen atoms in the second layer will be located further than an oxygen atom of the first layer, contributing to the enhanced layer interpenetration. In addition, since we are considering molecular layers, the contribution to the first layer comes also from atoms that are not right at the surface and, therefore, the first layer contribution is not just a delta function, as is typical for simple liquids [77]. The second, qualitative difference with respect to simple liquids, is that the major part of the lateral tension arises from atoms located in a narrow interval of 0.3 nm around the interfacial centers, a range comparable with one molecular diameter. The first molecular layer, in particular, contributes to more than 90% of the total surface tension. In simple liquids, the distribution of the lateral pressure extends to almost two atomic diameters, and the contribution of the first layer is slightly less than 80%.

4.3 Conclusions

In this chapter, we presented a method to calculate the long-range contribution of the electrostatic interaction to the local pressure tensor, based on mesh-based algorithms. We implemented our approach in the GROMACS molecular simulation package and have tested it on a model of water/vapor interface. We calculated the lateral pressure profile with our approach, and compared it to the one computed using the Irving-Kirkwood path. In addition, we have shown how it is possible to take advantage of the Harasima path decomposition to calculate the layer-by-layer contribution to the intrinsic and non-intrinsic lateral pressure profile. The present method is highly efficient, as it displays the same $N \log(N)$ scaling as the sPME algorithm used to compute long-range correction to forces and energy.

Chapter 5

Non-zero Ideal Gas Contribution to the Surface Tension of Water

The surface tension of a fluid can be obtained in several ways from the microscopic variables describing the system: the so-called mechanical route introduced in the previous chapter links the surface tension of a planar interface to the imbalance between the normal (P_N) and lateral (P_T) components of the pressure tensor, $\gamma^p = \int_{-\infty}^{\infty} P_N - P_T(z) dz$. In a periodic system of size L one can use the volume average of the pressure tensor to write the surface tension as $\gamma^p = L(P_N - P_T)/2$, where the factor $1/2$ takes into account the presence of two interfaces. For a system of point-like particles, the pressure tensor \mathbf{P} can be accessed through the virial [144, 145], $\mathbf{P} = 2(\mathbf{K} - \mathbf{\Xi})/V$, where V is the system volume, $\mathbf{K} = 1/2 \sum_i m_i \mathbf{v}_i \otimes \mathbf{v}_i$ is the kinetic energy tensor (corresponding to the ideal gas contribution) and $\mathbf{\Xi}$ is the virial tensor, which, for pairwise-additive forces \mathbf{f}_{ij} between particle i and j can be written as $\mathbf{\Xi} = -1/2 \sum_{i>j} \mathbf{r}_{ij} \otimes \mathbf{f}_{ij}$. If no constraints are present in the system, it is possible to invoke the equipartition theorem [146], $\langle x \partial H / \partial x \rangle = k_B T$ (H being the Hamiltonian, k_B Boltzmann's constant, and T the absolute temperature) for the elements of the kinetic energy tensor, and write the (average) pressure tensor as $\mathbf{P} = \rho k_B T \mathbf{1} - 2\mathbf{\Xi}/V$, where ρ is the number density of atoms, and $\mathbf{1}$ is the unit tensor. This allows to write an alternative expression for the surface tension, $\gamma^{\Xi} = -L/(2V) (\Xi_N - \Xi_T)$, which is, on average, completely equivalent to the one involving the full pressure tensor, γ^p , but has the advantage of not requiring to sample velocities. The equivalence $\gamma^p = \gamma^{\Xi}$, in other words, means that only the virial part of the pressure contributes to the surface tension, whereas the ideal gas contribution is zero. This is only true in absence of constraints.

In water, however, the softest internal degree of freedom, the bending mode, has a frequency of about 1640 cm^{-1} . This corresponds, at room temperature, to an activation energy for the first excited state of roughly $7.8 k_B T$, and a corresponding average energy of

about $3 \times 10^{-3} k_B T$. Excited stretching modes have even higher energies, and in this sense water molecules are, for the sake of computing the surface tension, just rigid bodies. In this case, the partition function is not separable any more into a kinetic and a configurational part [147–150], and the corresponding constraints acting on Cartesian coordinates and velocities appear in the expression for the pressure tensor, as it is well known for liquid crystals [151]. Small molecular liquids, on the contrary, do not usually enjoy long-range order in the bulk, and the effect of this coupling vanishes due to isotropy. The presence of an interface, introducing a preferential direction in the system, can, however, change this picture substantially, so that in principle the equivalence between γ^p and γ^Ξ is not guaranteed any more, and a finite ideal gas contribution to the surface tension could appear.

In the course of extensive testing for the calculation of the surface tension of the SPC/E water model [95] as detailed in the previous chapter, we found that the difference between γ^p and γ^Ξ amounts to about 15% at ambient temperature. The same discrepancy persisted with different software packages, integrators, thermostats, and electrostatic treatments. In particular, we reproduced the same behavior also in the microcanonical ensemble, guaranteeing conservation of the total energy to within at least 1 ppm, with no evident drift within one nanosecond of simulation. The asymmetry of the kinetic energy tensor does not show any dependence on system size or timestep, ruling out other known effects that seemingly violate equipartition [152–156]. Although this effect does not depend on the implementation of the constraints, substituting them with harmonic springs completely removes the asymmetry, and allows to recover the equality $\gamma^p = \gamma^\Xi$, confirming that it is the rigid arrangement of atoms in the molecules that is at the origin of this apparent violation of equipartition.

Since the properties of water molecules at the liquid/vapor interface differ from the bulk ones only in the first two or three layers [157, 158], it is reasonable to expect the kinetic energy tensor to be anisotropic only in proximity to the interface. The kinetic energy tensor is a well-defined local quantity, therefore it is possible to calculate, without the ambiguity that characterizes the configurational part of the pressure [129], its profile along the surface normal, $\mathbf{K}(z) = \langle 1/2 \sum_i m_i \mathbf{v}_i \otimes \mathbf{v}_i \delta(z - z_i) \rangle$, where it is assumed that the center of mass of the liquid phase is shifted at the origin of the coordinate system. The difference between the normal and the lateral components of $\mathbf{K}(z)$ can be used to compute the ideal gas contribution $\gamma^{\text{id}}(z) = \gamma^p(z) - \gamma^\Xi(z)$ to the surface tension, shown in figure 5.1, which is indeed concentrated in proximity to the interfaces. The ideal gas contribution originates only from the rotational degrees of freedom of the molecules, as the translational ones behave isotropically.

The coupling of the kinetic degrees of freedom to the positional ones can be exploited

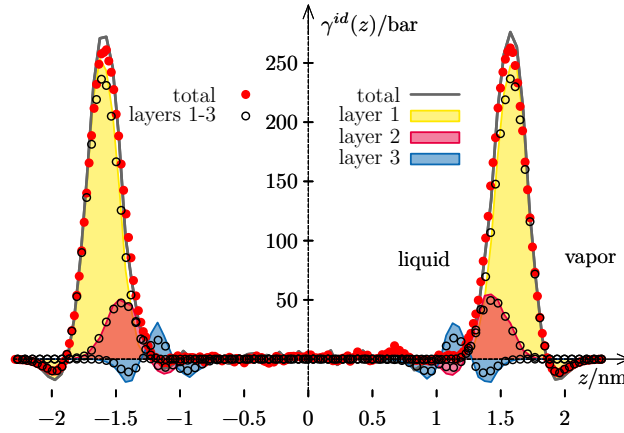


Figure 5.1. Ideal gas rotational contribution γ^{id} to the surface tension profile as computed from the kinetic energy tensor (solid line) and from Eq. (5.1) (full circles); contribution of successive molecular layers calculated from the kinetic energy tensor (shaded areas) and from Eq. (5.1) (open circles).

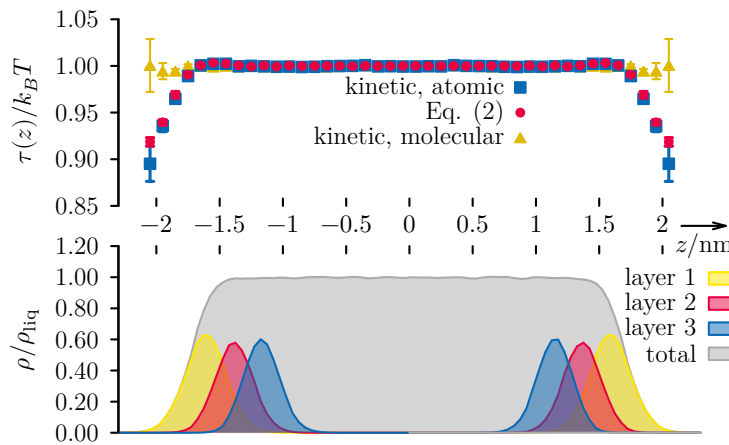


Figure 5.2. Upper panel: kinetic energy density profile $\tau(z)$ calculated using the atomic expression $k_B \tau(z) = \text{Tr} \mathbf{K}(z) / \rho(z)$ (blue squares), using Eq.5.2 (red circles), and using the molecular expression (yellow triangles), as described in the text. Lower panel: atomic density profile of the whole system and of the first three layers, normalized to the density in the liquid region.

to derive an expression for the ideal gas surface tension profile of rigid molecules, as a function of molecular orientations. Using the atomic positions \mathbf{r}'_i and the angular velocity vector ω in the molecular co-moving frame, the velocity of each atom in the lab frame can be written as $\mathbf{v}_i = \omega \times \mathbf{R}(\phi, \theta, \psi)\mathbf{r}'_i$, where \mathbf{R} is the Euler rotation matrix parametrized by the three Euler angles ϕ, θ, ψ . With the help of the equipartition theorem, quadratic terms in the components of ω appearing in the average can be expressed as functions of the components of the inertia tensor \mathbf{I} associated to the molecular structure. For a simple *symmetric top*, corresponding to the case of a linear molecule, such as O_2 , where $\mathbf{I} = \text{diag}(I, I, 0)$, the ideal gas surface tension contribution of the i -th atom is $\gamma_i^{\text{id}} = -k_{\text{B}}TL P_2(\cos \theta_i)/2V$, where $P_2(\cos \theta) = 3/2 \cos^2(\theta) - 1/2$ is the second order Legendre polynomial and θ_i identifies the angle between the molecular axis and the macroscopic surface normal Z . For a flat, *asymmetric top* like water, initially laying in the XZ plane with the dipole vector oriented along the Z axis, $\mathbf{I} = \text{diag}(I_x, I_x + I_z, I_z)$, and the ideal gas contribution of the i -th atom located, in the molecular frame, at $(x'_i, 0, z'_i)$, takes the form

$$\gamma_i^{\text{id}} = \frac{Lk_{\text{B}}Tm_i}{2VI_xI_yI_z} [f(\mathbf{I})P_2(\cos \theta) + g(\mathbf{I})P_2(\cos \delta)], \quad (5.1)$$

where $f(\mathbf{I}) = I_xI_y(x_i'^2 - z_i'^2)$, $g(\mathbf{I}) = I_xI_yx_i'^2 + I_z^2z_i'^2$, and δ , the angle between the molecular plane and the surface normal, is related to the Euler angles through the expression $\cos(\delta) = \cos(\psi) \sin(\theta)$.

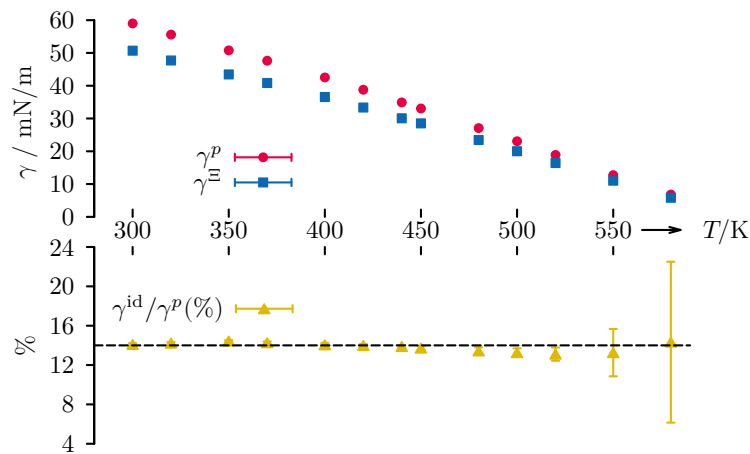


Figure 5.3. Upper panel: surface tension γ^p and virial contribution γ^E as a function of temperature. Lower panel: ratio $\gamma^{\text{id}}/\gamma^p = 1 - \gamma^E/\gamma^p$. Error bars are always smaller than the symbols in the upper panel, and are for all temperatures of the order of 0.1-0.2 mN/m.

The surface tension profile calculated using Eq. (5.1) as $\gamma(z) = \sum_i \langle \gamma_i \delta(z - z_i) \rangle$ reproduces strikingly well the ideal gas rotational contribution obtained using the kinetic energy tensor, as illustrated by figure 5.1. The integral of the two curves differ only by

Table 5.1. Temperature-independent ratio $\gamma^{\text{id}}/\gamma^{\text{p}}$ (%) for different water models.

SPC	SPC/E	TIP3P	TIP4P	TIP4P-2005	TIP5P	TIP5P/E
14.3(2)	15.0(1)	15.4(2)	11.5(1)	11.4(1)	9.2(5)	8.7(4)

0.5%.

This shows that, in fact, equipartition is not violated, as it has been used to derive Eq. (5.1), taking into account the correlations between kinetic and positional degrees of freedom, introduced by the presence of the rigid constraints. The explicit relation between the ideal gas contribution and the molecular ordering can be now used to look from a different perspective at some other results related to the surface tension. More precise structural information can be gained by identifying the molecules composing successive molecular layers below the interface [51, 131], and calculating their contribution to the ideal surface tension γ^{id} . Such an decomposition, also shown in figure 5.1, shows that the difference between the normal and lateral kinetic components of the stress tensor is indeed located mainly at the first molecular layer, with some minor deviations showing up in the second one, and with the third layer being already characterized by nearly zero-sum oscillations, which have a modest contribution to the total value of γ^{id} . We already observed this kind of oscillations in the full surface tension profile of water in figure 4.4, but their physical significance was not clear because of the virial contribution to the pressure profile not being a well-defined quantity [42]. The kinetic part of the profile, however, does not suffer from these interpretation problems, and the profile obtained by using equation 5.1 to compute the contribution of different layers (figure 5.1, open circles) shows that the oscillations are the result of the correlation between molecular orientation and deviation from the mean layer position.

Not only the surface tension, but also the kinetic energy density shows departure from the constant value one would expect. For water molecules, the relation between kinetic energy E , number of atoms N and temperature is $k_{\text{B}}T = \langle E/N \rangle$, which can be written naively in a local form as $k_{\text{B}}\tau(z) = \text{Tr}\mathbf{K}(z)/\rho(z)$, with $\tau(z)$ representing the kinetic energy density profile. The profile so defined departs from the constant value T in the proximity of the interface (see figure 5.2). This, again, is not a violation of the equipartition theorem, which can be used to derive the correct expression for the average kinetic energy contribution of the i -th atom in the water molecule

$$e_i = m_i \frac{k_{\text{B}}T}{2} \left\{ \frac{3}{M} + \frac{x_i'^2}{I_y} + \frac{x_i'^2}{I_z} + \frac{z_i'^2}{I_x} + \frac{z_i'^2}{I_y} \right\}, \quad (5.2)$$

where M is the mass of the molecule, and the term $3/M$ is the molecular center of mass velocity (translational) contribution to the kinetic energy of the atoms, while the remaining terms are the rotational contributions (interestingly, for the symmetric top, the rotational contribution of each atom is simply $k_B T/2$). The atomic kinetic energy density profile can thus be written using only atomic positions as $k_B \tau(z) = \sum_i \langle e_i \delta(z - z_i) \rangle / \rho(z)$, and is shown in figure 5.2 to reproduce very well the kinetic definition. Obviously, this quantity does not correspond to the usual thermodynamic temperature, which is expected to be constant across the interface. The temperature so defined loses its meaning once correlations between momenta and atomic positions occur. However, by using a molecular-based definition of the kinetic energy, in which the translational and rotational contributions are concentrated at the center of mass of the molecule, one obtains the expected constant profile, as shown also in figure 5.2.

As it is clear that the kinetic part of the pressure tensor is needed to compute the correct value of the surface tension if rigid molecules are present in the system, one might wonder if this can create problems for methods like Monte Carlo, which do not provide explicit access to momenta. In fact, if one wants to compute the surface tension through explicit calculation of the pressure tensor elements, there is no other way but to include the kinetic contribution through formulae like Eq. 5.1. However, this is not the only possible way to obtain the surface tension: the test-area method [159] (of which also local variants exist [160]), for example, follows a thermodynamic approach to compute the surface tension as the limit towards vanishing cross-sectional surface area perturbations ΔA (at constant volume) of the associated changes in Helmholtz free energy F , so that $\gamma = \lim_{\Delta A \rightarrow 0} \Delta F / \Delta A = -k_B T \ln \langle \exp(-\Delta U / k_B T) \rangle$, where ΔU is the change in potential energy between the perturbed and not perturbed state, and the ensemble average is performed over configurations sampled from the unperturbed state. Since this is (in the limit of small perturbations) the thermodynamic definition of the surface tension, one might expect it to yield the total surface tension, including the kinetic contributions. To test this, we computed the surface tension for water at $T = 300\text{K}$ using the test area method with area changes of 0.1, 0.05 and 0.01%, respectively, and extrapolated the results to vanishing area changes using a linear fit, resulting in a surface tension estimate of 59.5 ± 0.1 mN/m. This has to be compared with the mechanical route results of 59.9 ± 0.2 mN/m (full pressure tensor) and 51.2 ± 0.2 mN/m (virial contribution only). The test area method is therefore an appropriate way to obtain the surface tension with Monte Carlo methods when rigid molecules are present.

Finally, a surprising result obtained from the analysis of the temperature dependence of the ideal gas contribution on the surface tension must be mentioned. Since the orientational preference of water molecules at the surface has to vanish when approaching

the critical point, one can expect γ^{id} to decrease when the temperature increases. The values of γ^p and γ^{Ξ} show, in fact, a similar decreasing pattern, reaching convergence as the temperature approaches the critical value, as shown in figure 5.3. What is remarkable, however, is that the relative contribution $\gamma^{\text{id}}/\gamma^p$ is, to a good approximation, independent of the temperature, and oscillates within few fractions of a percent around 15%. We tested different rigid water models (SPC [161], TIP3P [162], TIP4P [162], TIP4P-2005 [163], TIP5P [164], TIP5P/E [165]), obtaining in all cases a temperature independent ratio of $\gamma^{\text{id}}/\gamma^p$, although the value itself is model-dependent, ranging from about 9 to 15%, as it is shown in table 5.1. There is, therefore, a direct proportionality between the orientational order of molecules, of which γ^{id} is representative, and the surface tension of the system, $\gamma^p \propto \gamma^{\text{id}}$.

Chapter 6

How Is the Surface Tension of Various Liquids Distributed along the Interface Normal?

Surface tension, the intensive counterpart of surface area, is a key quantity in colloid and interface science. At the molecular level, it originates from the fact that particles at the surface do not have as many and/or as strong attractive interactions with their neighbors in the opposite phase as with those within their own phase. In the particular case of the liquid-vapor interface, far from the critical point, particles that are at the surface practically lack any kind of interactions with the neighboring vapor phase. This loss of attractive interactions from the direction of the opposite phase affects not only the particles that are located right at the surface: particles in the second, third and subsequent molecular layers also miss some interactions from their outer coordination shells. In chapter 4, it was shown how surface tension is distributed in molecular layers close to the interface. Having this in mind, the following question can be raised immediately: how do the subsequent subsurface layers contribute to the surface tension of *various liquids*? Considering that surface tension originates from the lack of attractive interactions, the answer to this question can be expected to depend sensibly on the particular intermolecular interactions that characterize the given liquid phase.

Although the question concerning the distribution of the surface tension is related to the fundamental physical concept laying behind the phenomenon of surface tension, addressing it in a quantitative way was severely hindered by various difficulties. However, having developed the necessary tools as discussed in the last two chapters, computer simulations now can provide a molecular level insight into the structure and interactions of a suitably chosen model of the system of interest.

In this chapter, we present the calculation of the surface tension profile of the five different molecular liquids presented in chapter 3. The profiles of carbon tetrachloride, acetone, acetonitrile, methanol, and water, are calculated along the normal axis of their liquid-vapor interface on the basis of molecular dynamics simulations.

The surface tension profile is determined both relative to the capillary wave-corrugated, intrinsic liquid surface, and relative to the center-of-mass of the liquid phase*. In addition to the entire profiles, the contributions given by the first five molecular layers to them are also calculated in every case. Furthermore, the surface tension contribution is determined also in a layer-wise manner. The obtained distribution of the surface tension contributions along the surface normal axis is discussed in connection with the intermolecular interactions acting in the different liquid systems.

6.1 Computational Details

6.1.1 Molecular Dynamics Simulations

The simulations have been performed on the canonical (N,V,T) ensemble, similarly to those in chapter 3, but using the modified version of the GROMACS 5.1 molecular dynamics simulation package [99] that calculates also the pressure contribution of each particle. The interfacial systems were equilibrated for at least 5 ns. Finally, 20 ns long equilibrium trajectories have been generated for calculating the surface tension profiles.

6.1.2 Detection of the Intrinsic Liquid Surface by the ITIM Method

The intrinsic surfaces of the simulated liquid phases have been determined using the ITIM method [51]. For each configuration, after determining the liquid phase, we proceeded to compute the set of interfacial atoms using the ITIM algorithm [51] as described in chapter 3, using a probe sphere with a radius R_p of 2 Å. Contact position of the probe sphere with a given atom has been defined as their center to center distance being equal to the sum of the respective radii; the diameter of the atoms has been estimated by their Lennard-Jones distance parameter, σ . It should be emphasized that the surface layer has been defined on a molecular basis: once the probe sphere touches an atom the entire molecule to which this atom belongs is considered as part of the layer. Test lines have been arranged on a square grid, neighboring lines being separated by 0.5 Å from each other. The entire procedure of detecting the topmost layer of the liquid phase has been repeated five times by disregarding the molecules that belong to one of the previously identified layers. In this way, the molecules forming the first five subsequent layers of the

*This is equivalent to the laboratory-fixed frame

liquid phase have been identified separately. Finally, all results have been averaged over the two liquid-vapor interfaces present in the basic box.

6.1.3 Calculation of the Tangential Pressure Profiles

The details of the calculation of the surface tension profiles are presented in detail in chapters 4 and 5. The major points are presented again as a brief reminder.

The global pressure tensor can be expressed as a sum of a kinetic (ideal gas) and a virial (excess) term

$$\mathbf{P} = 2(\mathbf{K} - \mathbf{\Xi})/V, \quad (6.1)$$

where the kinetic is given by $\mathbf{K} = 1/2 \sum_i m_i \mathbf{v}_i \otimes \mathbf{v}_i$ and the virial term is represented by $\mathbf{\Xi} = -1/2 \sum_{i>j} \mathbf{r}_{ij} \otimes \mathbf{f}_{ij}$. Once the particle contributions have been determined, the tangential pressure profile can readily be calculated both in its nonintrinsic and in its intrinsic variants:

$$P_T(x) = \frac{V}{A} \left\langle \sum_i P_T^i \delta(x - x_i + x_{\text{com}}) \right\rangle \quad (6.2)$$

and

$$P_T(x_{\text{intr}}) = \frac{V}{A} \left\langle \sum_i P_T^i \delta(x_{\text{intr}} - x_i + \xi) \right\rangle, \quad (6.3)$$

where x_{com} is the position of the center of mass of the liquid phase along the surface normal, while ξ is the instantaneous local position of the interface.

6.2 Results and Discussion

The surface tension values obtained by integrating the non-intrinsic $P_T(x)$ curves, as described in the previous subsection, turned out to be 14.6, 15.9, 20.8, 17.3, and 58.5 mN/m, with the error bars never exceeding 0.2 mN/m, for CCl_4 , acetone, acetonitrile, methanol, and water, respectively. As a consistency check, we have repeated this calculation using the intrinsic pressure profiles, $P_T(x_{\text{intr}})$, and calculated γ also in the conventional way, using the average value of P_T as obtained from the global pressure tensor, without distributing it among the particles. The surface tension values obtained in these three different ways indeed turned out to be identical in every case up to the numerical precision of the calculations.

The non-intrinsic profiles of the tangential pressure, $P_T(x)$, are shown in figure 6.1 along with the contributions given by the first five molecular layers beneath the liquid surface, as obtained for the five liquids considered. In these profiles, the $x = 0$ Å value corresponds to the center of mass position of the liquid slab, and the vapor phase is located at x values larger than what corresponds to the position of the interface. The variation of

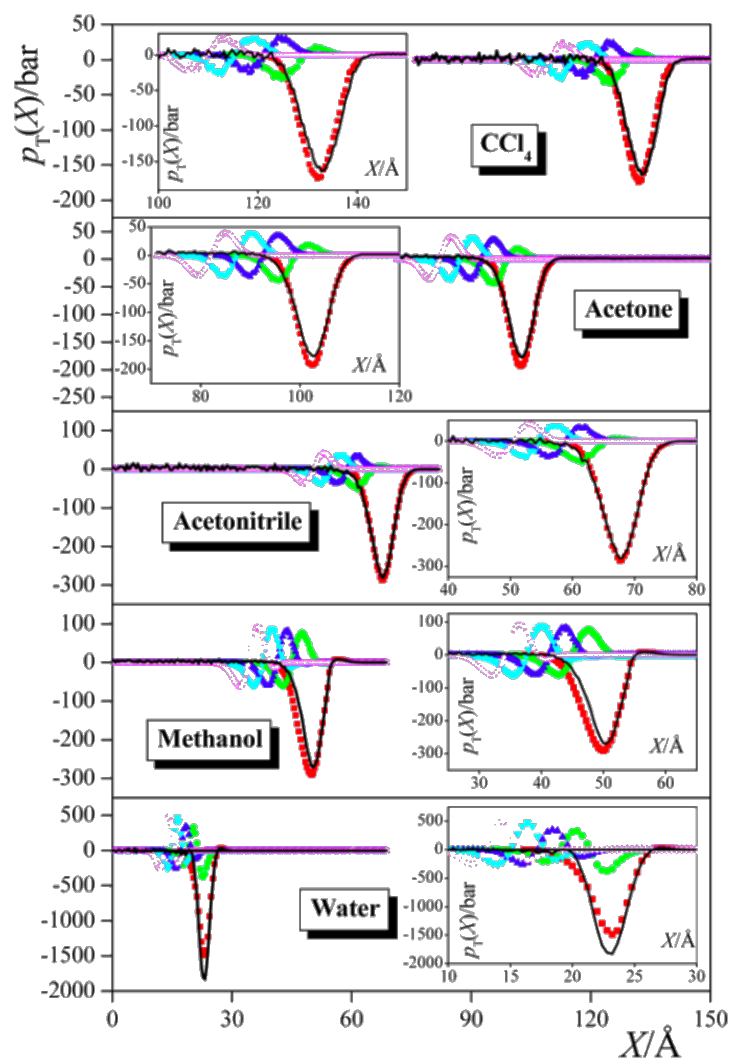


Figure 6.1. Nonintrinsic profile of the tangential pressure (black solid lines) at the liquid-vapor interface of the simulated liquids. The contributions given by the first (red), second (green), third (blue), fourth (light blue) and fifth (magenta) molecular layers beneath the surface. The insets show the structured part of the profiles on an enlarged scale.

the position of the interface along the x axis from system to system simply reflects the different densities of the different liquids. The interfacial part of the $P_T(x)$ profiles and its layer-wise contributions are shown on magnified scales in the insets of figure 6.1.

As is seen, the tangential pressure profile shows a deep minimum at the liquid side of the interface, whereas the rest of the profile is practically featureless in every case. This negative peak of the $P_T(x)$ profiles covers an about 10-20 Å wide x range, being the narrowest for water (~7 Å) and broadest for CCl_4 (~19 Å). This finding indicates that the surface tension is indeed located in a narrow, 1-2 nm wide region of the liquid at the surface. This width is larger by roughly a factor of three than the molecular size. However, due to the presence of capillary fluctuations, from the total profile it is not possible to draw any conclusion in how many molecular layers the surface tension is concentrated. Still, differences in the width of this region reflect essentially the different size of the molecules constituting the liquid phases. However, the range of this region in water is particularly narrow, and this cannot be accounted for simply by the small size of the water molecules. Rather, this narrowness is also due to the unusually strong (H-bonding) intermolecular interaction in water, which leads to rather close packing of the molecules and high density of the liquid.

The minimum of this negative peak of $P_T(x)$ corresponds to rather large negative tangential pressure values, being around 200-300 bar in every case, with the exception of water, where this value is close to 2000 bar. Since the value of the surface tension, γ , is related to the integral of this peak, it is not surprising that in liquids of similar surface tension values the depth of this minimum is also similar. However, the surface tension of the water model used here is only 3-4 times larger than that of the models of the other liquids considered, while the minimum of the $P_T(x)$ profile is an order of magnitude deeper. This is the consequence of the aforementioned exceptional narrowness of the negative $P_T(x)$ peak in water: narrow peaks must be larger in magnitude to result in the same integral value.

By looking at the decomposition of the pressure profiles into the contributions coming from different layers, also shown in figure 6.1, it is seen that that the large negative peak of the $P_T(x)$ profile is largely accounted for by the contribution of the first single molecular layer beneath the liquid surface in every case. In other words, the vast majority of the surface tension is distributed within the x range in which the first molecular layer is located. However, the profiles of the contributions of the subsequent molecular layers are not simply zero along the entire interface normal axis, instead, they typically exhibit a negative loop followed by a positive loop upon going towards the interface. In a few cases, the negative loop is seen to be larger in magnitude than the subsequent one, indicating the non-negligible contribution of also these layers to the surface tension. On the other hand,

for the majority of the cases the two loops are roughly equal in magnitude, suggesting that these layers do not give considerable contributions to the value of the surface tension. It is also seen that the position of the negative loop of a given layer typically coincides with that of the positive loop of the next molecular layer. As a consequence, the contributions of such two loops corresponding to two subsequent molecular layers largely cancel out each other, making the full $P_T(x)$ profile featureless beneath the x range of the first molecular layer.

The contributions of the second to fifth layers to $P_T(x)$ behave somewhat differently in water in this respect. Thus, here a small negative loop is typically followed by a larger positive, and then again by a small negative loop as going from the bulk liquid phase towards the interface. This "Mexican hat" shaped contribution is probably at least partly due to the fact that the 2 Å radius of the probe sphere used in the ITIM procedure is somewhat too large for probing the relatively small water molecules [62, 100]. To confirm this, we have repeated the entire analysis for water using a probe sphere of the radius of 1.2 Å. In this case, the $P_T(x)$ contributions of the second to fifth layers changed considerably toward the usual shape, leaving all other findings of us practically unchanged. It is also interesting to note that decreasing the probe sphere radius leaves the contribution of the first layer practically unchanged, but broadens and shifts towards the bulk that of the subsequent layers.

6.2.1 Intrinsic Tangential Pressure Profiles

The intrinsic profiles of the tangential pressure, $P_T(x_{\text{intr}})$, are shown in figure 6.2 along with the contributions given by the first five molecular layers beneath the liquid surface, as obtained in the five systems considered. Here, the $x_{\text{intr}} = 0$ Å value corresponds exactly to the position of the intrinsic liquid surface, whereas negative and positive x_{intr} values correspond to the liquid and vapor phases, respectively.

As it is seen, the intrinsic tangential pressure profiles show considerably more structure than the non-intrinsic ones, although the distance range covering this structured part is typically slightly narrower than that in the case of the non-intrinsic profiles. Also, the profiles of acetonitrile and methanol are somewhat more structured than those of the other systems considered. However, these fine structures are entirely described by contribution of the first molecular layer, and the distances of the peaks in this region are compatible with intramolecular distances, suggesting that this fine structure reflects intramolecular contributions rather than intermolecular ones to the pressure profile. The most apparent feature of the $P_T(x_{\text{intr}})$ profiles is the Dirac delta-like contribution at $x_{\text{intr}} = 0$ Å. Since the intrinsic liquid surface is defined through a set of interfacial atoms, all such atoms are located at exactly $x_{\text{intr}} = 0$ Å. This leads to the appearance of a peak here that is infinitely

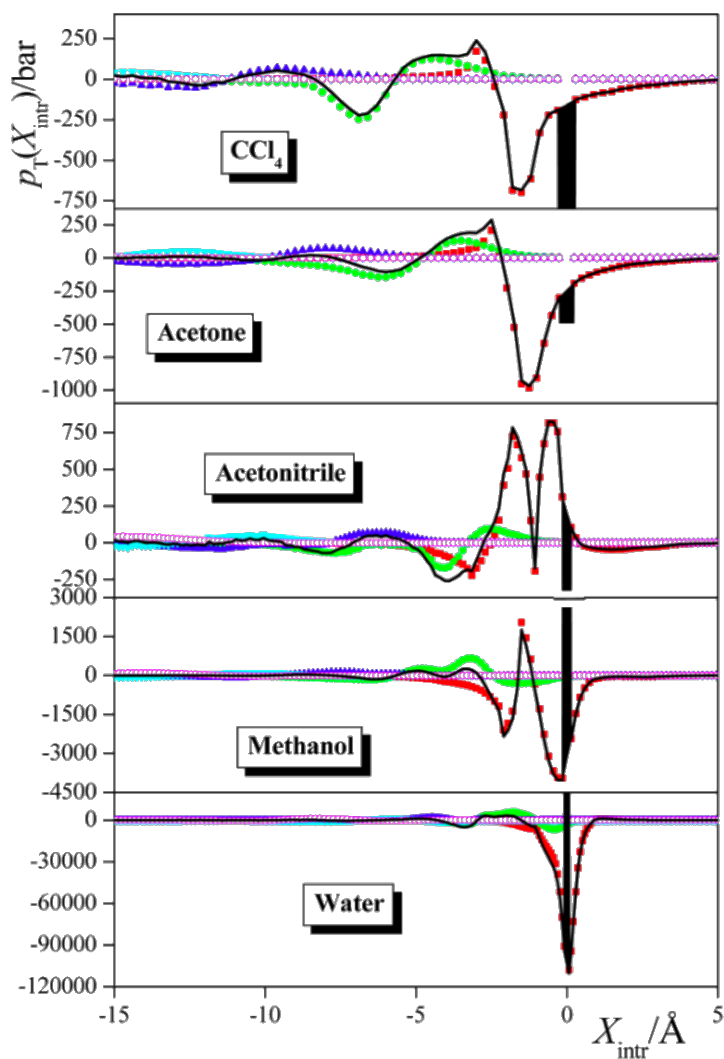


Figure 6.2. Intrinsic profile of the tangential pressure (black solid lines) at the liquid-vapor interface of the simulated liquids. The contributions given by the first (red), second (green), third (blue), fourth (light blue) and fifth (magenta) molecular layers beneath the surface.

sharp, yet corresponds to a finite integral. Although the infinite sharpness of this peak is clearly an artifact due to the definition of the intrinsic liquid surface, real physical meaning can be attributed to its *finite* integral. Besides the Dirac delta-like peak at $x_{\text{intr}} = 0 \text{ \AA}$, the $P_{\text{T}}(x_{\text{intr}})$ profiles show several oscillations at the liquid side of the intrinsic surface before they decay to a constant value.

It is also apparent from figure 6.2 that the amplitude of the peaks of $P_{\text{T}}(x_{\text{intr}})$ at the vicinity of $x_{\text{intr}} = 0 \text{ \AA}$ is typically much larger than that of the main negative peak of the corresponding non-intrinsic profile. Thus, in the case of the non-H-bonding liquids there is a factor of 3-5 between the amplitudes in the two types of profiles, while for methanol the $P_{\text{T}}(x_{\text{intr}})$ peak is about an order of magnitude and for water almost two orders of magnitude larger than that of $P_{\text{T}}(x_{\text{intr}})$.

The majority of the features of the intrinsic tangential pressure profiles are again given by the molecules constituting the first layer beneath the liquid surface. The fact that the first layer molecules contribute to $P_{\text{T}}(x_{\text{intr}})$ other than just at $x_{\text{intr}} = 0 \text{ \AA}$ is due to the fact that the layers have been defined in terms of molecules, whereas the tangential pressure is distributed among the atoms in the system. In other words, atoms of the surface molecules that are located right at the surface themselves give rise to the Dirac delta-like peak, while the other atoms belonging to the surface molecules give rise to the contributions at non-zero x_{intr} values. It should also be noted that the features of the $P_{\text{T}}(x_{\text{intr}})$ profiles that correspond to the first molecular layer are of little interest for our purpose, as they simply describe how the pressure is distributed within the molecules.

While the contribution of the first molecular layer already largely describes the entire $P_{\text{T}}(x_{\text{intr}})$ profile in every case, the contribution of the second layer is still noticeable in every case. Thus, in CCl_4 and acetone the second layer contribution fully accounts for the negative peak at about $x_{\text{intr}} = 7 \text{ \AA}$ and the positive peak around $x_{\text{intr}} = 3 \text{ \AA}$, in acetonitrile it describes the waves of $P_{\text{T}}(x_{\text{intr}})$ between 10 and 5 \AA , and contributes to the negative peak around 4 \AA , in methanol it gives rise to the small positive peaks at about 5 and 3 \AA , and in water it describes the features of $P_{\text{T}}(x_{\text{intr}})$ between about 4 and 2 \AA . On the other hand, the contributions of the third to fifth layers to the intrinsic tangential pressure profiles, in a clear contrast to those to the non-intrinsic profiles, are indeed featureless, flat curves.

Finally, it should be noted that the intrinsic tangential pressure profiles show several details that are not seen in the non-intrinsic profiles. Thus, the intrinsic profiles exhibit considerably more features in a considerably narrower distance range than the non-intrinsic ones. Thus, in contrast with the rather complex structure of the intrinsic profiles, the non-intrinsic ones exhibit one single negative peak, the amplitude of which is also much smaller than those of the corresponding intrinsic profiles. All these changes reflect

how the real, molecular level structure of the liquid surface is washed out by neglecting the effect of the capillary waves in a non-intrinsic analysis.

6.2.2 Contributions of the Individual Molecular Layers to the Surface Tension

The net contribution of the subsequent molecular layers beneath the liquid surface to the value of the tangential pressure can be calculated simply by integrating their individual contributions to the tangential pressure profile. Here it is important to notice that it is not possible to decompose the normal pressure component into layer contributions, and therefore, strictly speaking, also the layer contribution to the full surface tension is not accessible, but only its tangential contribution. However, since the normal pressure must be constant along the interface normal axis, it is sensible to assume that each layer contributes roughly equally to it, and through it also to the total value of the surface tension. Further, inside the bulk phases the tangential and normal pressure components must be equal to each other and constant along the interface normal axis. It is also clear from figures 6.1 and 6.2 that this constant value is several orders of magnitude smaller than the amplitude of the peaks of the tangential profile. Therefore, apart from the first few molecular layers, the *difference* of the normal and tangential pressure components must be zero, whereas in the first few layers the (unknown) normal pressure component must be much smaller than the tangential one, and hence can be neglected. In this sense, the tangential pressure contributions of the individual molecular layers can be interpreted as being practically equal to their full surface tension contributions. Thus, the term of the "surface tension contribution", when speaking about *individual molecular layers*, is used and has to be interpreted in the above sense throughout the text.

The obtained contributions of the first four molecular layers to the surface tension are shown in figure 6.3. The contribution of the fifth layer turned out to be negligible in every case. As a check of consistency, we have done this calculation by integrating both the intrinsic and non-intrinsic pressure profile contributions; the obtained results agreed within 0.1% in every case. As is seen, the distribution of the surface tension among the molecular layers is rather similar in the different liquids considered, in spite of the fact that they correspond to markedly different intermolecular interactions. Thus, the vast majority, namely at least 85%, of the surface tension is concentrated in the first molecular layer. The second layer still gives a noticeable, roughly 10% contribution to the surface tension, while this contribution is already negligible beyond the second layer in every case. The only exception in this respect is methanol, in which practically the entire surface tension comes from the first molecular layer.

It is also apparent from figure 6.3 that several layers give a negative contribution to the surface tension value. To understand the origin of this finding one has to consider that

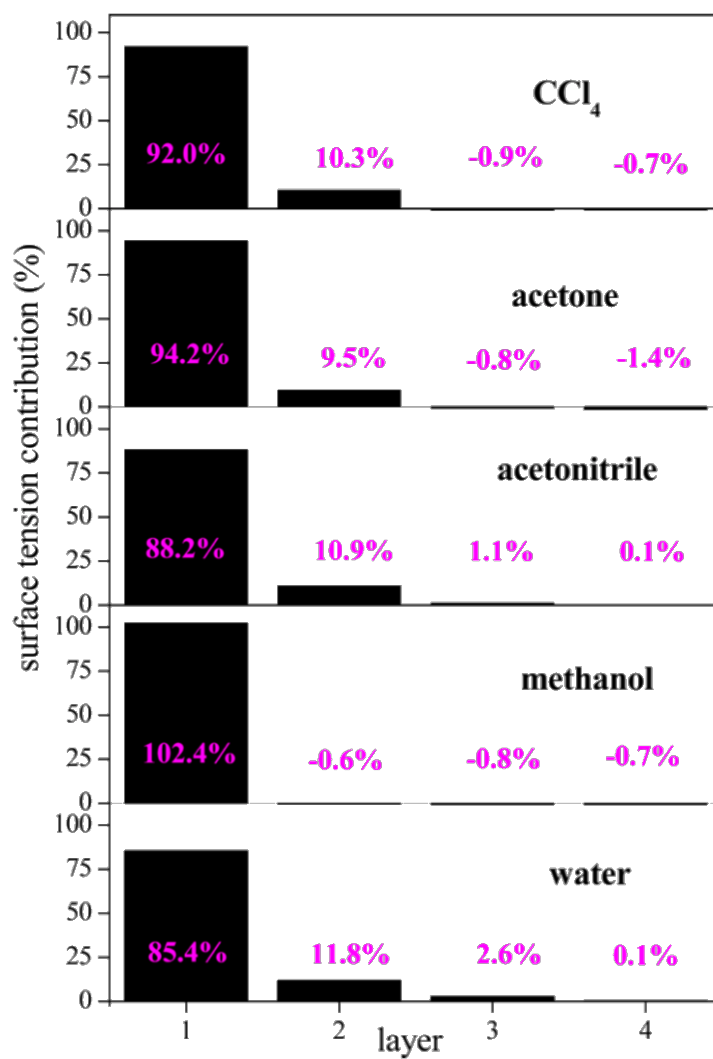


Figure 6.3. Net contribution of the first four molecular layers beneath the liquid surface to the value of the surface tension.

although the origin of the surface tension is the loss of attractive interaction of molecules being at the boundary of their phase, the surface tension itself describes the free energy cost of molecules being at the surface. More specifically, in order to decrease their energy loss surface molecules can increase their orientational order, both relative to the surface and to each other, which eventually leads the decrease of their entropy. However, while this orientational ordering might mostly or exclusively affect the surface layer itself, the corresponding energy gain can also affect the neighboring layers, which can lead to a net free energy decrease – negative surface tension contribution – in certain layers. This free energy decrease is, however, not supposed to be large, in accordance with our finding that such negative contribution to γ never exceeds 1.5%.

Although the general trends in the distribution of the surface tension clearly turn out to be system independent, details of the whole picture still depend on the particular intermolecular interactions acting in the different liquids. Thus, the roughly 10% contribution of the second layer reflects the lack of attractive interaction of these molecules with several second shell neighbors. In methanol, however, this contribution is completely missing. As it is known, in methanol the surface molecules adopt a rather strong orientational order, preferring the alignment in which the CH_3 group sticks straight out to the vapor phase. This orientation allows the surface methanol molecules to maintain all of their possible hydrogen bonds, and therefore to fully preserve their hydrogen bonding structure [109, 166], which leads to a much lower surface tension value than what could be expected considering the strength of the intermolecular interactions. Since in methanol H-bonding is the dominant interaction, but the vicinity of the interface leaves the H-bonding structure of the molecules unchanged, molecules in the second layer lack only a negligible fraction of their attractive interaction with respect to the bulk phase ones. On the other hand, in water the surface molecules adopt orientations such that they can form as many hydrogen bonds with each other as possible [51, 109]. As a price for that, hydrogen bonding between the first and second layers is, on average, weaker than in the bulk liquid phase.

Finally, it should also be noted that the obtained contributions of the individual molecular layers to the surface tension depend slightly also on the probe sphere radius used in the analysis, although the global picture is insensitive to that. Thus, when using a probe sphere of the radius of 1.2 Å instead of 2 Å for water, the contribution of the first and second layer turns out to be 96.3% and 3.8%, respectively, while that of the subsequent layers is practically zero. Similarly, when using the R_p value of 1.65 Å instead of 2 Å for methanol, the contribution of the first three layers turns out to be 106.1%, -3.5% and -1.3%, respectively. The fact that the decrease of the probe sphere radius leads to an increased contribution of the first layer is consistent with the previous finding that it shifts the peaks of the subsequent molecular layers contributions towards the bulk liquid phase, and can

be explained by the fact that smaller probe spheres can fall deeper between the molecules, touching molecules located farther from the liquid surface [51].

6.3 Conclusions

In this chapter we have demonstrated how intrinsic surface analysis methods combined with pressure profile calculations can provide a deep insight into the thermodynamics of fluid surfaces, by determining the tangential pressure profile across the liquid-vapor interface of five molecular liquids, characterized by markedly different intermolecular interactions. Since the value of the surface tension can be obtained by integrating the tangential pressure profile, this profile provides direct information on how the surface tension is distributed along the interface normal axis.

The obtained results show a surprising insensitivity of this distribution of the surface tension to the type of intermolecular interactions acting in the liquid phase. Thus, in every case, at least 85% of the surface tension comes from the first molecular layer, while, with the exception of methanol, the second layer contributes roughly 10% to the surface tension, and the contributions of the subsequent molecular layers are negligible. In methanol, on the other hand, the entire surface tension comes practically from the molecules constituting the first layer. Correspondingly, when considering a non-intrinsic coordinate frame, the surface tension is distributed in a 1-2 nm broad interval along the surface normal, which covers the distance range in which the first molecular layer is located. Using an intrinsic frame of reference, the distance range covering non-negligible surface tension contributions is even slightly narrower, and the amplitudes of the peaks of the profile are considerably larger than in the non-intrinsic case. The intrinsic analysis of the contribution of the subsequent molecular layers to the profile also reveals that practically no surface tension contribution comes from the third and subsequent molecular layers. By contrast, in a non-intrinsic treatment this information is obscured by the effect of neglecting the capillary waves in the analysis.

Although the distribution of the surface tension along the surface normal axis turned out to be largely independent from the interactions acting between the molecules in the specific systems, several details of it still reflect the peculiarities of these intermolecular interactions. Thus, in the case of water, characterized by small molecular size, particularly strong interactions and, consequently, particularly close contact of the molecules, the featured part of the surface tension profile is unusually narrow and the amplitudes of its peaks are considerably larger than what could be expected simply from the value of the surface tension. Also, due to the relatively weak interaction between the first two molecular layers beneath the liquid surface, the contribution of the second layer to the

surface tension is somewhat larger in water than in the other liquids. By contrast, the strong surface orientation of the molecules at the surface of methanol not only efficiently reduces the surface tension, but also eliminates practically the contribution of the second layer.

Chapter 7

Relation Between the Liquid Spinodal Pressure and the Lateral Pressure Profile at the Liquid-Vapor Interface

The spinodal line represents the limit of mechanical stability of a phase on the temperature (T) - pressure (P) phase diagram [167]. The liquid-vapor coexistence curve marks the limit of thermodynamic stability of the liquid phase, beyond which the liquid state no longer corresponds to the global minimum of the free energy. However, the liquid state can still exist beyond the liquid-vapor coexistence curve in the form of superheated liquid, a state that is metastable with respect to the vapor phase. This metastable region extends from the liquid-vapor coexistence curve to the liquid spinodal line, which starts from the critical point and goes below the coexistence line in the T-p phase diagram. Beyond the spinodal line, the liquid phase cannot exist even as a metastable state, as it no longer corresponds to even a *local minimum* of the free energy [167].

Approximating the location of the liquid spinodal line as accurately as possible is of great relevance both from the point of view of pure science and from that of the applications. Thus, for instance, the shape of this spinodal line – for example, whether it is re-entrant [168, 169] or not [170–175]) – can be related to the origin of a number of anomalous features of supercooled water. On the other hand, knowing the exact location of the spinodal is also of great importance in any process that involves metastable states. For example, when the pressure drop or temperature increase is very fast, near-spinodal states can be reached before nucleation takes place. This can happen during the breaking of high pressure-high temperature pipelines (such as the cooling circle of a power plant, or the storage tank of a compressed gas), resulting in a sudden and violent phase transition,

the so-called explosive or flash boiling [176–178] Similar near-spinodal states can be reached when the liquid comes into contact with hot material, such as magma or molten metal.

Finally, even near-spinodal states with negative pressure can be reached when high-amplitude pressure waves (for example, medical ultrasound) are applied in a liquid-containing environment, causing very rapid and violent cavitation or "embolism", posing a risk for neighboring materials, such as human tissues [179]. However, the spinodal line is experimentally almost inaccessible in common fluids, because upon approaching the spinodal, the liquid state becomes increasingly metastable with respect to the vapor phase, and hence the unavoidable presence of even an otherwise negligible amount of impurity leads to sudden evaporation, bringing the system to the thermodynamically stable vapor phase before the spinodal can be reached.

The liquid spinodal of a model system can, on the other hand, be accessed by computer simulation methods. Thus, as it was suggested by Poole et al. more than two decades ago, at a given temperature the pressure goes through a minimum as a function of the density (ρ). The spinodal pressure is simply the value of this minimum [170, 171]. This method has been applied to determine the liquid spinodal of various water models [170, 171, 173–175] as well as that of the Lennard-Jones system [180] and liquid SiO₂ [181]. However, similarly to the vast majority of the equations of state, potential models are also typically parametrized by fitting data corresponding to the thermodynamically stable liquid state, and hence their performance at deeply superheated and/or negative pressure states is not fully justified. Therefore, it is desirable to relate the spinodal pressure to experimentally accessible quantities, making thus the spinodal line of real liquids also accessible.

As mentioned at the beginning of chapter 4, Imre et al. conjectured that the pressure of the liquid spinodal at a given temperature is closely related to the minimum value of the lateral pressure profile, $P(x)$, across the liquid-vapor interface of the same system at the same temperature [125]. This estimation of the spinodal line, called the "interfacial spinodal", of liquid helium, the only simple liquid for which the spinodal can be experimentally accessed with reasonable accuracy, did not provide incompatible results with experimental data [182]. They also determined the interfacial spinodal of the Lennard-Jones fluid [125] and of CO₂ [183], and found them to be closely related to the spinodal line obtained from certain equations of state. Further, they also determined the interfacial spinodal of water, and used this result to distinguish between the performances of various equations of state [178].

The idea that the knowledge of the equation of state in the unstable region, between the liquid and vapor densities, can give access to the density profile, $\rho(x)$, of a liquid-

vapor interface dates back to Rayleigh [184]. In particular, if the two profiles $P(x)$ and $\rho(x)$ are known, and the latter is invertible, one can, through the function $X(\rho)$, obtain the equation-of-state $P(\rho)$. According to the conjecture of Imre et al., the pressure along the spinodal line is then related to the most negative value the pressure profile can take [125]. In the light of these considerations it is interesting to test this hypothesis, and to check if the spinodal pressure and the minimum value of the lateral pressure profile can indeed be related to each other. For this purpose, we compare these quantities for the Lennard-Jones fluid and for the SPC/E model [95] of water. For the Lennard-Jones fluid, we calculate the spinodal pressure in the conventional way, while for water we take it from the literature, [173] and compare them with those of the interfacial spinodal determined here.

7.1 Computational Details

7.1.1 Molecular Dynamics Simulations

To determine the liquid spinodal of the Lennard-Jones fluid we have performed a set of molecular dynamics (MD) simulations on the canonical (N,V,T) ensemble with 2048 Lennard-Jones particles placed in a cubic basic box at 6 different temperatures, performing simulations at 8-10 different densities at each temperature. For convenience, we use here reduced units of the temperature, number density, and pressure: $T^* = k_B T / \varepsilon$, $\rho^* = \rho \sigma^3$, and $P^* = P \sigma^{-3} / \varepsilon$, where k_B is the Boltzmann constant, and σ and ε are the Lennard-Jones distance and energy parameters, respectively. The temperatures considered are ranging from 0.7 to 0.95 in reduced units, with a spacing of 0.05. The temperature range has been chosen to be between the triple point temperature and critical temperature of the Lennard-Jones fluid, which are 0.694 [185] and 1.326 [186], respectively. However, at temperatures above 0.95 we observed bubble formation in the liquid phase of the interfacial system; hence these temperatures have been discarded. At each temperature, we started with a simulation at $\rho^* = 0.78$, and progressively decreased the density below the value at which we found a minimum of the pressure. Simulations performed below the lowest density presented in figure 7.1 have led to the immediate disappearance of the metastable homogeneous liquid phase, with a consequent bubble formation. The values of the Lennard-Jones interaction parameters have been set to $\sigma = 3.4 \text{ \AA}$ and $(\varepsilon/k_B) = 120 \text{ K}$, respectively, while the mass of the particles has been 40 a.m.u, corresponding to the argon model of Rahman [187].

To compute the interfacial spinodal, we have performed MD simulations of the liquid-vapor interface of the Lennard-Jones system and of water on the canonical (N,V,T) ensemble at the temperature values at which the spinodal was determined. It should be noted

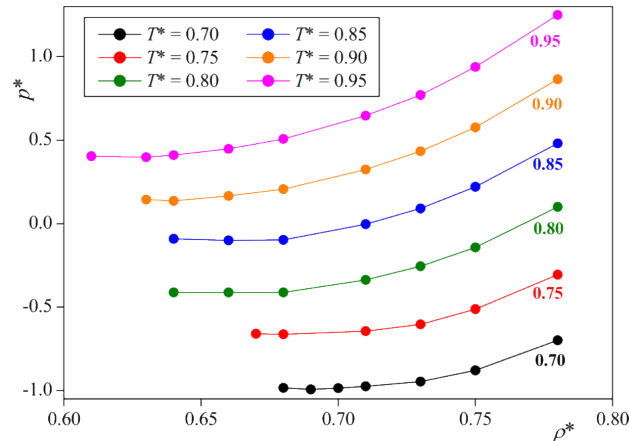


Figure 7.1. Dependence of the pressure of the Lennard-Jones fluid on the density at the six temperatures considered. The profiles corresponding to the reduced temperature values of 0.75, 0.8, 0.85, 0.9, and 0.95 are shifted by 0.15, 0.3, 0.45, 0.6, and 0.75 unit for clarity.

that for water this temperature range is particularly relevant in relation to the explanation of the anomalous features of supercooled water [168–175]. In describing water molecules, the SPC/E model [95] has been used, since the spinodal of this model has already been determined in the literature [173]. The triple point and critical point of this water model correspond to the temperature values of about 215 K [188] and 652 K [189], respectively. The rectangular basic box in the interfacial simulations has contained 2237 Lennard-Jones particles or 4000 water molecules, having the X , Y , and Z edge lengths of 180, 40, and 40 Å long, respectively, for the Lennard-Jones system, and of 300, 50, and 50 Å, respectively, for water, X being the interface normal. All simulations have been done with the modified version of the GROMACS 5.1 program package [99] that calculates also the pressure contribution of each particle. All interactions have been truncated to zero beyond the cut-off distance of 11 Å; their long range part has been accounted for using the smooth Particle Mesh Ewald method [28] for the Coulomb interaction in water as well as for the van der Waals dispersion in the Lennard-Jones system, with the accuracy of the reciprocal space contribution of 10^{-5} and 5×10^{-4} , respectively. It should be noted that taking the long-range part of the van der Waals interaction into account using an Ewald-based method is particularly important in the presence of an interface, as in this case the anisotropy of the system prevents the use of the analytical tail correction [190]. The temperature of the systems has been controlled by means of the Nosé-Hoover thermostat [32, 33]. The geometry of the water molecules has been kept fixed using the SHAKE algorithm [98]. Equations of motion have been integrated in time steps of 1 fs. Bulk Lennard-Jones and interfacial systems have been equilibrated for at least 100 ps and 1 ns, respectively. The value of the pressure in the bulk Lennard-Jones simulations, and the lateral pressure

profile in the interfacial simulations have then been evaluated over 200 ps and 5 ns long equilibrium trajectories, respectively.

7.1.2 Calculation of the Lateral Pressure Profile

The calculation of the pressure profiles is discussed in chapter 4 and in section 6.1.3.

7.2 Results and Discussion

Table 7.1. Spinodal Data of the Lennard-Jones Fluid

T^*	0.70	0.75	0.80	0.85	0.90	0.95
P^*	-0.99	-0.81	-0.71	-0.55	-0.46	-0.35
ρ^*	0.69 0.005	0.68 0.015	0.66 0.01	0.66 0.01	0.64 0.01	0.63 0.01

Figure 7.1 shows the pressure-density data obtained for the Lennard-Jones system at different temperatures. The spinodal pressure was simply regarded as the smallest of the obtained pressures along the given isotherm; its values obtained at different temperatures along with the corresponding densities are collected in table 7.1. In determining the pressure in these highly metastable systems we had to check carefully whether the system remained homogeneous in the entire course of the simulation. We monitored this both by following the time evolution of the pressure in the system and also by visual inspection of the configurations. In the case of bubble formation, happening typically upon approaching the spinodal, the pressure, previously fluctuating around a constant value, starts drifting to less negative values, as shown in figure 7.2, indicating the transition from a homogeneous metastable to a thermodynamically stable two-phase system. In such cases the pressure of the metastable homogeneous liquid was extracted by averaging only over the time range preceding the bubble formation, given that the metastable state persisted long enough to perform a meaningful averaging of the pressure. At even lower densities bubble formation occurred instantaneously, preventing us thus from calculating the metastable pressure. Fortunately, this always happened below the density where the pressure showed a minimum.

The lateral pressure profiles, obtained across the liquid-vapor interface of the Lennard-Jones fluid and water, are shown in figure 7.3, top and bottom respectively. The profiles are constant in the bulk vapor phase, and fluctuate around the same value in the bulk liquid phase, indicating that the two phases are indeed in equilibrium with each other. All the profiles exhibit a clear, deep minimum at the liquid side of the interface. The profiles shown are not symmetrized over the two interfaces present in the basic box. The difference between the two minimum values at the two interfaces can thus serve us as an estimate of

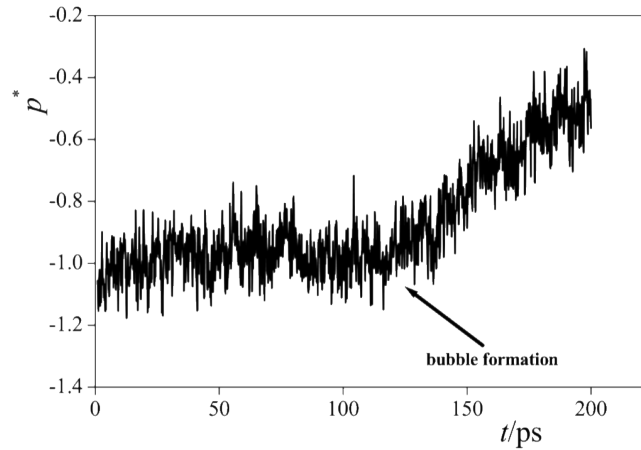


Figure 7.2. Time evolution of the pressure in the simulation of the bulk Lennard-Jones fluid, performed at the reduced temperature and density values of 0.7 and 0.71, respectively.

the uncertainty of the obtained interfacial spinodal values. The obtained minimum of the lateral pressure profiles are compared with the spinodal pressure values in figure 7.4 top and bottom for the Lennard-Jones fluid and water, respectively. As is seen, for water the spinodal pressure almost always agrees with the minimum value of the lateral pressure profile within error bars. The slight, few MPa difference observed at 280 K can easily be explained by the slightly different simulation setup used in the two calculations. The picture is, however, completely different for the Lennard-Jones fluid. Here the minimum value of the lateral pressure profile is consistently higher, but follows the same trend as the spinodal pressure in the entire temperature range studied. Moreover, the ratio of these two pressure values turns out to be around 1.65 in every case.

The observed different behavior of water and the Lennard-Jones fluid cannot simply be explained by the difference of the temperature ranges studied from the melting or critical point, because we found the ratio of the spinodal pressure and minimum of the lateral pressure profile temperature independent in both cases. Further, the range of temperatures studied starts right at the triple point temperature for both systems. Instead, it should be considered that the hypothesized equivalence of the minimum value of the lateral pressure in the interfacial system and of the spinodal pressure can be derived assuming the equivalence of the local free energy density in the interfacial system with that of a homogeneous system at the same density. However, for thermodynamic consistency, this equation needs to be supplemented with a term depending on the gradient of the density itself [42]. This fact could, in principle, be at the origin of the observed behavior, suggesting that this term is negligible for water but cannot be neglected in the case of the Lennard-Jones system.

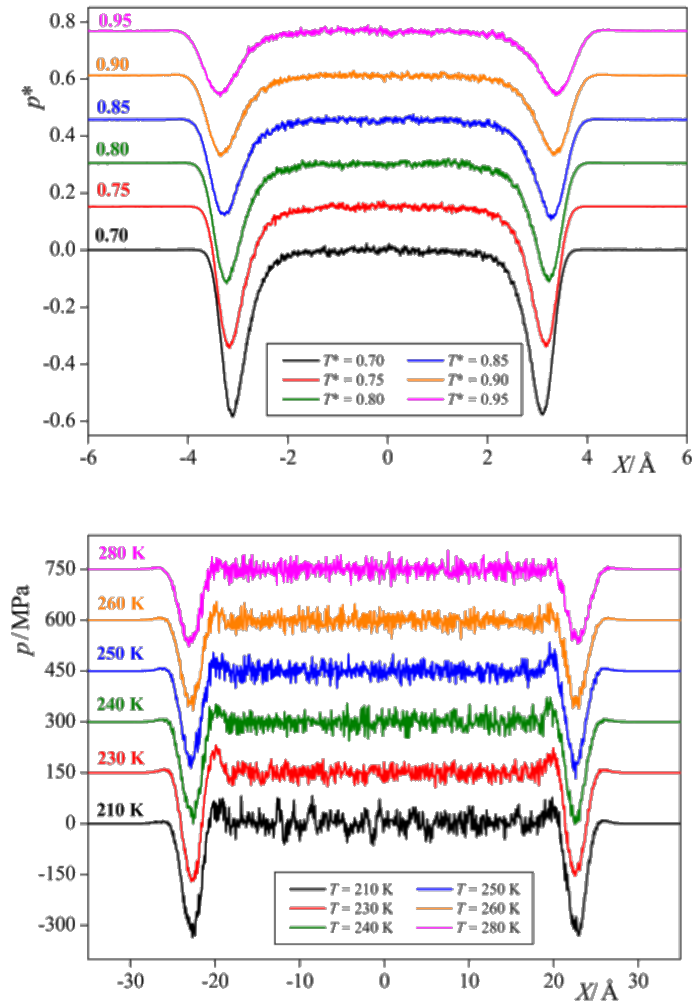


Figure 7.3. Lateral pressure profile of the Lennard-Jones fluid (top), and SPC/E water (bottom) along the liquid-vapor interface normal axis. The profiles converge to zero in the vapor phase, but have been shifted here for clarity.

7.3 Conclusion

The obtained results do not confirm, in general, the conjecture that the liquid spinodal can well be approximated with the minimum of the lateral pressure profile at the liquid-vapor interface. The two pressures are, nevertheless, found to be *proportional* with each other, their ratio being system dependent. This proportionality implies that the spinodal line could be reconstructed, if its value is known from an independent source at one single temperature (knowing also the critical point, the endpoint of the spinodal line). Such an independent source can be the approximation of the spinodal with the experimentally

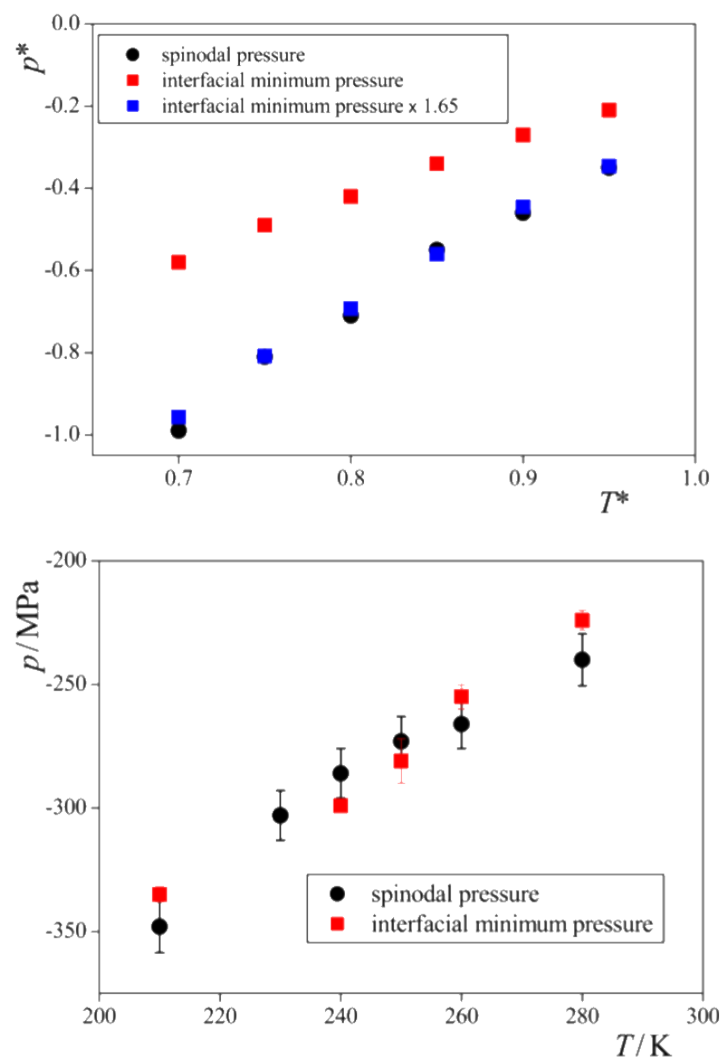


Figure 7.4. Comparison of the spinodal pressure of the Lennard-Jones fluid (top) and SPC/E water (bottom). The error bars are only shown when larger than the symbols.

measurable limit of overheat [191]. Finally, it should also be noted that although the approximation of the spinodal pressure by the minimum of the interfacial lateral pressure profile was not found to work in general, it works well in the case of water, the particular liquid for which knowing at least the approximate location of the liquid spinodal is by far of the greatest practical importance. Thus, the present results provide also a simple way of estimating the spinodal pressure of water both for practical applications and for fine tuning parameters in appropriate equations-of-state.

Chapter 8

Lateral Pressure Profile and Free Volume Properties in Phospholipid Membranes Containing Anesthetics

In spite of the fact that general anesthetics are routinely used in the everyday surgical practice for more than one and a half centuries, and that it is also known for more than a century that they act in the membrane of certain cells, still very little is known about the molecular mechanism of general anesthesia. Some hypotheses assume that anesthesia is caused by the specific interaction between the anesthetic molecules and certain membrane-bound proteins [192–196]. However, in the frame of such *protein theories* it is very difficult to account for the large chemical variety of the general anesthetics. Further, neither the protein(s), nor their active site(s) responsible for the anesthetic action have been unambiguously identified yet.

Alternative explanations, called *lipid theories* conjecture that anesthetics alter certain properties of the lipid matrix, which, in turn, alters the conformation, and hence also the function of certain proteins [124, 197–203]. Several such properties of the lipid membrane have been hypothesized to be behind the molecular mechanism of anesthesia in the past six decades. Thus, in his *critical volume hypothesis*, Mullins claimed that anesthesia occurs if the molar volume of the membrane exceeds a certain limit [197]. This assumption was later rationalized by claiming that anesthetics increase the ordering of the lipid tails, which leads to an increased thickness of the membrane [202–204]. In some other studies the fluidity of the membrane was thought to be the relevant property in this respect [205, 206]. Although a number of experimental [202, 203, 205, 206] and computer simulation studies [207–210] provided results that are consistent with the above hypotheses, other

studies found these properties to be insensitive to the presence of anesthetics [211–215], or even provided results contradicting some of these assumptions [216–219].

This controversy of the existing results largely originates from the fact that different anesthetics as well as membranes of different compositions have been considered in the different studies. Nevertheless, any possible explanation of the molecular mechanism of anesthesia in the frame of the lipid theories has to be valid for all general anesthetics as well as for all reasonable models of the cell membrane. Moreover, as it has been well-known since the 1950s, the anesthetic effect is reverted at elevated pressures, that is, at about 100-200 bar [205, 220–222]. Thus, any such explanation has to also account for this pressure reversal.

As mentioned at the beginning of chapter 4, in 1997 Cantor suggested that the relevant membrane property lying behind the molecular mechanism of anesthesia might be the lateral pressure profile [124]. According to this suggestion, anesthetics modify this profile in such a way that it changes the conformational equilibrium and hence also the function of certain proteins. Although this hypothesis became rather popular in the past years, its experimental test seems to be almost impossible, as it would require the measurement of certain components of the pressure tensor with an angstrom resolution. On the other hand, the problem can be addressed with the computational methods developed in 4, and already demonstrated in chapters 5, 6 and 7. In the following, the method is applied to study the molecular mechanism of anesthesia.

In recent publications, fully hydrated dipalmitoylphosphatidylcholine (DPPC) bilayer were studied, as a simple model of the cell membrane, in the absence of anesthetics as well as in the presence of four widely used general anesthetic molecules, namely, chloroform, halothane, diethyl ether, and enflurane, both at atmospheric pressure and at 1000 bar, considering both the gel (β) [223] and the biologically more relevant liquid crystalline (α) phase [224] of the bilayer.

The main approach was based on the idea that relevant membrane properties related to anesthesia must change in the same way upon addition of any general anesthetics, and in the opposite way upon increasing the pressure. Although a number of the membrane properties (density profiles, tail and headgroup orientation, tail ordering,...) were tested, it was shown that only the lateral membrane density (or area per headgroup) meets the above two criteria. The finding that, in systems where anesthesia is supposed to occur, the area per headgroup value exceeds a certain threshold is also consistent with the old critical volume hypothesis of Mullins [197], although it rationalizes this hypothesis in a different way than what was thought for a long time, namely, through the increase of the area rather than the thickness of the membrane.

Among the membrane properties investigated so far, the lateral pressure profile is missing, due to reasons related to the technical difficulties discussed in chapter 4. Having at hand an efficient tool to calculate the local pressure, including also long-range interactions [225], enables us to calculate the lateral pressure profile also in lipid membranes in a computationally feasible way. Therefore, we have repeated the simulations, performed at 310 K, corresponding to the biologically more relevant α phase of the bilayer, by also calculating the pressure profile in the membrane. To further investigate the origin of the observed effect of the anesthetics and overall pressure on the lateral density, we have performed a detailed analysis of the free volume properties of the membrane, using the Voronoi-Delaunay method [65, 110–112], both in the presence and absence of anesthetics as well as both at atmospheric and high pressure. Again, we are looking for changes that occur in the same direction upon addition of any of the anesthetics considered, but in the opposite direction upon increasing the pressure.

8.1 Computational Details

8.1.1 Molecular Dynamics Simulations

Simulations of the fully hydrated neat DPPC bilayer as well as bilayers containing four different general anesthetics, namely, chloroform (CF), halothane (HAL), diethyl ether (DE), and enflurane (ENF) have been performed on the isothermalisobaric (N,P,T) ensemble at pressures of 1 and 1000 bar. The temperature of the systems has been kept at 310 K. The rectangular basic simulation box has consisted of 256 DPPC molecules, arranged in a bilayer containing 128 molecules in each of the two leaflets. To ensure full hydration, which requires the water to lipid molar ratio to exceed 29.1 [226], 8132 water molecules have been used. In the systems containing anesthetics, 112 chloroform, 72 halothane, 192 diethyl ether, or 96 enflurane molecules have also been placed in the hydrocarbon region of the membrane. The number of the anesthetic molecules has been chosen in such a way that they correspond to roughly the same anesthetic mass density in all four systems. The molar fraction of the anesthetic molecules used in the simulations well exceeds what is used under surgical conditions, in order to magnify any possible effect of them on the membrane properties, as suggested by Oh and Klein [208]. For similar reasons, the pressure of 1000 bar used in the high pressure simulations is also considerably higher than what is needed for pressure reversal.

DPPC molecules have been modeled using a GROMOS87-based force field [227], developed specifically for lipids. According to this potential model, the CH, CH₂, and CH₃ groups have been treated as united atoms. This model of DPPC is known to be in the biologically more relevant α phase at $T = 310$ K and $p = 1$ bar [228]. Chloroform,

diethyl ether, and enflurane molecules have been described by the GROMOS96 force field [229–231], while for halothane the potential model of Scharf and Laasonen [232] has been used, whereas water molecules have been described by the rigid, three-site SPC potential [233]. The geometry of the water molecules as well as all bond lengths of the DPPC and anesthetic molecules have been kept fixed by means of the SHAKE algorithm [98]. Angular and torsional flexibility of DPPC and the anesthetics has been allowed, according to the force fields used. All interactions have been truncated to zero beyond the group-based center-center cutoff distance of 9.0 Å. The long-range part of the electrostatic interaction has been accounted for using the smooth particle mesh Ewald (sPME) method [28].

The simulations have been started from already equilibrated configurations obtained from our previous work [224], and have been performed using the modified version of the GROMACS 5.1 molecular dynamics simulation package [99], which also distributes the lateral pressure among all the atoms present in the basic box. The equations of motion have been integrated in time steps of 2 fs, using the leapfrog algorithm. The temperature and pressure of the systems have been controlled by means of the Nosé-Hoover thermostat [32, 33] and Parrinello-Rahman barostat [34], respectively, using the characteristic time of 0.5 ps in both cases. Pressure has been controlled in an anisotropic way, namely, separate couplings have been employed along all three spatial directions. The lateral pressure profile has been calculated over a 20 ns long equilibrium trajectory in each system, whereas for the calculation of the free volume characteristics, 2000 sample configurations per system, separated by 10 ps long trajectories each, have been saved. Equilibrium snapshots of the 10 systems simulated are shown in figure 8.1. Finally, all profiles calculated have also been averaged over the two sides of the membrane, therefore, in the following they will always be shown only in one side of the membrane.

8.1.2 Calculation of the Lateral Pressure Profile

The details of the calculation of the pressure profiles are presented in detail in chapters 4 and 5.

8.1.3 Calculation of the Free Volume Characteristics

Free volume properties are traditionally analyzed using the Voronoi and Delaunay tessellations in the system of interest [65, 111]. However, in its original formulation, the Voronoi-Delaunay method assumes that the system to be studied consists of points (or spheres of equal radii, such as in atomic systems). When studying molecular systems, which are built up by spherical particles of different radii, the original method needs to be improved. To keep the underlying physical concept unchanged, one should use the Voronoi S-tessellation [234, 235], where the distance of a spatial point is measured from

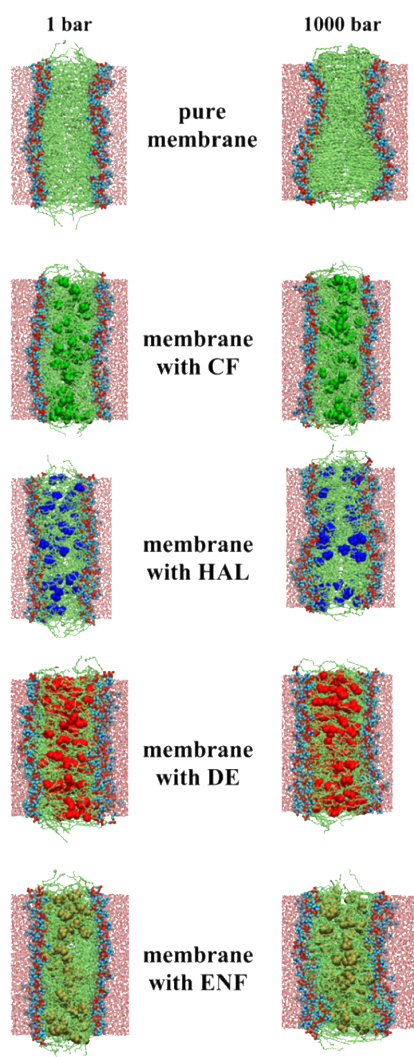


Figure 8.1. Equilibrium snapshot of the 10 systems simulated. Anesthetic molecules are shown enlarged for better visibility (CF: green, HAL: blue, DE: red, ENF: olive)

the surface rather than from the center of the atoms. Hence, the Voronoi S-region is the locus of the spatial points that are closer to the surface of a given atom than to that of any other atoms. Besides the Voronoi S-region, the other important construction of the method is the Delaunay S-simplex (tetrahedron), defined by four mutually neighboring atoms. The radius of the largest empty sphere that can be inscribed between these atoms characterizes the size of the interstitial void located between them. The position and radius of these interstitial spheres can be calculated simultaneously with the tessellation itself [235], while the volume of the Delaunay simplices themselves can easily be obtained by means of elementary geometry.

In contrast to the interstitial spherical cavities, the determination of the entire empty

volume of irregular shape located between the atoms is a considerably more complicated task. First, while the ordinary Voronoi regions are convex polyhedra with flat faces, the Voronoi S-regions have curved faces, and thus their volume can only be calculated numerically [236]. This makes the use of the Voronoi S-tessellation unsuitable for volumetric studies, since such studies need accurate and fast calculations. A reasonable compromise between computational cost and accuracy can be the use of the power (radical) Voronoi-Delaunay tessellation [110, 237, 238], where the faces of the Voronoi regions are defined by the planes from the points of which the tangents drawn to the two spheres are of equal lengths. In systems where the radii of the various atoms do not differ much from each other, such as in the present case, the power Voronoi tessellation retains the physical meaning of the original method, as in such cases the power Voronoi regions provide a very good approximation of the Voronoi S-regions. Another difficulty stems from the presence of strongly overlapping, chemically bound atoms. Several approaches have been proposed previously to overcome this problem, involving either the calculation of the volume of the overlapped regions of the atoms [239], or that of the voids [240]. Here, we use an approach based on Delaunay subsimplices [241], in which the occupied volume of the Delaunay simplices are calculated with analytical formulas for arbitrary systems of overlapping atoms [242]. This method was already used to calculate the volumetric characteristics of proteins in aqueous solutions [243].

An important characteristic of lipid bilayers is the profile of free volume along the axis perpendicular to the plane of the membrane. This profile can be calculated in several ways, for example, by placing sample points in the system, either randomly or along a grid [244–247]. Having the power Voronoi-Delaunay tessellation of the system determined, however, the profile of the free volume fraction, ε , can readily be calculated as the sum of the empty volumes of the Delaunay simplices located in the different slices of the system, normalized by the total volume of these simplices themselves.

8.2 Results and Discussion

8.3 Lateral Pressure profiles

The lateral pressure profiles obtained in the pure membrane at 1 bar as well as in the anesthetic containing membranes both at 1 and 1000 bar are shown and compared in figure 8.2. The pressure profiles exhibit a constant plateau in the bulk aqueous phase around the P value corresponding to the overall pressure of the system. This plateau is followed by a clear maximum at about $X = 20 \text{ \AA}$, and a minimum around the X value of 12-13 \AA . The position of the peak corresponds to the dense region of the lipid headgroups, while that of the minimum is close to the average position of the C=O groups of the lipid

tails [224]. In the hydrocarbon phase, the profile is again roughly constant, apart from the marked peak occurring at $X = 0 \text{ \AA}$, right in the middle of the membrane. It should be noted that here the density of the membrane is of minimum [224], therefore, the presence of this lateral pressure maximum cannot simply be explained by the effect of the density. Instead, it is sensible to assume that the outer part of the hydrocarbon phase is characterized by a rather homogeneous distribution of the atoms, which is reflected in the more or less constant value of P_L . By contrast, in the middle of the membrane the spatial distribution of the atoms exhibits larger fluctuations, relatively large voids are surrounded by rather crowded patches, and the presence of these high density patches leads to the relatively high lateral pressure value. This explanation is also in accordance with our earlier finding that the middle of a phospholipid membrane is characterized by larger but considerably less spherical voids than the outer part of the hydrocarbon region [234].

The increase of the pressure of the system leads, as expected, to the corresponding overall shift of the entire lateral pressure profile, without altering much of its shape. The inclusion of the anesthetic molecules has a much smaller effect on the lateral pressure profile. Nevertheless, it leads to a slight shift of the minimum position away from the membrane interior and, correspondingly, to a clear decrease of the lateral pressure in the X range of 13-18 \AA in every case. This range corresponds to the lipid side of the headgroup region, where the glycerol backbone of the DPPC molecules as well as the ester groups linking the fatty acid tails to this backbone are located. In this region, the behavior of the lateral pressure profile meets both of our criteria, namely, it is changed in the same way upon the addition of all the anesthetic molecules considered, and it is changed in the opposite way by increasing the overall pressure. This change might thus be related to the molecular mechanism of anesthesia.

Since in calculating the lateral pressure profile the pressure contributions were distributed among the different atoms, it is straightforward to separate the contributions of the lipid, anesthetic, and water molecules to the entire $P_L(X)$ profile. This separation is shown in figure 8.3 for the anesthetic containing systems simulated at 1 bar. To further analyze the origin of the above-discussed change of the $P_L(X)$ profile in the X range of 13-18 \AA , we have calculated the difference of the lipid, anesthetic, and water contributions to the $P_L(X)$ profile between the anesthetic-containing and pure membrane at 1 bar in every case. The obtained results are shown in figure 8.4. The anesthetic molecules always increase the lateral pressure in the membrane interior, where they are located. In the middle of the membrane, the lipid contribution is decreased in the presence of anesthetics, presumably due to the lateral expansion of the membrane [224]. In the X range relevant here, meaning in the region $13 \text{ \AA} < X < 18 \text{ \AA}$, both the lipid and the water contribution to $P_L(X)$ is decreased in the presence of anesthetics. Clearly, the anesthetic

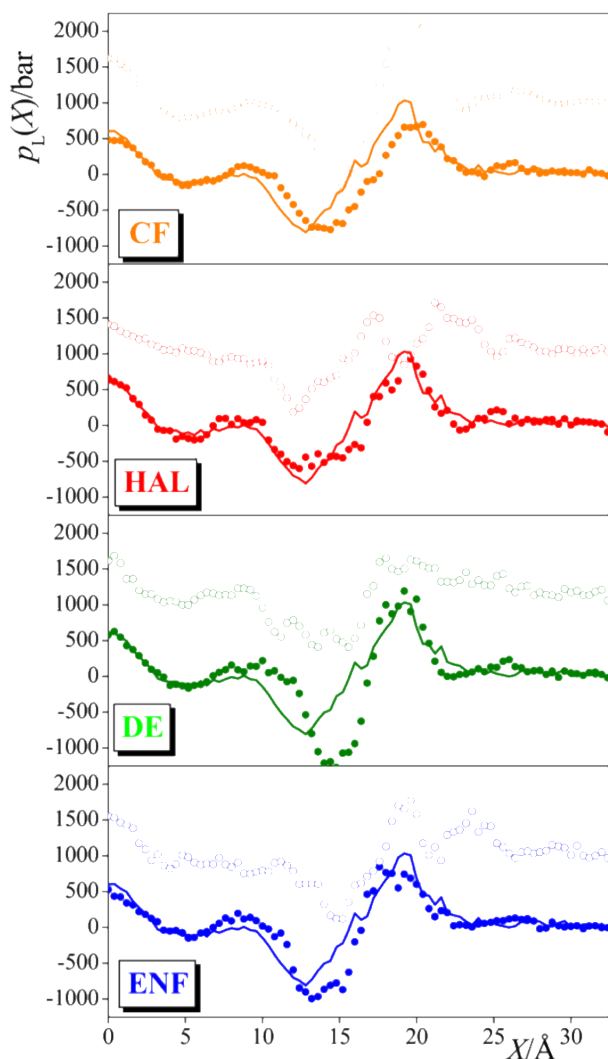


Figure 8.2. Comparison of the lateral pressure profile across the pure lipid membrane at 1 bar (solid curves) with the membranes containing anesthetics, simulated at 1 bar (filled circles) and 1000 bar (open circles). $X = 0$ Å corresponds to the middle of the bilayer.

molecules themselves do not reach this part of the membrane, they always stay somewhat closer to the middle of the bilayer [224]. On the other hand, water molecules can penetrate into this region [248, 249], as the O atoms and polar ester (C-O-C=O) groups of the lipid tails are located here [224]. The observed decrease of the lateral pressure in this part of the membrane can be attributed to the fact that the anesthetic molecules are accumulated in the immediate vicinity of this region, but do not penetrate here, and hence the effect of the anesthetic-induced lateral expansion of the membrane [224] is expected to be the strongest here.

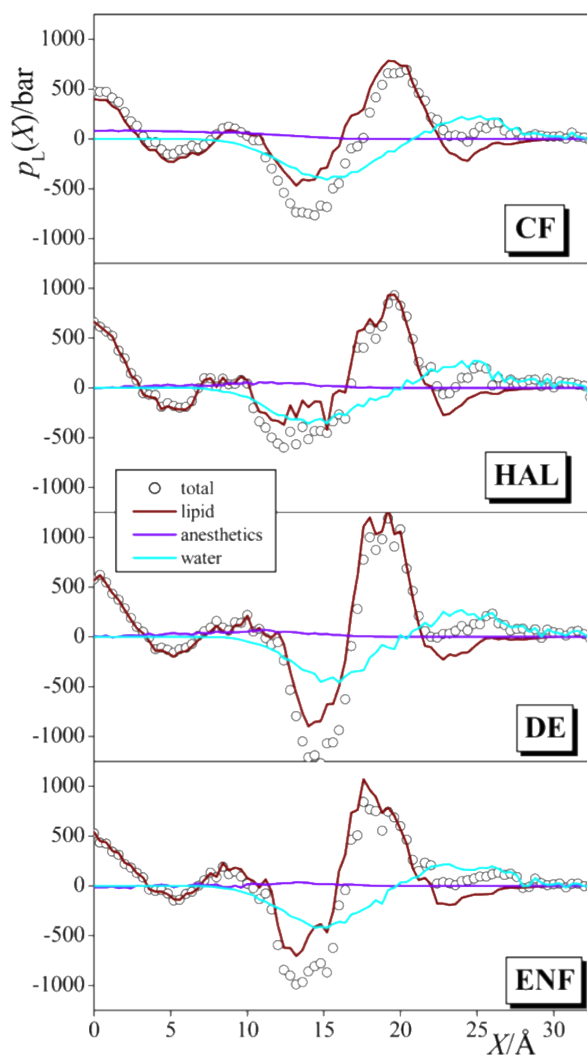


Figure 8.3. Total lateral pressure profile across the membranes simulated at 1 bar (black open circles), along with the contributions given by the DPPC (brown solid lines), anesthetic (violet solid lines), and water molecules (cyan solid lines). $X = 0 \text{ \AA}$ corresponds to the middle of the bilayer.

8.4 Free Volume Properties

In analyzing the voids in the different membranes, the simplest characteristics to be discussed is the size distribution of the elemental spherical vacancies located between the atoms. As it was described above, these interstitial voids are determined by the Delaunay tessellation of the system, namely, each void corresponds to the center of the Delaunay simplex formed by four mutually neighboring atoms [234]. This fact allows us not only to determine these spherical voids, but also to assign them to different parts of the system

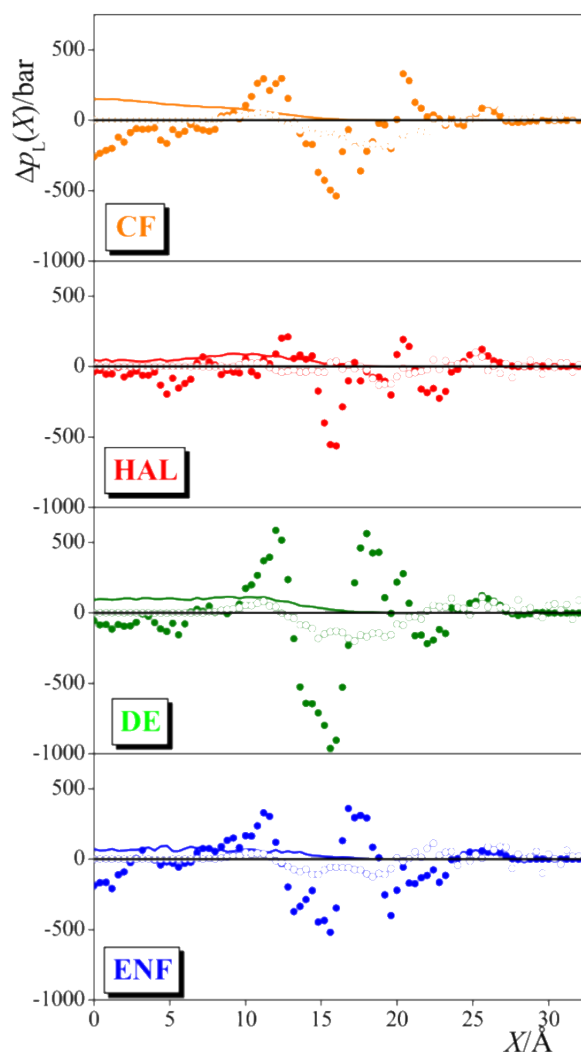


Figure 8.4. Difference between the lateral pressure profile contributions of the DPPC (full circles), anesthetic (solid curves), and water molecules (open circles) as obtained in the anesthetic-containing and pure membranes at 1 bar. $X = 0 \text{ \AA}$ corresponds to the middle of the bilayer.

according to the atoms forming the corresponding Delaunay simplices. Thus, here we defined an elemental void to belong to the lipid phase of the system if all the four atoms forming its Delaunay simplex belong to a DPPC (or anesthetic) molecule. Similarly, voids corresponding to Delaunay simplices formed by four water atoms are regarded to belong to the water phase of the system, whereas those corresponding to Delaunay simplices formed both by lipid and water atoms are regarded to belong to the interfacial region of the system.

The distribution of the radius R_i of the elemental interstitial voids belonging to these

Table 8.1. Empty volume in units of 10^6 \AA^3 associated with the different molecules in the different membranes simulated

	DPPC		anesthetic		water	
	1 bar	1000 bar	1bar	1000 bar	1 bar	1000 bar
pure membrane	105.1 ± 0.9	88.1 ± 0.8	0	0	110.8 ± 0.6	101.4 ± 0.6
membrane + CF	108.0 ± 0.9	90.0 ± 0.7	9.2 ± 0.2	7.5 ± 0.1	110.9 ± 0.7	101.4 ± 0.6
membrane + HAL	105.7 ± 0.9	84.8 ± 0.8	5.6 ± 0.1	4.6 ± 0.1	110.8 ± 0.7	101.2 ± 0.6
membrane + DE	104.9 ± 0.8	91.5 ± 0.6	13.2 ± 0.2	11.3 ± 0.1	110.6 ± 0.6	101.3 ± 0.6
membrane + ENF	104.5 ± 0.9	88.3 ± 0.6	7.8 ± 0.2	6.5 ± 0.1	110.7 ± 0.7	101.3 ± 0.6

three different parts of the system is shown in figure 8.5 as obtained in the pure membrane at 1 bar as well as in the membranes containing chloroform both at 1 and 1000 bar. (Similar distributions have been obtained with the other anesthetic molecules, as well.) As is seen, the inclusion of anesthetics in the membrane does not alter the $P(R_i)$ distributions in the water phase and in the interfacial region, but shifts the distribution to slightly higher values in the lipid part of the system. This finding is not surprising, since the anesthetic molecules are located deeply inside the hydrocarbon phase of the membrane. Further, as it is expected, the increase of the pressure shifts all these distributions to lower values. Table 8.1 shows the empty volume corresponding to the lipid, anesthetic, and water molecules, as obtained in the different systems simulated. As it was described above, the total volume of the Voronoi cell of an atom can be divided into “occupied” and “empty” parts, the former being covered by the given atom itself, while the latter is not. Since the occupied volume of a Voronoi region simply reflects the size of its central atom, it is sensitive neither to the pressure nor to the presence of the anesthetics. The amount of the empty volume, on the other hand, is characteristic of the local arrangement of the atoms. As it is seen from table 8.1, the empty volume corresponding both to the lipid and to the water molecules agree, within error bars, as obtained in the pure and anesthetic containing membranes at 1 bar in every case. On the other hand, considerably large empty volume is associated with the anesthetic molecules themselves in every case. In other words, the increase of the empty volume corresponding to the inclusion of the anesthetic molecules, evidenced by the lateral expansion of the membrane [224], is localized to the immediate vicinity of the anesthetic molecules. This finding is in line with our previous result that the presence of anesthetic molecules induces a decrease of the lateral pressure in the membrane region located in the immediate vicinity of the preferred position of the anesthetic molecules. Finally, as it is expected, the increase of the pressure leads to a marked decrease of the empty volume in every case, reverting thus the increase of the empty volume associated with the presence of the anesthetic molecules.

The profile of the free volume fraction, ε , across the membrane is shown in figure 8.6,

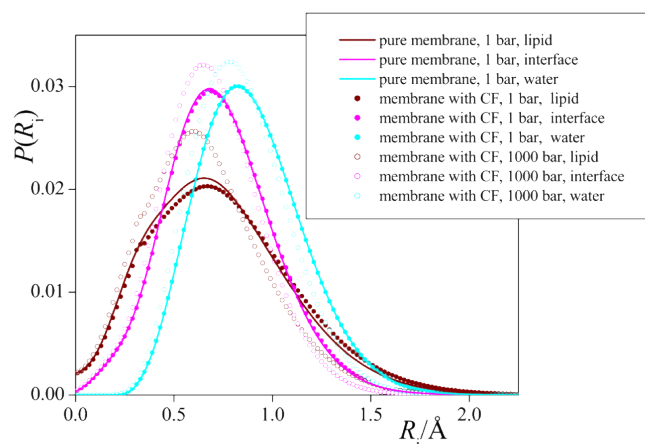


Figure 8.5. Distribution of the radius of the elemental spherical interstitial voids in the lipid phase (brown), interfacial region (magenta), and water phase (cyan) of the pure membrane simulated at 1 bar (solid curves), as well as in the chloroform containing membranes simulated at 1 bar (filled circles) and 1000 bar (open circles).

again as obtained in the pure membrane at 1 bar as well as in the anesthetic containing membranes both at 1 and 1000 bar. Clearly, the increase of the pressure leads to the decrease of the empty volume fraction across the entire membrane. The inclusion of the anesthetic molecules in the membrane has a more subtle effect on the free volume profile. In general, it decreases the fraction of free volume, or leaves it unchanged at the aqueous side, and increases it at the lipid side of the dense headgroup region. Although there are several differences between the behavior of the different anesthetic molecules in this respect, the fraction of the empty volume is noticeably increased in their presence in the X range between about 8 and 16 Å in every case. This X range largely overlaps with that corresponding to the decrease of the lateral pressure (between about 13 and 18 Å), but extends also somewhat toward the membrane region in which the anesthetic molecules are located. It should be noted that, as described in a previous paper [224], anesthetic molecules prefer two distinct positions along the membrane normal axis in every case, namely, the middle of the membrane, and the X range around 10 Å, although the relative weights of these two preferences can vary from anesthetic to anesthetic [219, 224].

Consistently, the fraction of the free volume is typically increased by the anesthetic molecules in both of these two regions; however, it is only the outer of these two regions in which *all* the anesthetic molecules considered leads to a clear increase of it.

Thus, our findings indicate that the increase of the empty volume in the membrane in the presence of anesthetics, associated with the anesthetic molecules themselves, leads to an overall increase of the fraction of empty volume in the membrane region where the

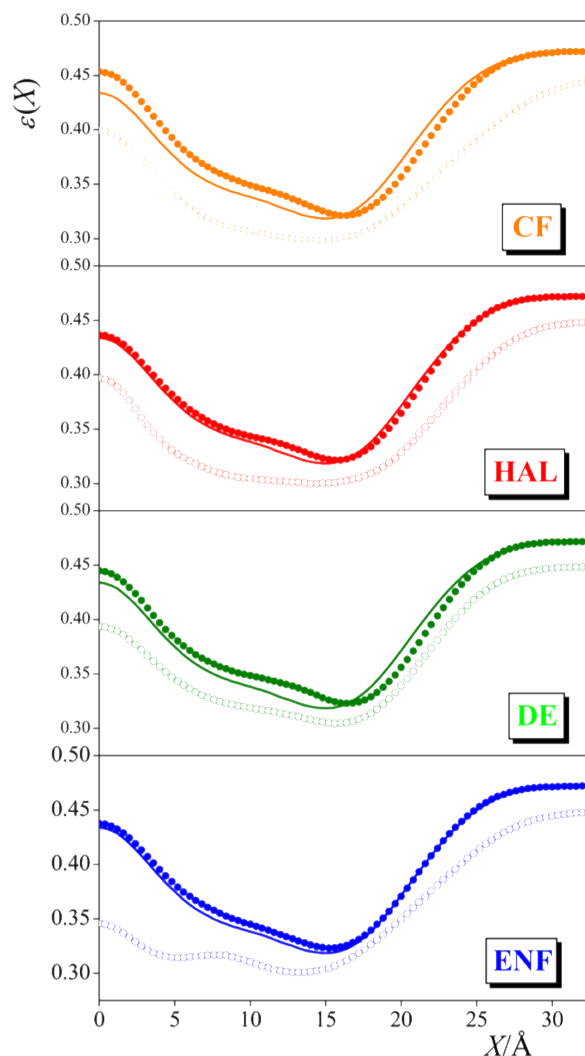


Figure 8.6. Profile of the fraction of empty volume in pure lipid membrane at 1 bar (solid curves), compared with that in the membranes containing anesthetics, simulated at 1 bar (filled circles) and 1000 bar (open circles). $X = 0 \text{ \AA}$ corresponds to the middle of the bilayer.

anesthetic molecules are located, and also in the immediate vicinity of this region at its headgroup side. This results in a decrease of the lateral pressure in the region of the ester groups of the DPPC molecules, located right next to the membrane region in which the anesthetic molecules are accumulated. These changes are clearly reverted by the increase of the pressure, and hence they might be behind the molecular mechanism of anesthesia.

8.5 Conclusion

In a previous study, it was found that anesthetic induced lateral expansion of the membrane might be a process that is relevant for the molecular mechanism of anesthesia, because such a lateral expansion was observed upon the introduction of all anesthetic molecules considered, and this effect was clearly reverted by the increase of the pressure [224]. This finding was also consistent with the more than 60 years old critical volume hypothesis of Mullins [197]. In this chapter, we analyzed in detail the origin of this anesthetic induced lateral expansion, and related it also to the hypothesis of Cantor, who claimed that anesthetics induce some changes in the lateral pressure profile of the lipid membrane, which alters the conformational equilibrium of certain membrane-bound proteins [124]. In order to calculate the lateral pressure profile, we used the computationally feasible method described in chapter 4.

Previously, it was also shown that anesthetics prefer two distinct positions in the membrane. The first of these positions is right in the middle of the membrane, while the second one is located at the outer edge of the hydrocarbon phase, close to the region of the C=O groups of the lipid tails [224]. This finding was in agreement with the results of earlier coarse-grain simulations [250], and was later confirmed also by Chen et al. [219]. Here, we have demonstrated that anesthetics located close to the C=O groups might be related to the aforementioned lateral expansion, and thus be responsible for the molecular mechanism of anesthesia. Thus, although in the presence of certain anesthetics the fraction of the empty volume is increased around both of these preferred positions, it is only at the outer position where this increase of empty volume occurs in the presence of *all* anesthetics considered. Further, the presence of anesthetics is found not to alter the lateral pressure in the middle of the membrane, but to decrease it in the region of the ester groups of the lipid tails, very close to the outer preferred position of the anesthetic molecules.

We have shown here that the additional free volume occurring in the membrane upon addition of the anesthetics is localized right around the anesthetic molecules themselves, and thus, the empty volume increases in the region where anesthetics are preferentially located. This increase of the empty volume results in a decrease of the lateral pressure in the nearby region of the ester groups, where the anesthetic molecules do not penetrate. In other words, the lateral pressure decreases where the lateral expansion induced by the presence of anesthetics is not accompanied by the occurrence of additional molecules. This way, we have found a link between the critical volume hypothesis of Mullins [197] and the lateral pressure hypothesis of Cantor [124]. Thus, by contrast to earlier claims [202–204], the increase of the membrane volume upon addition of anesthetics is caused by the lateral

expansion rather than the thickening of the membrane [224]. This lateral expansion is the strongest in the membrane region of the ester groups, where anesthetics do not penetrate, but it is right next to the outer of their two preferred positions. This leads to a clear decrease of the lateral pressure in this region, an effect that can simply be reverted by the increase of the overall pressure. As a consequence, given that indeed this change of the lateral pressure profile lays behind the molecular mechanism of anesthesia, the conformational changes of the relevant membrane bound protein molecules, predicted by Cantor [124], are also expected to occur in this region of the ester groups of the membrane.

Chapter 9

Ammonia Clathrate Hydrate As Seen from Grand Canonical Monte Carlo Simulations

Ammonia is an abundant molecule in the universe. Its presence has widely been evidenced in the interstellar medium [251] as well as in the primitive matter of the solar system (meteorites, comets) and in the atmospheres of Jupiter and Saturn, the two gas giants orbiting the Sun. Ammonia is also assumed to be the main source of the molecular nitrogen dominating Titan's atmosphere [252]. The ammonia content and ammonia/water ratio seems also to be critical in search for amino acids, which are the basic building blocks of life [253].

As stellar bodies may have preserved ammonia in the form of ammonium silicates or in ice, the presence of ammonia hydrates has been hypothesized in Saturn's largest moon Titan [254, 255], and also evidenced on the surfaces of the minor planets like Charon [256] and Orcus [257] via observations in the near-infrared range. The presence of ammonia hydrate, together with crystalline water ice, has been invoked as evidence for past, or even present, cryovolcanism on object of the Kuiper Belt [258].

On the other hand, ammonia is suspected to modify the stability regions of solid ice and methane clathrate phases on various moons in the Solar System [259]. Indeed, it has been experimentally shown that the hydrophilic behavior of ammonia does not disqualify this properly sized molecule from being incorporated into clathrates, together with a more hydrophobic guest that is known to easily form stable clathrates [259]. Ammonia may even form clathrate hydrates between 100 and 150 K, with only ammonia as guest [259], as shown by some peak positions in X-ray diffraction measurements that can be

unambiguously assigned to the ammonia clathrate hydrate with cubic structure I (sI) [259]. The stability of this sI clathrate structure, together with a detailed analysis of the hydrogen bonding between water and ammonia molecules, has then been theoretically investigated by molecular dynamics (MD) simulations, showing that the pure sI NH_3 clathrate decomposes in the simulations between 220 and 240 K, depending on the water force field used [260].

Indeed, considering both the paucity of experimental data on the ammonia clathrate itself and the lack of a fundamental understanding of how the NH_3 molecule may affect the phase behavior of other clathrates, computer simulation appears to be an ideal tool for providing the missing insight at the atomistic level.

Thus, MD simulations have been performed by various researchers to characterize not only the structure and the stability of pure NH_3 , but also of binary $\text{NH}_3 + \text{THF}$ (tetrahydrofuran) and $\text{CH}_4 + \text{NH}_3$ clathrates from 100 to 240 K, in close relation with the corresponding experimental work [259, 260]. However, such simulations, performed on the isothermal-isobaric ensemble, suffer from their dependence on the initial conditions, especially regarding the clathrate composition that has to be fixed in the calculations. Moreover, it is sometimes difficult with MD to know if the simulated system corresponds to a real equilibrium structure or if it is stuck in a metastable state, even when performing very long simulation runs. Because the abundance of the trapped gases in the hosting cages of the clathrates under consideration is one of the most important data sought, calculations performed on the grand canonical ensemble, where the number of guest molecules is not fixed in the simulations, may appear to be much more appropriate. In simulations performed on the grand canonical ensemble, such as grand canonical Monte Carlo (GCMC) [1, 38] simulations, the chemical potential rather than the number of the molecules is fixed. Therefore, performing a set of GCMC simulations, in which the chemical potential of the molecules in contact with the absorbent system is systematically varied, the occupancy isotherm, that is, the number of enclathrated molecules as a function of their chemical potential, can be conveniently calculated. Surprisingly this method has only scarcely been applied to clathrate systems since the pioneering work of Tanaka [261, 262], although it has proven to be very efficient for directly calculating the composition of methane [263, 264], hydrogen [265], binary hydrogen/THF [266], and binary CO/N_2 [267] clathrates under various thermodynamic conditions.

In this chapter, the first GCMC simulation study is presented of the trapping of NH_3 molecules in the cages of a clathrate hydrate of structure I in the very low temperature range of 100-180 K, which was also experimentally investigated [259]. Besides calculating the trapping isotherm, the detailed analysis of the clathrate structure is also performed at various ammonia abundances. In section 9.1, details of the calculations performed are

given. The obtained results concerning the occupancy isotherm and properties of the resulting systems are presented and discussed in detail in section 9.2. Finally, in section 9.3, the main conclusions are briefly summarized.

9.1 Grand Canonical Monte Carlo Simulations

The trapping of NH_3 molecules in the clathrate hydrate lattice has been investigated by performing a set of Monte Carlo simulations on the grand canonical (μ, V, T) ensemble at three temperatures, namely 100, 150, and 180 K. Simulations have first been performed with a rigid clathrate, meaning in a system where the water molecules have been fixed at the equilibrium positions of a clathrate of structure I (sI), with fixed orientations. While the number of water molecules in the simulation box has been kept constant, the number of ammonia molecules trapped by the rigid network of water has been calculated by increasing the chemical potential, μ , of the NH_3 molecules from values corresponding to empty clathrate lattice to values corresponding to twice the number of cages. The isotherms were obtained as the average number of NH_3 molecules, $\langle N \rangle$, in the simulation box as a function of the chemical potential, and will be referred to as occupancy isotherms because the number of enclathrated ammonia molecules is calculated [263]. Simulations have been performed with simulation boxes based on both 2 and $3 \times 3 \times 3$ replicas of the sI unit cell, taken from Takeuchi et al. [268], to test the influence of the size of the simulation box in the calculated isotherms. The $2 \times 2 \times 2$ replica of the unit cell of sI clathrate consisted of a total of 368 water molecules forming a network of 48 large and 16 small cages. The edge length of this cubic box was 24.06 Å in every direction, in agreement with the periodicity of the clathrate lattice. The larger, $3 \times 3 \times 3$, replica of the unit cell corresponded to a network of 1242 water molecules forming 162 large and 54 small cages in a cubic simulation box with the edge length equal to 36.09 Å.

Then, the GCMC method has also been applied to a flexible clathrate model, in which rotational and translational degrees of freedom of the water molecules have also been considered. However, no chemical potential value has been assigned to the water molecules, and thus, insertion/deletion steps have not been considered for water molecules in the GCMC calculations. Nevertheless, this treatment has resulted in a large increase of the corresponding computational cost and, as a consequence, simulations with flexible clathrates have only been performed with the $2 \times 2 \times 2$ simulation.

To facilitate the comparison of our results with those of the molecular dynamics simulations of Alavi et al. [260], water molecules have been described by the TIP4P/Ice potential [269]. This potential was shown to reproduce more accurately the decomposition temperature of methane hydrate while also giving better predictions regarding the lattice

constants, as compared to the TIP4P model [270]. Moreover, the fact that TIP4P/Ice tends to form less hydrogen bonds with the NH_3 molecules increases the likelihood of the clathrate being stable in the temperature range of the simulations [260]. The NH_3 molecules have been represented by the OPLS force-field of Rizzo and Jorgensen [271], again to ensure comparability. Based on these models, the potential energy has been calculated as the sum of the pairwise interaction energies between molecules, where the interaction energy between two molecules is defined as the sum of the Lennard-Jones and Coulomb contributions of all pairs of their interaction sites. For the potential models used here, these interaction sites are located at the atomic positions, with the exception of the TIP4P/Ice model, which contains also a nonatomic site slightly displaced from the O atom, along the water molecular axis [269].

All interactions have been truncated to zero beyond the distance of 12.03 and 18.04 Å for the small and large simulation boxes, respectively. The long-range contribution of the electrostatic interaction has been accounted for by the reaction field correction method [272, 273] under conducting boundary conditions.

Monte Carlo simulations have been performed using the MMC code that has been widely applied for studying the adsorption process of a number of atmospherically relevant molecules at the surface of ice [274–277], showing a fair agreement with the corresponding experimental results when available. In every Monte Carlo step, a translational and rotational move was attempted with 50% probability on a randomly chosen molecule, along a randomly chosen axis parallel to one of the edges of the simulation box. The maximum value of these translations and rotations did not exceed 0.25 Å and 15°, respectively, and the acceptance or rejection of these steps was evaluated based on the standard Metropolis criterion [22]. Insertion and deletion of the guest NH_3 molecules was performed with the remaining 25%-25% probabilities, using the cavity biased technique of Mezei [41, 278]. According to this method, the guest molecule insertions were only attempted into empty cavities having a minimum radius of 2.5 Å. Cavities were identified along a $100 \times 100 \times 100$ grid in the basic simulation box, which was regenerated after every 106 Monte Carlo steps. The Monte Carlo acceptance rule was modified accordingly, in order to eliminate the bias introduced this way. The systems were equilibrated by performing 5×10^8 Monte Carlo steps. For each system, the equilibration phase was followed by the production phase during which a total of 5000 configurations with a sampling interval of 10^5 steps between samples were collected for further analyses.

9.2 Results and Discussion

9.2.1 Occupancy Isotherms

The occupancy isotherms calculated for rigid and flexible clathrate structures can be seen in figure 9.1, while equilibrium snapshots from the simulations are shown in figure 9.2.

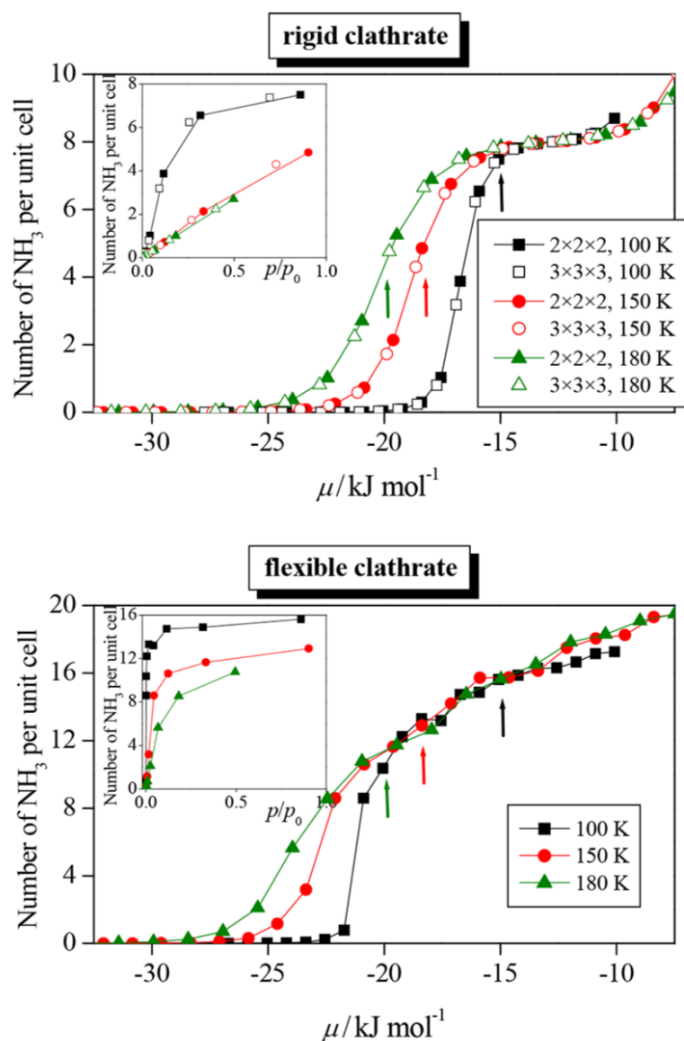


Figure 9.1. Occupancy isotherm of NH₃ in a rigid (top panel) and flexible (bottom panel) clathrate hydrate, as obtained from our GCMC simulations. The insets show the occupancy isotherms calculated as a function of the relative pressure $P_{\text{rel}} = P/P_0$. The arrows indicate the chemical potential values corresponding to the point of condensation of NH₃.

First, it has to be mentioned that in the temperature range investigated here the temperature has very little influence on the behavior of the ammonia occupancy isotherm. Indeed, irrespective of the temperature, the occupancy isotherm is characterized first by

a continuous exponential increase at low chemical potential values, corresponding to the progressive filling of the clathrate cages by the ammonia molecules. Then, above around -16 kJ/mol, the isotherm for the rigid clathrate (figure 9.2, top panel) reaches a rather long plateau covering a roughly 6-8 kJ/mol wide range of chemical potentials. For this range of chemical potentials, the clathrate appears saturated and changes in the chemical potential values result only in a rather small increase of the number of enclathrated molecules. In the corresponding system, 8 ammonia molecules are trapped per unit cell of the simulation box – on average, one ammonia molecule per cage in the clathrate. Finally, at a value of about -9 kJ/mol, the isotherm increases again, corresponding to the possible trapping of additional ammonia molecules in the clathrate cages at very large chemical potential values. Moreover, the comparison between the isotherms calculated for the rigid clathrate by considering $2 \times 2 \times 2$ and $3 \times 3 \times 3$ simulation boxes (figure 9.1, top panel) suggests that the effect of the box size on the results is negligibly weak, since the corresponding occupancy isotherms are almost perfectly superimposed. This indicates that simulations performed by considering the small, $2 \times 2 \times 2$ simulation box can provide results of reasonable quality concerning the cage occupancy calculations at a significantly lower computational cost than when considering the larger, $3 \times 3 \times 3$ box.

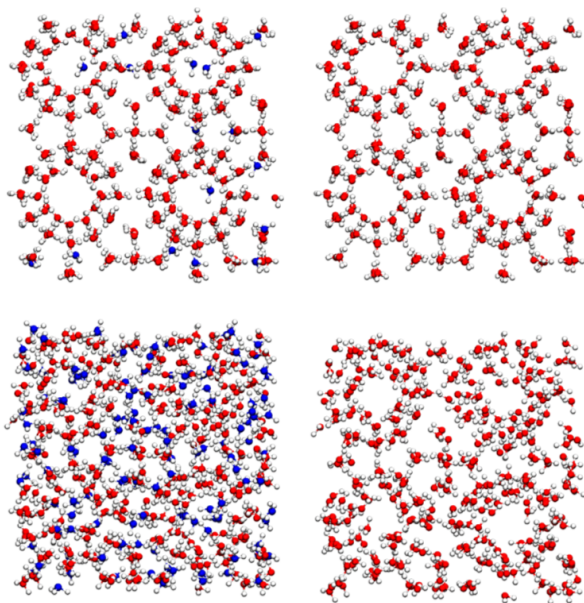


Figure 9.2. Some snapshots of the systems in a flexible clathrate hydrate of NH_3 , as obtained from our GCMC simulations at 100 K at low (-21.72 kJ/mol, top row) and high (-10.08 kJ/mol, bottom row) chemical potential values corresponding to different fillings of the cages. Snapshots for the same chemical potential values are given on the right-hand side of the figure, in which ammonia molecules have been removed for clarity.

The comparison between the ammonia occupancy isotherms simulated for flexible

clathrate structures at 100, 150, and 180 K (figure 9.1, bottom panel) and those given in figure 9.1, top panel for rigid clathrates immediately shows the influence of the cage flexibility on the trapping of the ammonia molecules inside the clathrate. Indeed, not only the chemical potential value at which the filling of the clathrate cages starts is lower for flexible than for rigid structures, but also the global shape of the isotherm looks different. Indeed, the isotherm for flexible clathrate is characterized by an almost continuous rise with increasing chemical potential, and no plateau is evidenced contrarily to the rigid clathrate situation. Overall, for any given chemical potential and temperature value, the occupancy of the flexible clathrate is higher than that of the rigid one. More surprisingly, the number of ammonia molecules that can be inserted in the simulation box rapidly exceeds the number of cages upon the increase of the chemical potential, which rises a question about the stability of the clathrate in such conditions and, as a consequence, about the exact nature of the corresponding system.

Another way to represent the obtained occupancy isotherms is to convert the chemical potential to relative pressure $P_{\text{rel}} = P/P_0$, which is the pressure of the system, P , normalized by that of the saturated vapor, P_0 . Since the bulk vapor phase of the system is practically empty in every case, the value of the absolute pressure, P , can hardly be evaluated in the simulations. However, the relative pressure can simply be calculated as [279]

$$P_{\text{rel}} = \frac{P}{P_0} = \frac{\exp \mu/k_b T}{\exp \mu_0/k_b T} \quad (9.1)$$

where k_b stands for the Boltzmann constant and μ_0 is the chemical potential value corresponding to the point of condensation. To determine this μ_0 value, we performed a new set of GCMC simulations by considering only the NH_3 molecules in a box containing no water molecule and having the same volume as the box used for the clathrate simulation. In this case, there is no absorption/incorporation (as there is no clathrate), but only condensation of ammonia at a certain point, corresponding to the chemical potential value μ_0 . The occupancy isotherms as a function of P_{rel} are shown in the inset of figure 9.1. Note that the P_0 value has been determined here only as a reference value for converting chemical potentials to relative pressures. Moreover, because equation 9.1 is only valid up to the point of condensation, the conversion from μ to P_{rel} has not been done above the value $P/P_0 = 1$.

Note that the value of P_0 could, in principle, be obtained from the Antoine's equation

$$\log P_0 = A - \frac{B}{T + C} \quad (9.2)$$

where the temperature is in K and the pressure in bar. To the best of our knowledge,

Antoine's coefficients for ammonia are unfortunately not known below 164 K. However, in the 164-240 K range, their values are $A = 3.18757$, $B = 506.713$ K, and $C = -80.78$ K, which gives $P_0 = 0.012$ bar at 180 K. By contrast, P_0 values at 100 and 150 K cannot be calculated, which prevents any reasonable comparison with actual physical conditions for these very low temperatures.

9.2.2 Structural Characterization

To investigate the structure of the ammonia + water system when the ammonia content increases, we have characterized the geometrical order of the water molecules in the simulation box by calculating an order parameter that measures the degree to which the nearest-neighbor water molecules are tetrahedrally coordinating a reference water molecule [280]. The tetrahedral order parameter that has been shown to correctly describe the ordering of the water molecules in clathrates has been defined as

$$\langle \zeta^{ww} \rangle = \frac{1}{N_w} \sum_{N_w} \left[1 - \frac{3}{8} \sum_{i=1}^3 \sum_{j=i+1}^4 (\cos \psi_{ij} + 1/3)^2 \right] \quad (9.3)$$

where the indices i and j run over the four nearest water neighbors of a given water molecule, ψ_{ij} is the angle between the bonds that this given molecule forms with its nearest-neighbors i and j , and N_w is the total number of water molecules. For a perfectly ordered clathrate, $\zeta_{ww} = 1$, whereas this value decreases to 0.63 in liquid water [280].

The values of $\langle \zeta^{ww} \rangle$ calculated at 100, 150, and 180 K in the range of chemical potential considered are given in figure 9.3, together with the occupancy isotherms for the flexible clathrates.

These curves clearly indicate that the values of $\langle \zeta^{ww} \rangle$ are equal to or slightly smaller than one up to a threshold value of the chemical potential, above which they continuously decrease. More interestingly, this threshold value, which is obtained at the beginning of the rising part of the isotherm, corresponds to around eight ammonia molecules per unit cell at 100 and 150 K, and to a number of NH_3 between about five and eight molecules per unit cell at 180 K. This corresponds approximately to a complete filling of the clathrate structure at the two lowest temperatures considered here, and, more probably, to a partial filling of the clathrate at 180 K. Then, above this threshold value, the decrease of $\langle \zeta^{ww} \rangle$ could be interpreted as resulting from an increasing disordering of the water network when the number of enclathrated NH_3 molecules increases. However, the value $\langle \zeta^{ww} \rangle = 0.6$, corresponding to a complete breakdown of the clathrate structure, such as in liquid water, is only reached at 180 K and very high NH_3 loading, which raises questions on the physical state of the systems corresponding to intermediate values of $\langle \zeta^{ww} \rangle$ between 1 (perfectly

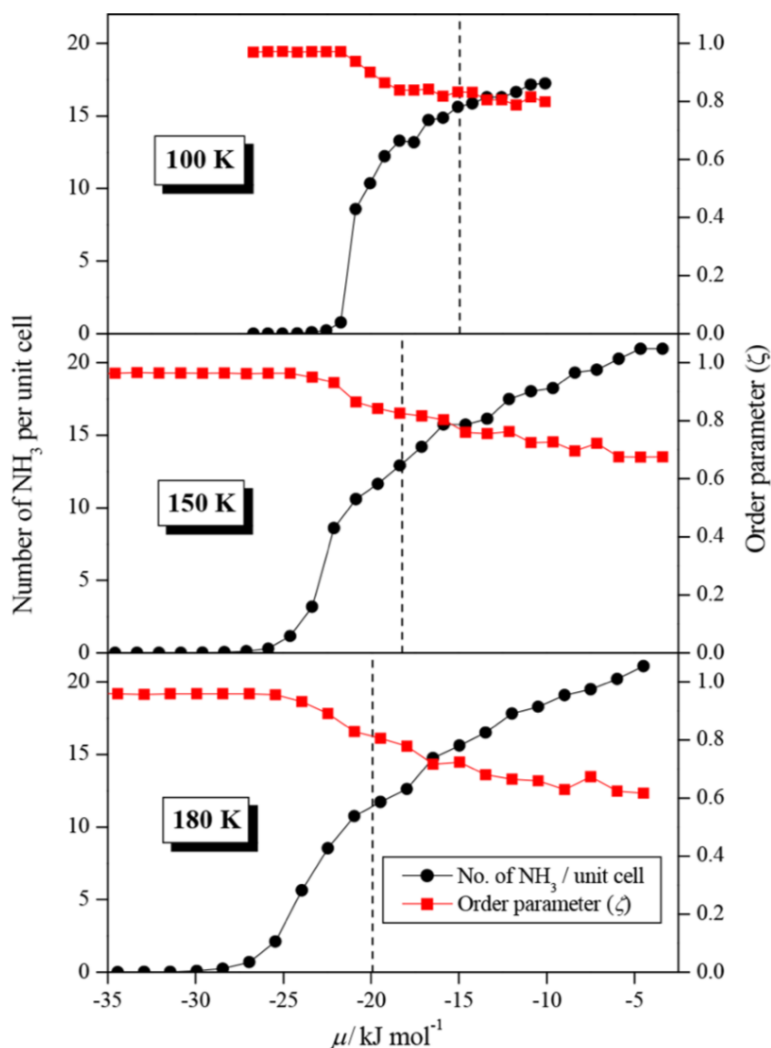


Figure 9.3. Tetrahedral order parameter calculated for the flexible NH_3 clathrates, as a function of the chemical potential. The corresponding occupancy isotherms are also shown. The dashed vertical lines indicate the chemical potential values corresponding to the point of condensation of NH_3 . Scales at the left and right side of the figure correspond to the occupancy isotherm and order parameter data, respectively.

tetrahedrally ordered water molecules) and 0.6 (liquid-like disordered water molecules).

A more detailed analysis of the water arrangements can, in fact, be deduced from the distribution of the ζ^{ww} parameter values, $P(\zeta^{\text{ww}})$, than simply from its average value. Let us first comment the situation corresponding to the results obtained at 100 K. In this case, the $P(\zeta^{\text{ww}})$ distribution is given in figure 9.4 for selected values of the chemical potential, ($\mu = -21.72, -20.88, -19.22, -16.73, -13.40,$ and -10.08 kJ/mol) corresponding to different NH_3 loadings (0.8, 8.6, 12.2, 14.7, 16.3, and 17.2 NH_3 molecules per unit cell in average,

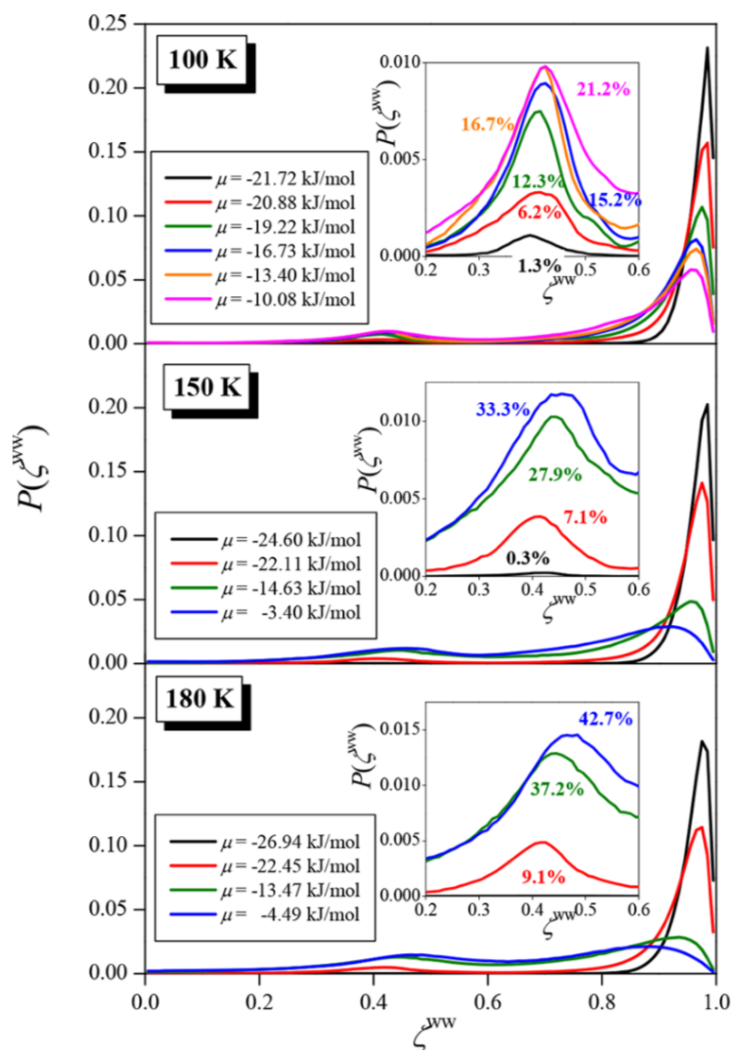


Figure 9.4. Distributions of the tetrahedral order parameter, obtained by considering only the O atoms, for various chemical potential values, corresponding to different NH_3 loadings in the flexible clathrate. The insets show the region of the peak around 0.4 on a magnified scale. The percentage of atoms giving rise to this peak is also indicated.

respectively). At low chemical potential values, the calculated distribution clearly exhibits one single peak, located at 0.997, indicating that in this case all the water molecules are involved in a tetrahedral arrangement with their water neighbors. In contrast, when increasing the chemical potential value, a small shift of ζ^{ww} to lower values is observed and, more importantly, a second peak is evidenced at around $\zeta^{ww} = 0.4$ in the distribution, the intensity of which is increasing with the ammonia loading. The presence of this second peak indicates that an increasing fraction of water molecules lose their tetrahedral coordination when the number of ammonia molecules increases. However, the integration of this

peak of the $P(\zeta^{\text{ww}})$ distribution shows that about 80% of the water molecules remain more or less involved in a tetrahedral arrangement with the surrounding water molecules even at the highest chemical potential values considered here. This conclusion clearly indicates that the average value of $\langle \zeta^{\text{ww}} \rangle = 0.8$, calculated at 100 K at high chemical potentials (figure 9.3, top panel) does not correspond to a fully disordered system, but rather to a tetrahedrally ordered system, containing nontetrahedrally coordinated, possibly off-network water molecules up to 20%. This conclusion suggests the persistence of the clathrate structure in the simulation box during the entire course of our simulations, even at very high ammonia loading, as evidenced on the simulation snapshots (figure 9.2).

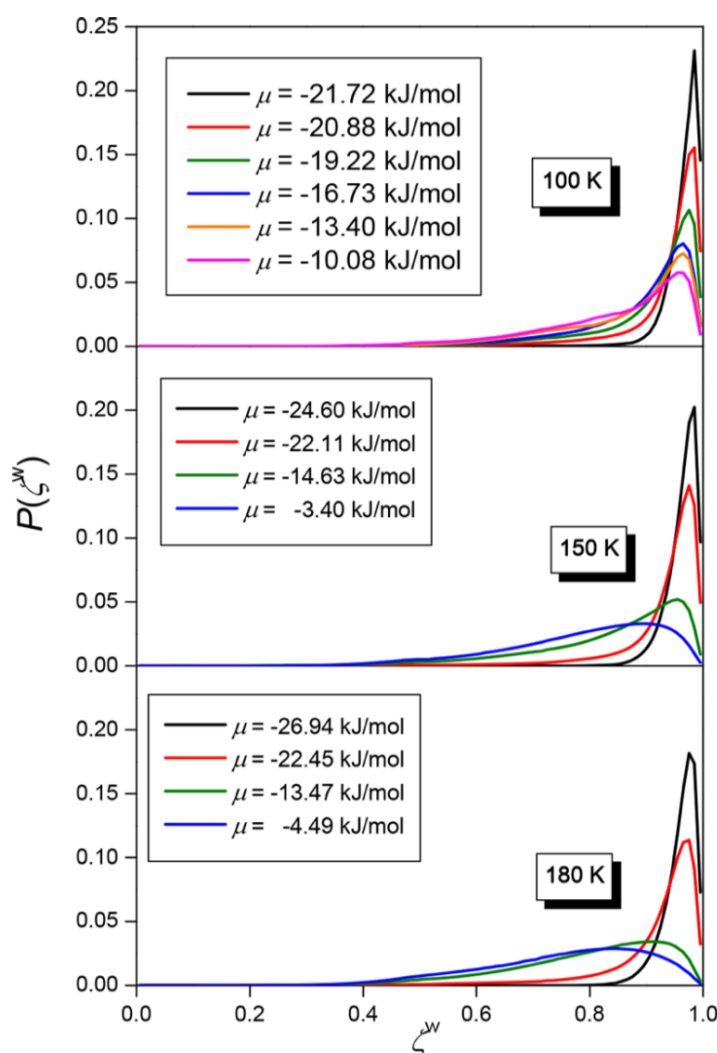


Figure 9.5. Distribution of the tetrahedral order parameter, obtained by considering both the O and N atoms, for various chemical potential values, corresponding to different NH_3 loadings in the flexible clathrate.

To complement our investigations, we have also calculated the tetrahedral order parameter without discriminating between water or ammonia neighbors of the reference water molecule. The corresponding distributions of this parameter are given in figure 9.5 (top panel) at different chemical potential values. To distinguish it from the ζ^{ww} order parameter, measuring the tetrahedrality of solely the water neighbors, this parameter is denoted here as ζ^w . Contrarily to $P(\zeta^{ww})$, the $P(\zeta^w)$ distributions are characterized by only a single peak, the maximum of which is always located above 0.9. Although this peak exhibits an increasing shoulder at lower values when the chemical potential value rises, the persistence of the main peak around 0.95 shows that most of the water molecules stay tetrahedrally coordinated by their neighbors in the entire chemical potential range investigated. This is a strong indication that some ammonia molecules can replace water molecules, and become incorporated in the water lattice, as already observed in previous molecular dynamics simulations of the ammonia clathrate [260].

Because the tetrahedral coordination cannot unambiguously discriminate between ice-like and clathrate-like configurations, an additional criterion characterizing the obtained structure is needed. Such a criterion is based on the fact that water molecules in clathrates form five-membered rings (cyclic pentamers) in clathrates, while no such cyclic pentamers exist in I_h ice [281]. A water molecule is thus considered being involved in a cyclic pentamer if a structure is found in which (i) five oxygen atoms of the water molecules form the vertices of such a ring, and (ii) the length of all the five edges of this ring structure is shorter than the position of the first minimum in the oxygen-oxygen radial distribution function in the system [281]. According to this criterion, water molecules in I_h ice do not form any five-member rings, while in clathrate structures all water molecules participate in 4, 5, or 6 such rings. Note also that liquid water shows a broad distribution of cyclic pentamers [281].

The calculated fraction of water molecules that are part of a given number of pentameric rings at 100 K is shown in figure 9.6 for selected values of the chemical potential, corresponding to different NH_3 loadings along the occupancy isotherm.

For reference, result for a rigid clathrate is also shown in the figure figure 9.6, which confirms that water molecules in a perfectly ordered clathrate structure are involved in four, five, or six pentamers. In contrast, when considering flexible clathrates, an increasing fraction of water molecules belonging to less than four cyclic pentamers is calculated with increasing ammonia chemical potential (and, hence, with increasing ammonia loading), which is a strong indication for a progressive loss of connections between adjacent cages. Nevertheless, even at the highest ammonia loading, a significant number of water molecules still take part in four, five, or six pentameric rings, indicating that the clathrate structure is partially preserved in the system.

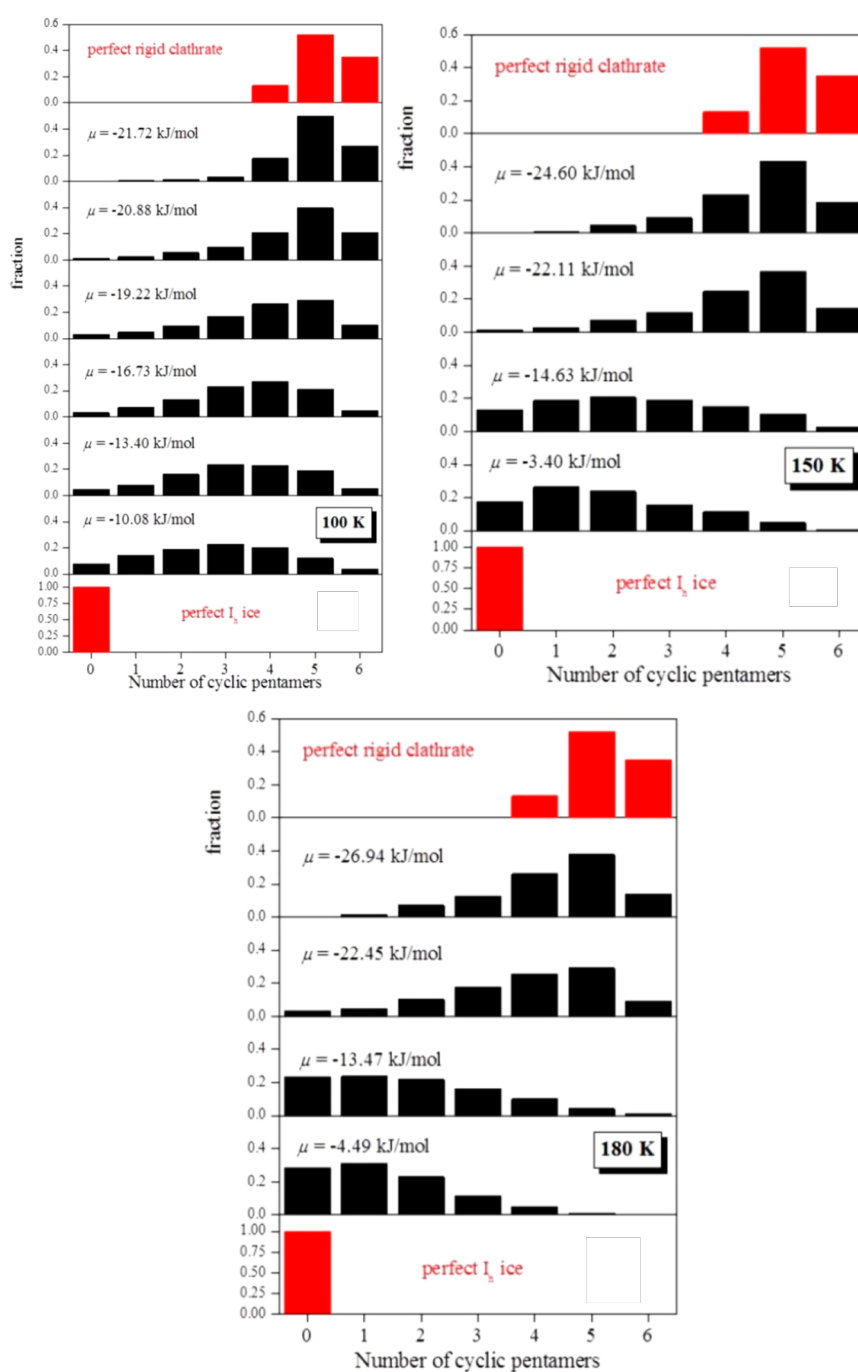


Figure 9.6. Fraction of water molecules that belong to a given number of cyclic pentamers in the simulated systems. The distributions corresponding to the perfect rigid clathrate and to the perfect I_h ice crystal are given as a reference in the top and bottom panels, respectively.

Another way to characterize the structural arrangement of the molecules in the systems investigated is the calculation of certain partial radial distribution functions (RDFs). Figure 9.7 shows the simulated RDFs between the oxygen atoms of the water cages ($g_{OO}(r)$), between these oxygen atoms and the nitrogen atoms of the ammonia molecules ($g_{NO}(r)$), and between nitrogen atoms of the ammonia molecules ($g_{NN}(r)$) for different values of the chemical potential, corresponding to various ammonia loadings in the flexible clathrate at 100 K. For comparison, results obtained at full loading of the rigid clathrate are also shown. First, the $g_{OO}(r)$ in figure 9.7 shows that, at the low chemical potential values corresponding to the first part of the occupancy isotherm, the structural arrangement of the water molecules is similar in the rigid and flexible clathrates. This is a clear indication of the preservation of the clathrate structure at low ammonia loading. However, as the chemical potential value increases, the long-range ordering of the oxygen atoms gets progressively lost. Meanwhile, the first peak of the N-N RDFs shows that nearest neighbor ammonia molecules are separated by about 6.5 Å at low NH₃ loading, corresponding to the very first part of the occupancy isotherm, similarly to that in the rigid clathrate. This distance corresponds to that of the neighboring cages. However, as the number of the trapped NH₃ molecules increases, an additional peak of $g_{NN}(r)$ is evidenced around 3 Å, as seen in figure 9.6, indicating that NH₃ pairs might have been formed in the system. This feature could correspond to near-neighbor ammonia molecules in a more and more disordered structure. Finally, the analysis of the $g_{NO}(r)$ functions also confirms that the flexible clathrate behaves similarly to the rigid one at low chemical potential values, whereas significant differences are evidenced when the number of the ammonia molecules increases. In particular, the first peak of $g_{NO}(r)$ around 4 Å not only broadens and shifts to smaller distances when the chemical potential value increases, but it also exhibits a weak shoulder around 2.8 Å. These features are clear indications of the formation of some NH₃-H₂O pairs in the system, and can be related to the conclusions obtained above from the calculations of the ζ^w parameter, namely, that some of the ammonia molecules can displace water, and become incorporated in the water lattice, contributing to the increase of the number of ammonia molecules trapped in the simulated system with increasing the chemical potential values.

Similar analyses have been performed at the two higher temperatures (150 and 180 K) to characterize the structural evolution of the ammonia clathrate upon temperature increase. According to the shape of the occupancy isotherm simulated at $T = 150$ K, four characteristic systems have been analyzed in detail. These systems correspond to the chemical potential values of $\mu = -24.6, -22.11, -14.63,$ and -3.40 kJ/mol, and to 1.1, 8.6, 15.7, and 20.6 NH₃ molecules per unit cell, respectively. The corresponding distributions of the tetrahedral order parameter for the relative arrangement of the neighboring water

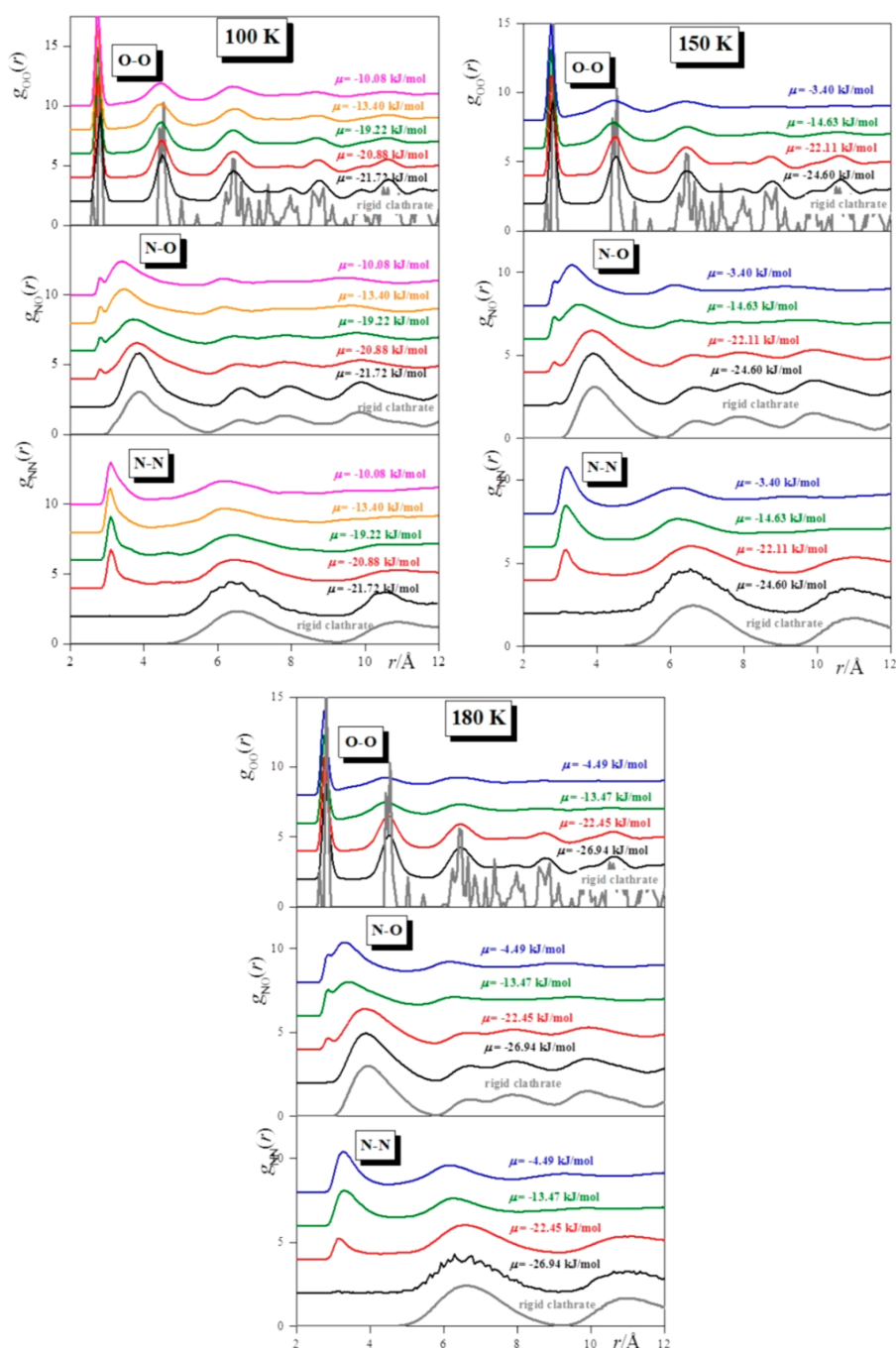


Figure 9.7. Partial radial distribution functions between the O atoms of the water cages (top panels), between the O and N atoms (middle panels), and between the N atoms (bottom panels). The radial distribution functions calculated for the rigid clathrate at full occupancy is also given as a reference. The curves corresponding to increasing chemical values are shifted up by 2, 4, 6, 8, and 10 units, for clarity.

molecules, $P(\zeta^w)$, the distribution of the tetrahedral order parameter without discriminating between water or ammonia neighbors of the reference water molecule, $P(\zeta^w)$, and the fraction of water molecules that form part of a given number of pentameric rings are shown in figure 9.4, figure 9.5, and figure 9.6, respectively. As is evidenced in these figures, the clathrate structure appears to be almost perfectly preserved up to a loading corresponding to about eight ammonia molecules per unit cell, with a loss of the tetrahedral coordination for about 7% of the water molecules, corresponding to an increasing fraction of water molecules that are involved in less than four cyclic pentamers. The higher ammonia loadings are characterized by an increasing disorder, and the complete disappearance of water molecules involved in six pentameric rings is a strong indication for the disruption of the clathrate structure at 150 K. This is also confirmed by the disappearance of the peak around 0.9 in $P(\zeta^w)$, which illustrates the loss of any tetrahedral coordination for the water molecules as the number of ammonia molecules increases in the simulation box. Meanwhile, the increasing number of water molecules that are not included in any cyclic pentamer (as evidenced by the growing intensity of the peak at 0 in figure 9.7) suggests the formation of ice in the system as the clathrate structure disappears. These conclusions are also supported by the analysis of the $g(r)$ curves given on figure 9.7. Indeed, the $g_{OO}(r)$ functions show that while the clathrate structure is almost preserved at $\mu = -24.6$ and -22.11 kJ/mol, it clearly disappears at higher chemical potential values, at which $g_{OO}(r)$ appears to be similar to the corresponding distribution calculated for low density amorphous (LDA) ice [282, 283]. In addition, the appearance of a short distance peak of $g_{NN}(r)$ at 3.2 \AA as well as of that of $g_{NO}(r)$ around 2.8 \AA indicate the formation of ammonia-ammonia and ammonia-water pairs in the system.

9.3 Conclusions

In this chapter, we have investigated the trapping of ammonia molecules into a clathrate structure by means of Grand Canonical Monte Carlo simulations, at three different temperatures relevant for astrophysical environments. Contrarily to previous molecular dynamics simulation studies performed on the same system [259, 260], no a priori assumption was made on the number of ammonia molecules incorporated into the water lattice, it was a function of the chemical potential. This treatment allowed us to investigate the stability of the clathrate structure as a function of not only the temperature, but also of the ammonia loading.

The results have revealed that ammonia containing clathrate of structure I is stable at partial filling during the whole length of our GCMC simulations, irrespective of the temperature in the range investigated here. It could also be stable – more exactly, metastable during the entire course of our simulations – in a chemical potential range that

corresponds to the full occupancy of the clathrate structure. At higher chemical potential values and higher temperatures, new features are evidenced by the various structural analyses performed, which can be related to a progressive dissolution of the clathrate concomitant with a transformation to an ice phase showing structural ordering similar to low density amorphous ice at 150 and 180 K. This dissolution of the clathrate allows a continuously increasing loading of ammonia molecules that are thus mixed with water molecules in the new phase formed. It should be mentioned that the full characterization of the ice phase form upon clathrate dissolution would require additional investigations that are beyond the scope of this work, since discriminating between the various phases of solid ice could be a very tedious task [284]. In addition, the present results may depend on the water potential model used here (TIP4P/Ice), for which no detailed characterization of the various amorphous ice phases is available in the literature, contrarily to a number of water models, including polarizable ones [285], which have been shown to exhibit stability of LDA ice up to at least 180 K, depending also on the pressure and the way of preparation [286–288]. Moreover, as for any GCMC simulations, the results obtained could depend on the number of MC steps used in the calculations. Despite the length of the simulations performed here, it could be possible that the total decomposition of the clathrate hydrate phase upon increasing ammonia loading has not been fully reached during the course of our simulations. In that sense, the picture described here in which part of the system remains clathrate-like at 150 and 180 K even at high ammonia loading could be questioned in much longer GCMC simulations.

The present GCMC results support the stability (or metastability) of the ammonia clathrate of structure I at very low temperature (100 K) and for chemical potential (or pressure) values that do not exceed the single-occupancy of all the clathrate cages, in accordance with the conclusions obtained from previous MD simulations [259, 260].

However, we cannot definitely rule out the possibility that our system has been stuck in a local free energy minimum during the entire course of our simulations (as it could also be the case in MD simulations). Note that such metastable states have been recently experimentally observed, for instance, for the N_2 clathrate [289], and, even, for empty clathrates [290], suggesting that kinetic effects may play an important role in the evolution of the clathrates structures [289].

In the systems simulated in the present work, ammonia molecules are trapped into the cages of the water lattice with the formation of hydrogen-bonds between water and ammonia molecules, in which the water molecule can act as both proton-acceptor and proton-donor. Ammonia molecules can also displace water molecules, and become incorporated into the water lattice upon increasing the ammonia loading and the temperature.

The incorporation of some ammonia molecules into the water lattice results in the destabilization of the clathrate structure and, as the number of ammonia molecules increases, more and more ammonia-ammonia and ammonia-water pairs are formed that finally lead to the disappearance of the clathrate structure.

The results of the present work emphasize the role that ammonia can play in forming or destabilizing solid clathrate phases at low temperatures in planetary environments [291]. They could thus help in better understanding the mechanisms governing the stability regions of, for instance, the methane clathrate phases on various moons in the Solar System [259]. Indeed, methane clathrates are likely present on Titan, Enceladus, or Europa [292], where they are supposed to consist internal reservoirs of methane and other atmospheric gases. In the case of Titan, the dissociation of these methane clathrates has even been invoked to be the main contributor to the replenishment of Titan's atmospheric methane via outgassing episodes [292–294].

Our calculations also indicate a subtle interplay between the various environmental conditions on the stability of the ammonia clathrate phase. Ammonia clathrate may thus be ubiquitous in the interiors of the icy bodies of the outer solar system. Indeed, the surface temperature of Jupiter's icy moon Europa, which can reach about 130 K [295], suggests that ammonia clathrate may be present in the ice crust and favor biochemical processes. The subsurfaces of other icy bodies of the solar system located at further distances may also harbor ammonia clathrates, provided that some internal heat sources allow the local temperature to remain in the 100-150 K range.

Summary

The ultimate aim of studying interfaces is to determine the relations between the thermodynamic properties and the microscopic structure of the system under study. One possible framework is provided by the Capillary Wave Theory. Under its assumptions, the fluctuations along the surface normal and the tangential directions can be decoupled. The two resulting terms are the intrinsic surface and the intrinsic density profile. The ordinary density profile can be easily recovered by the convolution of the intrinsic profile and a Gaussian function representing the fluctuations of the intrinsic surface. In computer simulations, this intrinsic analysis enables us to selectively probe the molecules that are at the interface of the various phases, providing detailed information on their structure and dynamics.

In my thesis, we have developed a python software package PYTIM that provides a convenient way to perform such analyses. Most of the popular surface analysis methods are incorporated in the package, such as ITIM, GITIM and the method of Willard and Chandler. The freely available package can be readily extended by custom-made analysis tools.

Having all the necessary tools at hand, we have investigated the dynamical behavior of various molecules at their liquid-vapor interfaces. The molecules used in this study, namely water, acetone, acetonitrile, methanol and carbon-tetrachloride, range from apolar through aprotic dipolar to hydrogen bonding one. The obtained results indicate a 2-4-fold increase in mobility at the interface. This suggests a picture of a much more fluid surface layer, sharing some traits with those of rarefied fluids in the case of non-hydrogen-bonding liquids, which can have important consequences for diffusion-limited reactions occurring at the surface of liquid phases.

Another aspect of my work concerned the calculation of pressure profiles, in order to investigate the interfacial properties of various systems. These calculations are complicated by the fact that they require the local determination of a non-local quantity. Using the Harasima path, a certain amount of the total lateral pressure is associated with each particle, making the calculation of the lateral pressure profile straightforward and

computationally efficient. A serious technical problem in calculating pressure profiles in charged systems is how to take into account the long range correction term of the electrostatic interaction. This can be overcome using mesh Ewald methods. Therefore, we have derived the local pressure from the reciprocal space contribution of mesh Ewald methods. We implemented the approach in the GROMACS molecular simulation package and have tested it on a model of water/vapor interface. The method is highly efficient, as it displays the same $N \log(N)$ scaling as the sPME algorithm used to compute long-range correction to forces and energy.

In the course of extensive testing for the calculation of the surface tension of the SPC/E water model, we found that the difference between the surface tension calculated with and without the assumption of isotropic kinetic energy tensor amounts to about 15% at ambient temperature. Substituting the constraints with harmonic springs completely removes the asymmetry, and recovers the equality of the two methods. The ideal gas contribution originates solely from the rotational degrees of freedom of the molecules, as the translational ones were found to behave isotropically. The coupling of the kinetic degrees of freedom to the positional ones can be exploited to derive an expression for the ideal gas surface tension profile as a function of molecular orientations. This shows that the equipartition is not violated, only one has to take into account the correlations between kinetic and positional degrees of freedom, which are introduced by the presence of the rigid constraints.

With the established methods of intrinsic analysis and pressure profile calculation, we studied the distribution of surface tension along the surface normal. The obtained results show an insensitivity of the distribution of surface tension to the type of intermolecular interactions acting in the liquid phase: in every case, at least 85% of the surface tension comes from the first molecular layer, while, with the exception of methanol, the second layer contributes roughly 10% to the surface tension, and the contributions of the subsequent molecular layers are negligible. The intrinsic analysis of the contribution of the subsequent molecular layers to the profile also reveals that practically no surface tension contribution comes from the third and subsequent molecular layers. By contrast, in a non-intrinsic treatment this information is obscured by the effect of neglecting the capillary waves in the analysis.

The two methods can also be applied to investigate a conjecture concerning the spinodal of molecular systems. It was hypothesized that the pressure of the liquid spinodal at a given temperature is closely related to the minimum value of the lateral pressure profile across the liquid-vapor interface at the same temperature. The two pressures are only found to be proportional with each other, their ratio being system dependent. This proves a weaker version of the hypothesis. The results also provide a way to estimate the

spinodal pressure of water both for practical applications and for tuning the parameters in equations-of-state.

A final example of the utility of the pressure profiles concerns the lateral pressure profiles in phospholipid membranes. In this work, we investigated Cantor's hypothesis relating the pressure profiles to the onset of anesthetic action. The presence of anesthetics is found not to alter the lateral pressure in the middle of the membrane, but to decrease it in the region of the ester groups of the lipid tails, close to the outer preferred position of the anesthetic molecules. Given that indeed this change of the lateral pressure profile lays behind the molecular mechanism of anesthesia, the conformational changes of the relevant membrane bound protein molecules are also expected to occur in this region of the ester groups of the membrane.

Last, but not least, if one wants to simulate a complicated two-phase system, it is not always the correct approach to model an explicit interface. For this, we have investigated the trapping of ammonia molecules into a clathrate structure by means of Grand Canonical Monte Carlo simulations, at three different temperatures relevant for astrophysical environments. It has already been experimentally shown that the hydrophilic behavior of ammonia does not disqualify this properly sized molecule from being incorporated into clathrates, together with a more hydrophobic guest that is known to easily form stable clathrates. The results of this work emphasize the role that ammonia can play in forming or destabilizing solid clathrate phases at low temperatures in planetary environments. They could thus help in better understanding the mechanisms governing the stability regions of, for instance, the methane clathrate phases on various moons in the Solar System.

In a broader context, the results obtained here are of relevance in the field of atmospheric chemistry. Although this branch science is often regarded as experimental, theoretical and computational approaches can greatly complement and support its techniques. Such as the case here, where the microscopic point of view provides an atomistic scale insight, one that is completely inaccessible by current experimental methods. The developed methods and the interfaces investigated in this thesis are directly applicable in atmospheric studies, such as the interfacial properties of aerosols and the adsorption of particles on various airborne particles.

THESIS POINTS

1. I developed the PYTIM software package, which provides a consistent framework for programs related to interfacial analysis. The open-source code can serve as a platform for further developments in the field. [S10]
2. I showed that the interfacial molecules can “feel” the constraints of the intrinsic interface when diffusing in the interfacial layer. The long-residing molecules are not randomly distributed, but for clusters. The molecular interaction have a profound impact on the dynamics of interfacial molecules. [S2,S6]
3. I established that with the calculation of lateral pressure profiles using the Harasima path, it is possible to take into account pressure contribution coming from the long-range correction of the electrostatic interactions. These contributions can be localized on the individual atomic sites. [S3]
4. I showed, that when calculating the surface tension in interfacial systems with rigid constraints, the kinetic contribution cannot be averaged out for simplification, as the rigid constraint introduce a coupling between kinetic and positional degrees of freedom. [S8]
5. I determined, that in molecular liquids, about 90% of the total surface tension originates from the first molecular layer, while around 10% from the second. The subsequent molecular layers have negligible contribution to the surface tension, in agreement with the physical interpretation of the surface tension. [S1,S4]
6. I showed, that there is a proportionality between the spinodal pressure and the minimum of the lateral pressure profile. This material constant is temperature independent. Thus, the knowledge of the lateral pressure profile enables the approximation of the spinodal on broad range of temperature, once it is known at a single point. [S7]
7. I determined, that presuming that indeed the change of the lateral pressure profile lays behind the molecular mechanism of anaesthesia, the conformational changes of the relevant membrane bound protein molecules, predicted by Cantor, are also expected to occur in the region of the ester groups of the membrane. [S5]
8. I demonstrated, that despite their polarity, under suitable thermodynamic conditions, such as those found in astronomical environments, ammonia clathrates can indeed be stable. [S9]

PUBLICATIONS INCLUDED IN THE THESIS

[S1] Layer-by-layer and intrinsic analysis of molecular and thermodynamic properties across soft interfaces, M. Sega, B. Fábián, P. Jedlovsky, *J. Chem. Phys.*, 2015, 143, 114709 (2015 Editors' Choice) - IF: 2.842; IR: 5

[S2] Dynamics of the Water Molecules at the Intrinsic Liquid Surface as Seen from Molecular Dynamics Simulation and ITIM Analysis, B. Fábián, M.V. Sencanski, I.N. Cvijetic, P. Jedlovsky, G. Horvai, *J. Phys. Chem. C*, 2016, 120 (16), 8578-8588 - IF: 4.484; IR: 6

[S3] Pressure Profile Calculation with Mesh Ewald Methods, M. Sega, B. Fábián, P. Jedlovsky, *J. Chem. Theory Comput.*, 2016, 12(9), 4509-4515 IF: 5.399; I: 1

[S4] How the Surface Tension of Various Liquids is Distributed along the Interface Normal?, M. Sega, B. Fábián, G. Horvai, P. Jedlovsky, *J. Phys. Chem. C*, 2016, 120 (48), 27468-27477 - IF: 4.484; IR: 13

[S5] Lateral Pressure Profile and Free Volume Properties in Phospholipid Membranes Containing Anesthetics, B. Fábián, M. Sega, V. Voloshin, N. Medvedev, P. Jedlovsky, *J. Phys. Chem. B*, 2017, 121 (13), 2814-2824 - IF: 3.146; IR: 6

[S6] Single particle Dynamics at the Intrinsic Surface of Various Apolar, Aprotic Dipolar and Hydrogen Bonding Liquids, As Seen from Computer Simulations, B. Fábián, M. Sega, G. Horvai, P. Jedlovsky, *J. Phys. Chem. C*, 2017, 121 (22), 5582-5594 - IF: 3.146; IR: 1

[S7] Relation Between the Liquid Spinodal Pressure and the Lateral Pressure Profile at the Liquid-Vapor Interface, M. Sega, B. Fábián, A. Imre, P. Jedlovsky, *J. Phys. Chem. Lett.*, 2017, 121 (22), 12214-12219 - IF: 4.484; IR: 1

[S8] Non-Zero Ideal Gas Contribution to the Surface Tension of Water, M. Sega, B. Fábián, P. Jedlovsky, *J. Phys. Chem. Lett.*, 2017, 8 (12), 2608-2612 - IF: 8.709; IR: 2

[S9] Ammonia Clathrate Hydrate As Seen from Grand Canonical Monte Carlo Simulations, B. Fábián, S. Picaud, P. Jedlovsky, A. Guilbert-Lepoutre, O. Mousis, *ACS Earth and Space Chemistry*, 2018, 2 (5), 521-531 - IF: -; IR: 0

[S10] Pytim: a python package for the interfacial analysis of molecular simulations, M. Sega, G. Hantal, B. Fábián, P. Jedlovsky, *J. Comp. Chem.*, 2018, (accepted) - IF: 3.221; IR: 0

OTHER PUBLICATIONS

[SN1] Floating Patches of HCN at the Surface of Their Aqueous Solutions – Can They Make “HCN World” Plausible?, B. Fábián, M. Szöri, P. Jedlovszky, *J. Phys. Chem. C*, 2014, 118 (37), pp 21469–21482 - IF: 4.484; IR: 6

[SN2] Effect of anaesthetics on the properties of a lipid membrane in the biologically relevant phase. A computer simulation study, B. Fábián, M. Darvas, S. Picaud, M. Sega, P. Jedlovszky, *Phys. Chem. Chem. Phys.*, 2015, 17, 14750-14760 - IF: 3.906; IR: 10

[SN3] Properties of the Liquid-Vapor Interface of Acetone-Water Mixtures. A Computer Simulation and ITIM Analysis Study, B. Fábián, B. Jójárt, G. Horvai, P. Jedlovszky, *J. Phys. Chem. C*, 2015, 119, 12473-12487 - IF: 4.484; IR: 5

[SN4] Local lateral environment of the molecules at the surface of DMSO-water mixtures, B. Fábián, I. Abdenacer, M. Bogdan, P. Jedlovszky, *J. Phys. Cond. Matt.*, 2016, 28 (40), 404002- 404011 - IF: 2.617; IR: 1

[SN5] Adsorption of Fluorinated Methane Derivatives at the Surface of Ice under Tropospheric Conditions, As Seen from Grand Canonical Monte Carlo Simulations, I. Sumi, B. Fábián, S. Picaud, P. Jedlovszky, *J. Phys. Chem. C*, 2016, 120 (31), 17386-17399 - IF: 4.484; IR: 1

[SN6] Miscibility and Thermodynamics of Mixing of Different Models of Formamide, B. Kiss, B. Fábián, P. Jedlovszky, *J. Phys. Chem. B.*, 2017, 121 (29), 7147-7155 - IF: 3.146; IR: 1

[SN7] Multiscale Modeling of Interfacial Oxidation Mechanism at Air/Organic Interface: Reactions of CH₂=CH-Terminated Self-Assembled Monolayer with OH•, O₃, and HO₂•, K. Korcsok., M. Szöri, B. Fábián, S. Picaud, P. Jedlovszky, B. Viskolcz, *J. Phys. Chem. C*, 2018, 122 (18), 9886 - IF: 4.484; IR: 0

[SN8] Investigation of the Liquid-Vapor Interface of Water-Formamide Mixtures by Computer Simulation and Intrinsic Surface Analysis, B. Kiss, B. Fábián, A. Idrissi, M. Szöri, P. Jedlovszky, *J. Phys. Chem. C*, 2018 (accepted), - IF: 4.484; IR: 0

Résumé (français)

Les outils de simulation numérique permettent désormais l'analyse des interfaces à l'échelle moléculaire, tant du point de vue de leur structure que de leur comportement dynamique. Ainsi, dans mon travail de thèse, j'ai développé le logiciel PYTIM qui comprend les procédures les plus populaires d'analyse interfaciale à l'échelle moléculaire, fournissant une base solide pour les travaux de recherche sur les surfaces et interfaces.

En utilisant ces méthodes, j'ai étudié le comportement dynamique des molécules situées aux interfaces de différents systèmes d'intérêt biologiques et atmosphériques. Ce faisant, j'ai étudié la corrélation entre la dynamique des molécules à la surface et les interactions intermoléculaires correspondantes. De plus, j'ai travaillé sur le calcul des profils de pression dans les systèmes simulés. Dans ce cas, définir localement une quantité macroscopique, la pression, à l'échelle microscopique représente un obstacle considérable. Nous avons cependant montré que les profils de pression peuvent être calculés dans des systèmes comprenant des charges ponctuelles via le contour de Harasima avec la méthode de sommation d'Ewald (PME). Par ailleurs, j'ai montré comment les contraintes rigides souvent utilisées dans les simulations introduisent un couplage entre les degrés de liberté translationnels (positions) et les degrés de liberté de rotation. La conséquence de ce couplage est que le tenseur d'énergie cinétique n'est plus constant même dans des systèmes en équilibre, ce qui peut introduire une différence significative dans le calcul de la tension de surface.

Les méthodes développées au cours de mon travail de thèse ont permis de calculer, pour différents systèmes, la distribution de la tension superficielle près de l'interface, la relation entre la pression spinodale et le minimum du profil de pression latérale. Elles ont également permis de mieux comprendre les liens entre pression et mécanisme d'action des molécules anesthésiques, fournissant ainsi des bases moléculaires à l'hypothèse de Cantor.

Enfin, j'ai étudié également l'équilibre gaz/solide en caractérisant, à l'aide de simulation de Monte Carlo dans l'ensemble grand canonique, le piégeage de molécules d'ammoniac dans un clathrate, sous conditions de pression et de température caractéristiques d'environnements extraterrestres.

Összefoglaló

A számítógépes szimulációk során a határfelületi analízis eszközei lehetővé teszik a felületi molekulák direkt tanulmányozását, dinamikai és szerkezeti viselkedésük elemzését. A doktori munkám során kidolgozott PYTIM programcsomag egységes keretben foglalja az általános felületanalizáló eljárásokat, szilárd alapot nyújtva a határfelületek elemzésével foglalkozó kutatásoknak.

Ezen módszerek segítségével tanulmányoztam a határfelületi molekulák dinamikus viselkedését biológiai és atmoszférikus szempontból releváns rendszerekben. Ennek során azt vizsgáltam, hogyan függ össze a molekulák felületi dinamikája a közöttük működő kölcsönhatásokkal. Munkámban emellett a nyomásprofilok számolásával foglalkoztam felületi rendszerekben. Esetükben technikai nehézséget okoz az, hogy egy eredendően makroszkopikus mennyiséget, a nyomást kívánjuk lokalizálni valamilyen eljárás segítségével. Bemutattam, hogyan számíthatók a nyomásprofilok a Harasima kontúrral ponttöltéseket tartalmazó rendszerekben, mesh Ewald módszerekkel. Emellett a szimulációkban gyakran használt merev megkötések csatolást vezetnek be a pozíciók és a forgási szabadsági fokok között. Emiatt a kinetikus energia tenzor nem lesz állandó egyensúlyi rendszerekben sem. Ez nem mond ellent az ekvipartíció törvényének, viszont jelentős hibát eredményezhet, amennyiben nem veszik figyelembe a felületi feszültség számítása során.

A kidolgozott módszert doktori munkám során különböző határfelületekkel kapcsolatos problémák vizsgálatára alkalmaztam, mint a felületi feszültség-sűrűség eloszlása a határfelület közelében, a spinodális nyomás és a laterális nyomásprofil minimum között feltételezett kapcsolat, vagy az anesztetikumok hatásmechanizmusának Cantor-féle elmélete.

Dolgozatom legvégén gőz/folyadék egyensúlyokat tanulmányoztam. Ennek során nagykanonikus Monte Carlo szimulációkkal vizsgáltam ammónia klatrát-hidrátokat távoli égitesteken jellemző körülmények között, felderítve stabilitásukat.

Résumé (english)

The tools of numerical simulation enable the analysis of interfaces at the molecular scale, both in terms of their structure and their dynamic behavior. Thus, in my thesis work, I developed the PYTIM software that includes the most popular procedures for interfacial analysis at the molecular level, providing a solid foundation for research work on surfaces and interfaces.

Using these methods, I investigated the dynamic behavior of molecules at the interfaces of different biological and atmospheric systems of interest. In doing so, I studied the correlation between the dynamics of molecules on the surface and the corresponding intermolecular interactions. In addition, I worked on the calculation of pressure profiles in simulated systems. In particular, the localization of an inherently non-local quantity, the pressure, represents a considerable technical difficulty. I have shown that the pressure profiles can be calculated in systems containing point charges via the Harasima contour with mesh Ewald methods (PME). Moreover, I showed how the rigid constraints often used in simulations introduce a coupling between the translational degrees of freedom and the rotational degrees of freedom. The consequence of this coupling is that the kinetic energy tensor is no longer constant, even in equilibrium systems, which – if neglected – can introduce significant errors in the calculation of the surface tension.

The methods developed during my thesis work provided means to study various problems, such as the distribution of the surface tension near the interface, the relation between the spinodal pressure and the minimum of the lateral pressure profile. They also enabled the investigation of the possible links between the lateral pressure profiles and the mechanism of action of anesthetic molecules, thus providing a molecular basis for the hypothesis of Cantor.

Finally, I also studied gas/solid equilibrium characterizing, by Monte Carlo simulation in the grand canonical ensemble, the trapping of ammonia molecules in a clathrate under conditions of pressure and temperature representative of extraterrestrial environments.

Bibliography

- [1] M. Allen, D. Tildesley, *Computer Simulation of Liquids*, Clarendon Press, **1989**.
- [2] T. Young, *Philosophical transactions of the Royal Society of London* **1802**, 92, 12–48.
- [3] A. Arons, M. Peppard, *American Journal of Physics* **1965**, 33, 367–374.
- [4] S. Malin, *Nature Loves to Hide: Quantum Physics and Reality, a Western Perspective*, Oxford University Press, **2003**.
- [5] E. Schrödinger, *Annalen der Physik* **1926**, 384, 361–376.
- [6] T. Hey, P. Walters, *The New Quantum Universe*, Cambridge University Press, **2003**.
- [7] L. Hand, J. Finch, *Analytical Mechanics*, Cambridge University Press, **1998**.
- [8] A. Leach, *Molecular Modelling: Principles and Applications*, Prentice Hall, **2001**.
- [9] D. Marx, J. Hutter, *Ab Initio Molecular Dynamics: Basic Theory and Advanced Methods*, Cambridge University Press, **2009**, 333 pp.
- [10] K. Tosio, *Journal of the Physical Society of Japan* **1950**, 5, 435–439.
- [11] W. Kutzelnigg, *Molecular Physics* **1997**, 90, 909–916.
- [12] J. C. Tully, *Faraday Discussions* **1998**, 110, 407–419.
- [13] P. A. M. Dirac, *Proceedings of the Cambridge Philosophical Society* **1930**, 26, 376.
- [14] D. Bohm, *Quantum Theory*, Dover Publications, **1989**.
- [15] L. Landau, E. Lifshitz, *Mechanics*, Elsevier Science, **1982**.
- [16] L. Landau, E. Lifshitz, *Statistical Physics*, Elsevier Science, **2013**.
- [17] J. Gibbs, *Elementary Principles in Statistical Mechanics*, C. Scribner's sons, **1902**.
- [18] L. Boltzmann, *Über die mechanische Bedeutung des zweiten Hauptsatzes der Wärmetheorie: (vorgelegt in der Sitzung am 8. Februar 1866)*, Staatsdruckerei, **1866**.
- [19] P. Atkins, J. de Paula, *Atkins' Physical Chemistry*, OUP Oxford, **2010**.
- [20] D. Frenkel, B. Smit, *Understanding Molecular Simulation: From Algorithms to Applications*, Elsevier Science, **2001**.
- [21] N. Ashcroft, N. Mermin, *Solid State Physics*, Holt, Rinehart and Winston, **1976**.
- [22] N. Metropolis, A. W. Rosenbluth, M. N. Rosenbluth, A. H. Teller, E. Teller, *The journal of chemical physics* **1953**, 21, 1087–1092.
- [23] M. Praprotnik, D. Janežič, *The Journal of chemical physics* **2005**, 122, 174103.
- [24] L. Verlet, *Physical review* **1967**, 159, 98.
- [25] P. P. Ewald, *Annalen der Physik* **1921**, 369, 253–287.

- [26] S. W. de Leeuw, J. W. Perram, E. R. Smith, *Proc. R. Soc. Lond. A* **1980**, 373, 27–56.
- [27] T. Darden, D. York, L. Pedersen, *The Journal of chemical physics* **1993**, 98, 10089–10092.
- [28] U. Essmann, L. Perera, M. L. Berkowitz, T. Darden, H. Lee, L. G. Pedersen, *The Journal of chemical physics* **1995**, 103, 8577–8593.
- [29] R. Hockney, J. Eastwood, *Computer Simulation Using Particles*, McGraw-Hill, **1981**.
- [30] R. Hockney, S. Goel, J. Eastwood, *Journal of Computational Physics* **1974**, 14, 148–158.
- [31] H. Berendsen, W. Van Gunsteren, *Molecular-dynamics simulation of statistical-mechanical systems* **1986**, 43–65.
- [32] S. Nosé, *Molecular Physics* **1984**, 52, 255–268.
- [33] W. G. Hoover, *Phys. Rev. A* **Mar. 1985**, 31, 1695–1697.
- [34] M. Parrinello, A. Rahman, *Journal of Applied physics* **1981**, 52, 7182–7190.
- [35] G. J. Martyna, M. L. Klein, M. Tuckerman, *The Journal of chemical physics* **1992**, 97, 2635–2643.
- [36] I. McDonald, *Molecular Physics* **1972**, 23, 41–58.
- [37] D. Adams, *Molecular Physics* **1974**, 28, 1241–1252.
- [38] D. Adams, *Molecular Physics* **1975**, 29, 307–311.
- [39] H. J. Stroud, E. Richards, P. Limcharoen, N. G. Parsonage, *Journal of the Chemical Society Faraday Transactions 1: Physical Chemistry in Condensed Phases* **1976**, 72, 942–954.
- [40] B. Smit, *The Journal of Physical Chemistry* **1995**, 99, 5597–5603.
- [41] M. Mezei, *Molecular Physics* **1980**, 40, 901–906.
- [42] J. Rowlinson, B. Widom, *Molecular Theory of Capillarity*, Dover Publications, **2002**.
- [43] S. Poisson, *Nouvelle théorie de l'action capillaire*, Bachelier père et fils, **1831**.
- [44] T. Reed, K. Gubbins, *Applied statistical mechanics: thermodynamic and transport properties of fluids*, McGraw-Hill, **1973**.
- [45] F. Buff, R. Lovett, F. Stillinger Jr, *Physical Review Letters* **1965**, 15, 621.
- [46] J. Penfold, *Reports on Progress in Physics* **2001**, 64, 777.
- [47] D. L. Heath, J. K. Percus, *J. Stat. Phys.* **Oct. 1987**, 49, 319–330.
- [48] I. Benjamin, *Physical review letters* **1994**, 73, 2083.
- [49] T.-M. Chang, L. X. Dang, *The Journal of chemical physics* **1996**, 104, 6772–6783.
- [50] S. Paul, A. Chandra, *The Journal of chemical physics* **2005**, 123, 184706.
- [51] L. B. Pártay, G. Hantal, P. Jedlovsky, Á. Vincze, G. Horvai, *J. Comput. Chem.* **2008**, 29, 945–956.
- [52] P. Jedlovsky, M. Předota, I. Nezbeda, *Molecular Physics* **2006**, 104, 2465–2476.
- [53] M. Tarek, D. J. Tobias, *Physical Review Letters* **2002**, 88, 138101.
- [54] C. F. Lopez, S. O. Nielsen, M. L. Klein, P. B. Moore, *The Journal of Physical Chemistry B* **2004**, 108, 6603–6610.

- [55] J. Chowdhary, B. M. Ladanyi, *J. Phys. Chem. B* **2006**, *110*, 15442.
- [56] M. Sega, S. S. Kantorovich, P. Jedlovszky, M. Jorge, *J. Chem. Phys* **2013**, *138*, 44110.
- [57] A. P. Willard, D. Chandler, *J. Phys. Chem. B* **2010**, *114*, 1954–1958.
- [58] L. B. Pártay, G. Horvai, P. Jedlovszky, *J. Phys. Chem. C* **2010**, *114*, 21681.
- [59] M. Sega, G. Hantal, *Phys. Chem. Chem. Phys.* **2017**, *19*, 18968–18974.
- [60] N. Michaud-Agrawal, E. J. Denning, T. B. Woolf, O. Beckstein, *J. Comput. Chem.* **2011**, *32*, 2319–2327.
- [61] M. Jorge, P. Jedlovszky, M. N. D. S. Cordeiro, *J. Phys. Chem. B* **July 2010**, *114*, 11169–11179.
- [62] M. Sega, *Phys. Chem. Chem. Phys.* **2016**, *18*, 23354–23357.
- [63] J. L. Bentley, *Commun. ACM* **Sept. 1975**, *18*, 509–517.
- [64] H. Edelsbrunner, E. P. Mücke, *ACM Transactions on Graphics* **Jan. 1994**, *13*, 43–72.
- [65] B. Delaunay, *Izv. Akad. Nauk SSSR Otdelenie Matematicheskii i Estestvennyka Nauk* **1934**, *7*, 1–2.
- [66] C. B. Barber, D. P. Dobkin, H. Huhdanpaa, *ACM Transactions on Mathematical Software* **Dec. 1996**, *22*, 469–483.
- [67] H. Si, *ACM Trans. Math. Softw.* **Feb. 2015**, *41*, 11:1–11:36.
- [68] M. Rosenblatt et al., *The Annals of Mathematical Statistics* **1956**, *27*, 832–837.
- [69] E. Parzen, *The annals of mathematical statistics* **1962**, *33*, 1065–1076.
- [70] T. Lewiner, H. Lopes, A. W. Vieira, G. Tavares, *Journal of graphics tools* **2003**, *8*, 1–15.
- [71] W. E. Lorensen, H. E. Cline in *ACM siggraph computer graphics, Vol. 21*, ACM, **1987**, pp. 163–169.
- [72] S. van der Walt, J. L. Schönberger, J. Nunez-Iglesias, F. Boulogne, J. D. Warner, N. Yager, E. Gouillart, T. Yu, *PeerJ* **June 2014**, *2*, e453.
- [73] M. Ester, H.-P. Kriegel, J. Sander, X. Xu, et al. in *Kdd, Vol. 96*, **1996**, pp. 226–231.
- [74] A. Idrissi, I. Vyalov, N. Georgi, M. Kiselev, *J. Phys. Chem. B* **2013**, *117*, 12184–12188.
- [75] J. MacQueen et al. in *Proceedings of the fifth Berkeley symposium on mathematical statistics and probability, Vol. 1*, Oakland, CA, USA, **1967**, pp. 281–297.
- [76] S. Lloyd, *IEEE transactions on information theory* **1982**, *28*, 129–137.
- [77] E. Chacón, P. Tarazona, *Phys. Rev. Lett.* **Oct. 2003**, *91*, 166103.
- [78] E. Lindahl, O. Edholm, *Phys. Rev. E: Stat. Phys. Plasmas Fluids Relat. Interdiscip. Top.* **1998**, *57*, 791.
- [79] K. Aman, E. Lindahl, O. Edholm, P. Håkansson, P. O. Westlund, *Biophys. J.* **2003**, *84*, 102.
- [80] P. Liu, E. Harder, B. Berne, *J. Phys. Chem. B* **2004**, *108*, 6595.
- [81] J. B. Bühn, P. A. Bopp, M. J. Hampe, *Fluid Phase Equilib.* **2004**, *224*, 221.
- [82] M. Sega, R. Vallauri, S. Melchionna, *Phys. Rev. E* **2005**, *72*, 041201.

- [83] S. Y. Bhide, M. L. Berkowitz, *J. Chem. Phys.* **2005**, *123*, 224702.
- [84] I. Benjamin, *Reactivity and Dynamics at Liquid Interfaces*, Vol. 28, Wiley: Chichester, UK, **2015**.
- [85] J. Chowdhary, B. M. Ladanyi, *J. Phys. Chem. B* **2008**, *112*, 6259.
- [86] D. Duque, P. Tarazona, E. Chacón, *J. Chem. Phys.* **2008**, *128*, 134704.
- [87] R. Delgado-Buscalioni, E. Chacón, P. Tarazona, *Phys. Rev. Lett.* **2008**, *101*, 106102.
- [88] R. Delgado-Buscalioni, E. Chacón, P. Tarazona, *J. Phys.: Condens. Matter* **2008**, *20*, 494229.
- [89] B. Fábián, M. V. Sencanski, I. N. Cvijetic, P. Jedlovszky, G. Horvai, *J. Phys. Chem. C* **2016**, *120*, 8578.
- [90] A. Geiger, F. H. Stillinger, A. Rahman, *J. Chem. Phys.* **1979**, *70*, 4185.
- [91] H. E. Stanley, J. Teixeira, *J. Chem. Phys.* **1980**, *73*, 3404.
- [92] G. Pálinkás, E. Hawlicka, K. Heinzinger, *J. Phys. Chem.* **1987**, *91*, 4334.
- [93] E. M. Duffy, D. L. Severance, W. L. Jorgensen, *J. Am. Chem. Soc.* **1992**, *114*, 7535.
- [94] J. M. Stubbs, J. J. Potoff, J. I. Siepmann, *J. Phys. Chem. B* **2004**, *108*, 17596.
- [95] H. J. C. Berendsen, J. R. Grigera, T. Straatsma, *J. Phys. Chem.* **1987**, *91*, 6269.
- [96] H. J. Böhm, I. R. McDonald, P. A. Madden, *Mol. Phys.* **1983**, *49*, 347.
- [97] R. Walser, A. E. Mark, W. F. van Gunsteren, M. Lauterbach, G. Wipff, *J. Chem. Phys.* **2000**, *112*, 10450.
- [98] J. P. Ryckaert, G. Ciccotti, H. J. C. Berendsen, *J. Comput. Phys.* **1977**, *23*, 327.
- [99] S. Pronk, S. Páll, R. Schulz, P. Larsson, P. Bjelkmar, R. Apostolov, M. R. Shirts, J. C. Smith, P. M. Kasson, D. van der Spoel, *Bioinformatics* **2013**, *29*, 845.
- [100] M. Jorge, P. Jedlovszky, M. N. D. S. Cordeiro, *J. Phys. Chem. C* **2010**, *114*, 11169.
- [101] M. Darvas, M. Jorge, M. N. D. S. Cordeiro, S. S. Kantorovich, M. Sega, P. Jedlovszky, *J. Phys. Chem. B* **2013**, *117*, 16148.
- [102] N. A. Rideg, M. Darvas, I. Varga, P. Jedlovszky, *Langmuir* **2012**, *28*, 14944.
- [103] G. Hantal, M. Darvas, L. B. Pártay, G. Horvai, P. Jedlovszky, *J. Phys.: Condens. Matter* **2010**, *22*, 284112.
- [104] J. Chowdhary, B. M. Ladanyi, *Phys. Rev. E* **2008**, *77*, 031609.
- [105] P. Jedlovszky, *J. Phys.: Condens. Matter* **2004**, *16*, S5389.
- [106] A. Wakisaka, H. Abdoul-Carime, Y. Yamamoto, Y. Kiyozumi, *J. Chem. Soc. Faraday Trans.* **1998**, *94*, 369.
- [107] S. Dixit, J. Crain, W. C. K. Poon, J. L. Finney, A. K. Soper, *Nature* **2002**, *416*, 829.
- [108] L. Dougan, S. P. Bates, R. Hargreaves, J. P. Fox, J. Crain, J. L. Finney, V. Réat, A. K. Soper, *J. Chem. Phys.* **2004**, *121*, 6456.
- [109] L. B. Pártay, P. Jedlovszky, Á. Vincze, G. Horvai, *J. Phys. Chem. B* **2008**, *112*, 5428.

- [110] A. Okabe, *Spatial tessellations: concepts and applications of Voronoi diagrams*, Wiley, **2000**.
- [111] G. F. Voronoi, *J. Reine Angew. Math.* **1908**, 134, 198.
- [112] N. Medvedev, *SB RAS Russian Novosibirsk* **2000**.
- [113] T. Kiang, *Z. Astrophys.* **1966**, 63, 433.
- [114] E. Pineda, P. Bruna, D. Crespo, *Phys. Rev. E* **2004**, 70, 066119.
- [115] L. Zaninetti, *Phys. Lett. A* **1992**, 165, 143.
- [116] S. Nihonyanagi, T. Ishiyama, T. K. Lee, S. Yamaguchi, M. Bonn, A. Morita, T. Tahara, *J. Am. Chem. Soc.* **2011**, 133, 16875.
- [117] A. Vila Verde, P. G. Bolhuis, R. K. Campen, *J. Phys. Chem. B* **2012**, 116, 9467.
- [118] D. Laage, J. T. Hynes, *Chem. Phys. Lett.* **2006**, 433, 80.
- [119] U. Balucani, J. P. Brodholt, R. Vallauri, *J. Phys.: Condens. Matter* **1996**, 8, 6139.
- [120] J. Gullingsrud, K. Schulten, *Biophys. J.* **2004**, 86, 3496–3509.
- [121] O. S. Ollila, H. J. Risselada, M. Louhivuori, E. Lindahl, I. Vattulainen, S. J. Marrink, *Phys. Rev. Lett.* **2009**, 102, 078101.
- [122] H. W. Hatch, P. G. Debenedetti, *J. Chem. Phys.* **2012**, 137, 035103.
- [123] A. Torres-Sánchez, J. M. Vanegas, M. Arroyo, *Phys. Rev. Lett.* **2015**, 114, 258102.
- [124] R. S. Cantor, *Biochemistry* **1997**, 36, 2339–2344.
- [125] A. Imre, G. Mayer, G. Házi, R. Rozas, T. Kraska, *J. Chem. Phys.* **2008**, 128, 114708.
- [126] R. H. Templer, S. J. Castle, A. Rachael Curran, G. Rumbles, D. R. Klug, *Faraday Discuss.* **1999**, 111, 41–53.
- [127] J. Irving, J. G. Kirkwood, *J. Chem. Phys.* **1950**, 18, 817–829.
- [128] A. Harasima, *Adv. Chem. Phys.* **1958**, 1, 203–237.
- [129] P. Schofield, J. Henderson, *Proc. Royal Soc. London. A* **1982**, 379, 231–246.
- [130] J. Sonne, F. Y. Hansen, G. H. Peters, *J. Chem. Phys.* **2005**, 122, 124903.
- [131] M. Sega, B. Fábíán, P. Jedlovszky, *J. Chem. Phys.* **2015**, 143, 114709.
- [132] L. Onsager, *J. Am. Chem. Soc. USA* **1936**, 58, 1486–1493.
- [133] P. M. Kasson, B. Hess, E. Lindahl, *Chem. Phys. Lipids* **2013**, 169, 106–112.
- [134] S. Ollila, M. T. Hyvönen, I. Vattulainen, *J. Phys. Chem. B* **2007**, 111, 3139–3150.
- [135] J. M. Vanegas, A. Torres-Sánchez, M. Arroyo, *J. Chem. Theory Comput.* **2014**, 10, 691–702.
- [136] A. J. Sodt, R. W. Pastor, *J. Chem. Phys.* **2012**, 137, 234101.
- [137] J. W. Cooley, J. W. Tukey, *Math. Comput.* **1965**, 19, 297–301.
- [138] M. Deserno, C. Holm, *J. Chem. Phys.* **1998**, 109, 7678–7693.
- [139] Alejandro, J, Tildesley, D J, Chapela, G A, *J. Chem. Phys.* **1995**, 102, 4574–4583.
- [140] C. Vega, J. Abascal, I. Nezbeda, *J. Chem. Phys.* **2006**, 125, 034503.

- [141] J. Alejandre, G. A. Chapela, *J. Chem. Phys.* **2010**, *132*, 014701.
- [142] C. Vega, E. de Miguel, *J. Chem. Phys.* **2007**, *126*, 154707.
- [143] F. Chen, P. E. Smith, *J. Chem. Phys.* **2007**, *126*, 221101.
- [144] J. P. Hansen, I. R. McDonald, *Theory of simple liquids*, Second, Academic Press, London, UK.
- [145] P. H. Hünenberger, *J. Chem. Phys.* **2002**, *116*, 6880–6897.
- [146] R. C. Tolman, *Phys. Rev. Apr.* **1918**, *11*, 261–272.
- [147] J. P. Ryckaert, G. Ciccotti, *J. Chem. Phys.* **1983**, *78*, 7368.
- [148] G. Ciccotti, J. P. Ryckaert, *Comput. Phys. Rep.* **1986**, *4*, 346–392.
- [149] M. Sprik, G. Ciccotti, *J. Chem. Phys.* **1998**, *109*, 7737–7744.
- [150] S. Melchionna, *Phys. Rev. E June* **2000**, *61*, 6165–6170.
- [151] P. M. Chaikin, T. C. Lubensky, *Principles of condensed matter physics*, Cambridge Univ Press, Cambridge, **1995**.
- [152] R. B. Shirts, S. R. Burt, A. M. Johnson, *J. Chem. Phys.* **2006**, *125*, 164102.
- [153] D. S. Corti, M. J. Uline, D. W. Siderius, *J. Chem. Phys.* **2008**, *128*, 124301.
- [154] M. P. Eastwood, K. A. Stafford, R. A. Lippert, M. Ø. Jensen, P. Maragakis, C. Predescu, R. O. Dror, D. E. Shaw, *J. Chem. Theory Comput.* **July 2010**, *6*, 2045–2058.
- [155] R. W. Pastor, B. R. Brooks, A. Szabo, *Mol. Phys.* **Dec. 1988**, *65*, 1409–1419.
- [156] E. Hairer, G. Wanner, C. Lubich in *Geom. Numer. Integr.* Springer-Verlag, Berlin/Heidelberg, **2006**, pp. 179–236.
- [157] M. Sega, B. Fábíán, G. Horvai, P. Jedlovszky, *J. Phys. Chem. C* **2016**, *120*, 27468.
- [158] M. Sega, B. Fábíán, P. Jedlovszky, *J. Chem. Theory Comput.* **Aug. 2016**, *12*, 4509–4515.
- [159] G. J. Gloor, G. Jackson, F. J. Blas, E. de Miguel, *J. Chem. Phys.* **2005**, *123*, 134703.
- [160] A. Ghoufi, P. Malfreyt, *J. Chem. Phys.* **2012**, *136*, 024104.
- [161] J. Hermans, H. J. C. Berendsen, W. F. van Gunsteren, J. P. M. Postma, *Biopolymers* **1984**, *23*, 1513–1518.
- [162] W. L. Jorgensen, J. Chandrasekhar, J. D. Madura, R. W. Impey, M. L. Klein, *J. Chem. Phys.* **1983**, *79*, 926.
- [163] J. L. Abascal, C. Vega, *J. Chem. Phys.* **2005**, *123*, 234505.
- [164] M. W. Mahoney, W. L. Jorgensen, *J. Chem. Phys.* **2000**, *112*, 8910–8922.
- [165] S. W. Rick, *J. Chem. Phys.* **2004**, *120*, 6085.
- [166] A. Idrissi, G. Hantal, P. Jedlovszky, *Phys. Chem. Chem. Phys.* **2015**, *17*, 8913.
- [167] H. Stanley, *Introduction to phase transitions and critical phenomena*, Oxford University Press, **1971**.
- [168] R. Speedy, C. Angell, *The Journal of chemical physics* **1976**, *65*, 851–858.
- [169] R. J. Speedy, *The Journal of Physical Chemistry* **1982**, *86*, 982–991.

- [170] P. H. Poole, F. Sciortino, U. Essmann, H. E. Stanley, *Nature* **1992**, 360, 324.
- [171] P. H. Poole, F. Sciortino, U. Essmann, H. E. Stanley, *Physical Review E* **1993**, 48, 3799.
- [172] S. Sastry, P. G. Debenedetti, F. Sciortino, H. E. Stanley, *Physical Review E* **1996**, 53, 6144.
- [173] P. A. Netz, F. W. Starr, H. E. Stanley, M. C. Barbosa, *The Journal of chemical physics* **2001**, 115, 344–348.
- [174] M. Yamada, S. Mossa, H. E. Stanley, F. Sciortino, *Physical review letters* **2002**, 88, 195701.
- [175] P. Gallo, M. Minozzi, M. Rovere, *Physical Review E* **2007**, 75, 011201.
- [176] T. Abbasi, S. Abbasi, *Journal of Loss Prevention in the Process Industries* **2007**, 20, 165–181.
- [177] A. Poulikkas, *Progress in Nuclear Energy* **2003**, 42, 3–10.
- [178] A. R. Imre, A. Baranyai, U. K. Deiters, P. T. Kiss, T. Kraska, S. Q. Cisneros, *International Journal of Thermophysics* **2013**, 34, 2053–2064.
- [179] T. Nakabaru, T. Hashimoto, S. Matsuo, T. Setoguchi, G. Rajesh, *Journal of Thermal Science* **2013**, 22, 209–215.
- [180] V. G. Baidakov, S. P. Protsenko, *High temperature* **2003**, 41, 195–200.
- [181] H. Stanley, C. Angell, U. Essmann, M. Hemmati, P. Poole, F. Sciortino, *Physica A: Statistical Mechanics and its Applications* **1994**, 205, 122–139.
- [182] A. R. Imre, T. Kraska, *Physica B: Condensed Matter* **2008**, 403, 3663–3666.
- [183] T. Kraska, F. Romer, A. Imre, *The Journal of Physical Chemistry B* **2009**, 113, 4688–4697.
- [184] L. Rayleigh, *The London Edinburgh and Dublin Philosophical Magazine and Journal of Science* **1892**, 33, 209–220.
- [185] E. A. Mastny, J. J. de Pablo, *The Journal of chemical physics* **2007**, 127, 104504.
- [186] J. Caillol, *The Journal of chemical physics* **1998**, 109, 4885–4893.
- [187] A. Rahman, *Physical Review* **1964**, 136, A405.
- [188] T. Bryk, A. Haymet, *Molecular Simulation* **2004**, 30, 131–135.
- [189] B. Guillot, Y. Guissani, *The Journal of Chemical Physics* **2001**, 114, 6720–6733.
- [190] P. J. in't Veld, A. E. Ismail, G. S. Grest, *The Journal of chemical physics* **2007**, 127, 144711.
- [191] S. Puchinskis, P. Skripov, *International journal of thermophysics* **2001**, 22, 1755–1768.
- [192] C. Kao, *Pharmacological reviews* **1966**, 18, 997–1049.
- [193] A.-G. Lee, *Nature* **1976**, 262, 545.
- [194] N. Franks, W. Lieb, *Nature* **1978**, 274, 339.
- [195] N. Franks, W. Lieb, *Nature* **1994**, 367, 607.
- [196] D. C. Mitchell, J. T. Lawrence, B. J. Litman, *Journal of Biological Chemistry* **1996**, 271, 19033–19036.

- [197] L. Mullins, *Chemical Reviews* **1954**, 54, 289–323.
- [198] S. M. Johnson, K. W. MILLER, *Nature* **1970**, 228, 75.
- [199] M. K. Jain, N. Y.-M. WU, L. V. Wray, *Nature* **1975**, 255, 494.
- [200] K. W. Miller, K.-Y. Y. Pang, *Nature* **1976**, 263, 253.
- [201] J. Boggs, T. Yoong, J. Hsia, *Molecular pharmacology* **1976**, 12, 127–135.
- [202] D. Haydon, B. Hendry, S. Levinson, J. Requena, *Nature* **1977**, 268, 356.
- [203] R. Ashcroft, H. Coster, J. Smith, *Nature* **1977**, 269, 819.
- [204] R. Ashcroft, H. Coster, J. Smith, *Biochimica et Biophysica Acta (BBA)-Biomembranes* **1977**, 469, 13–22.
- [205] J. Trudell, D. Payan, J. Chin, E. Cohen, *Proceedings of the National Academy of Sciences* **1975**, 72, 210–213.
- [206] B. J. Forrest, D. K. Rodham, *Biochimica et Biophysica Acta (BBA)-Biomembranes* **1985**, 814, 281–288.
- [207] P. Huang, E. Bertaccini, G. H. Loew, *Journal of Biomolecular Structure and Dynamics* **1995**, 12, 725–754.
- [208] K.-J. Oh, M. L. Klein, *Bulletin of the Korean Chemical Society* **2009**, 30, 2087–2092.
- [209] R. Reigada, *The Journal of Physical Chemistry B* **2011**, 115, 2527–2535.
- [210] Y. Moskovitz, H. Yang, *Soft matter* **2015**, 11, 2125–2138.
- [211] G. L. Turner, E. Oldfield, *Nature* **1979**, 277, 669–670.
- [212] N. Franks, W. Lieb, *Journal of molecular biology* **1979**, 133, 469–500.
- [213] J. L. Cascales, J. H. Cifre, J. G. de la Torre, et al., *J. Phys. Chem. B* **1998**, 102, 625–631.
- [214] K. Tu, M. Tarek, M. L. Klein, D. Scharf, *Biophysical journal* **1998**, 75, 2123–2134.
- [215] P.-L. Chau, P. Jedlovszky, P. Hoang, S. Picaud, *Journal of Molecular Liquids* **2009**, 147, 128–134.
- [216] J. Trudell, W. Hubbell, E. Cohen, *Biochimica et Biophysica Acta (BBA)-Biomembranes* **1973**, 291, 321–327.
- [217] L. Koubi, M. Tarek, M. L. Klein, D. Scharf, *Biophysical journal* **2000**, 78, 800–811.
- [218] R. D. Porasso, W. Drew Bennett, S. Oliveira-Costa, J. Lopez Cascales, *The Journal of Physical Chemistry B* **2009**, 113, 9988–9994.
- [219] J. Chen, L. Chen, Y. Wang, X. Wang, S. Zeng, *Scientific reports* **2015**, 5, 17235.
- [220] F. H. Johnson, E. A. Flagler, *Science* **1950**, 112, 91–92.
- [221] M. Lever, K. Miller, W. Paton, E. Smith, *Nature* **1971**, 231, 368.
- [222] M. Halsey, B. Wardley-Smith, *Nature* **1975**, 257, 811.
- [223] M. Darvas, P. N. Hoang, S. Picaud, M. Sega, P. Jedlovszky, *Physical Chemistry Chemical Physics* **2012**, 14, 12956–12969.
- [224] B. Fábíán, M. Darvas, S. Picaud, M. Sega, P. Jedlovszky, *Physical Chemistry Chemical Physics* **2015**, 17, 14750–14760.

- [225] B. Griepernau, R. A. Böckmann, *Biophysical journal* **2008**, *95*, 5766–5778.
- [226] J. F. Nagle, R. Zhang, S. Tristram-Nagle, W. Sun, H. I. Petrache, R. M. Suter, *Biophysical journal* **1996**, *70*, 1419–1431.
- [227] O. Berger, O. Edholm, F. Jähnig, *Biophysical journal* **1997**, *72*, 2002–2013.
- [228] S. Leekumjorn, A. K. Sum, *Biochimica et Biophysica Acta (BBA)-Biomembranes* **2007**, *1768*, 354–365.
- [229] L. D. Schuler, X. Daura, W. F. Van Gunsteren, *Journal of Computational Chemistry* **2001**, *22*, 1205–1218.
- [230] A. W. Schüttelkopf, D. M. Van Aalten, *Acta Crystallographica Section D: Biological Crystallography* **2004**, *60*, 1355–1363.
- [231] C. Oostenbrink, A. Villa, A. E. Mark, W. F. Van Gunsteren, *Journal of computational chemistry* **2004**, *25*, 1656–1676.
- [232] D. Scharf, K. Laasonen, *Chemical physics letters* **1996**, *258*, 276–282.
- [233] H. J. Berendsen, J. P. Postma, W. F. van Gunsteren, J. Hermans, **1981**, 331–342.
- [234] M. G. Alinchenko, A. V. Anikeenko, N. N. Medvedev, V. P. Voloshin, M. Mezei, P. Jedlovszky, *The Journal of Physical Chemistry B* **2004**, *108*, 19056–19067.
- [235] N. N. Medvedev, V. Voloshin, V. Luchnikov, M. L. Gavrilova, *Journal of computational chemistry* **2006**, *27*, 1676–1692.
- [236] N. Medvedev, V. Voloshin in *Voronoi Diagrams in Science and Engineering (ISVD)*, 2013 10th International Symposium on, IEEE, **2013**, pp. 89–90.
- [237] M. Mezei, *Molecular Simulation* **1988**, *1*, 327–332.
- [238] F. Aurenhammer, R. Klein, D.-T. Lee, *Voronoi diagrams and Delaunay triangulations*, World Scientific Publishing Company, **2013**.
- [239] F. Cazals, H. Kanhere, S. Lorient, *ACM Transactions on Mathematical Software (TOMS)* **2011**, *38*, 3.
- [240] J. Liang, H. Edelsbrunner, P. Fu, P. V. Sudhakar, S. Subramaniam, *Proteins: Structure Function and Bioinformatics* **1998**, *33*, 1–17.
- [241] S. Sastry, D. S. Corti, P. G. Debenedetti, F. H. Stillinger, *Physical Review E* **1997**, *56*, 5524.
- [242] V. Voloshin, A. V. Anikeenko, N. N. Medvedev, A. Geiger in *Voronoi Diagrams in Science and Engineering (ISVD)*, 2011 Eighth International Symposium on, IEEE, **2011**, pp. 170–176.
- [243] V. P. Voloshin, N. N. Medvedev, N. Smolin, A. Geiger, R. Winter, *Physical Chemistry Chemical Physics* **2015**, *17*, 8499–8508.
- [244] S. Marrink, R. Sok, H. Berendsen, *The Journal of chemical physics* **1996**, *104*, 9090–9099.
- [245] P. Jedlovszky, M. Mezei, *Journal of the American Chemical Society* **2000**, *122*, 5125–5131.

- [246] E. Falck, M. Patra, M. Karttunen, M. T. Hyvönen, I. Vattulainen, *The Journal of chemical physics* **2004**, *121*, 12676–12689.
- [247] M. Kupiainen, E. Falck, S. Ollila, P. Niemelä, A. Gurtovenko, M. Hyvönen, M. Patra, M. Karttunen, I. Vattulainen, *Journal of Computational and theoretical nanoscience* **2005**, *2*, 401–413.
- [248] P. Jedlovszky, M. Mezei, *The Journal of Chemical Physics* **1999**, *111*, 10770–10773.
- [249] P. Jedlovszky, M. Mezei, *The Journal of Physical Chemistry B* **2001**, *105*, 3614–3623.
- [250] M. Pickholz, L. Saiz, M. L. Klein, *Biophysical journal* **2005**, *88*, 1524–1534.
- [251] P. T. Ho, C. H. Townes, *Annual Review of Astronomy and Astrophysics* **1983**, *21*, 239–270.
- [252] S. K. Atreya, T. M. Donahue, W. R. Kuhn, *Science* **1978**, *201*, 611–613.
- [253] M. Meringer, H. J. Cleaves, S. J. Freeland, *Journal of chemical information and modeling* **2013**, *53*, 2851–2862.
- [254] J. I. Lunine, D. J. Stevenson, *Icarus* **1987**, *70*, 61–77.
- [255] O. Grasset, J. Pargamin, *Planetary and Space Science* **2005**, *53*, 371–384.
- [256] J. C. Cook, S. J. Desch, T. L. Roush, C. A. Trujillo, T. Geballe, *The Astrophysical Journal* **2007**, *663*, 1406.
- [257] A. Delsanti, F. Merlin, A. Guilbert-Lepoutre, J. Bauer, B. Yang, K. J. Meech, *Astronomy & Astrophysics* **2010**, *520*, A40.
- [258] D. C. Jewitt, J. Luu, *Nature* **2004**, *432*, 731.
- [259] K. Shin, R. Kumar, K. A. Udachin, S. Alavi, J. A. Ripmeester, *Proceedings of the National Academy of Sciences* **2012**, *109*, 14785–14790.
- [260] S. Alavi, K. Shin, J. A. Ripmeester, *Journal of Chemical & Engineering Data* **2014**, *60*, 389–397.
- [261] H. Tanaka, *The Journal of chemical physics* **1994**, *101*, 10833–10842.
- [262] H. Tanaka, *Fluid phase equilibria* **1998**, *144*, 361–368.
- [263] V. V. Sizov, E. M. Piotrovskaya, *The Journal of Physical Chemistry B* **2007**, *111*, 2886–2890.
- [264] S. Wierzchowski, P. Monson, *The Journal of Physical Chemistry B* **2007**, *111*, 7274–7282.
- [265] K. Katsumasa, K. Koga, H. Tanaka, *The Journal of chemical physics* **2007**, *127*, 044509.
- [266] N. Papadimitriou, I. Tsimpanogiannis, A. T. Papaioannou, A. Stubos, *The Journal of Physical Chemistry C* **2008**, *112*, 10294–10302.
- [267] S. Lectez, J.-M. Simon, O. Mousis, S. Picaud, K. Altwegg, M. Rubin, J. Salazar, *The Astrophysical Journal Letters* **2015**, *805*, L1.
- [268] F. Takeuchi, M. Hiratsuka, R. Ohmura, S. Alavi, A. K. Sum, K. Yasuoka, *The Journal of chemical physics* **2013**, *138*, 124504.
- [269] J. Abascal, E. Sanz, R. Garcia Fernandez, C. Vega, *The Journal of chemical physics* **2005**, *122*, 234511.

- [270] M. Conde, C. Vega, *The Journal of chemical physics* **2010**, *133*, 064507.
- [271] R. C. Rizzo, W. L. Jorgensen, *Journal of the American Chemical Society* **1999**, *121*, 4827–4836.
- [272] J. Barker, R. Watts, *Molecular Physics* **1973**, *26*, 789–792.
- [273] M. Neumann, *The Journal of chemical physics* **1985**, *82*, 5663–5672.
- [274] P. Jedlovszky, L. Pártay, P. N. Hoang, S. Picaud, P. von Hessberg, J. N. Crowley, *Journal of the American Chemical Society* **2006**, *128*, 15300–15309.
- [275] M. Darvas, J. Lasne, C. Laffon, P. Parent, S. Picaud, P. Jedlovszky, *Langmuir* **2012**, *28*, 4198–4207.
- [276] S. Picaud, P. Jedlovszky, *Chemical Physics Letters* **2014**, *600*, 73–78.
- [277] I. Sumi, B. Fábrián, S. Picaud, P. Jedlovszky, *The Journal of Physical Chemistry C* **2016**, *120*, 17386–17399.
- [278] M. Mezei, *Molecular Physics* **1987**, *61*, 565–582.
- [279] C. D. Daub, G. Patey, D. Jack, A. Sallabi, *The Journal of chemical physics* **2006**, *124*, 114706.
- [280] R. Radhakrishnan, B. L. Trout, *The Journal of chemical physics* **2002**, *117*, 1786–1796.
- [281] L. A. Baez, P. Clancy, *Annals of the New York Academy of Sciences* **1994**, *715*, 177–186.
- [282] P. Jedlovszky, L. B. Pártay, A. P. Bartók, G. Garberoglio, R. Vallauri, Structure of coexisting liquid phases of supercooled water: Analogy with ice polymorphs, **2007**.
- [283] P. Jedlovszky, L. B. Pártay, A. P. Bartók, V. P. Voloshin, N. N. Medvedev, G. Garberoglio, R. Vallauri, *The Journal of chemical physics* **2008**, *128*, 244503.
- [284] P. H. Handle, T. Loerting, F. Sciortino, *Proceedings of the National Academy of Sciences* **2017**, 201700103.
- [285] J. Brodholt, M. Sampoli, R. Vallauri, *Molecular Physics* **1995**, *86*, 149–158.
- [286] F. Martelli, S. Torquato, N. Giovambattista, R. Car, *Physical review letters* **2017**, *119*, 136002.
- [287] P. Gallo, K. Amann-Winkel, C. A. Angell, M. A. Anisimov, F. Caupin, C. Chakravarty, E. Lascaris, T. Loerting, A. Z. Panagiotopoulos, J. Russo, et al., *Chemical reviews* **2016**, *116*, 7463–7500.
- [288] J. Engstler, N. Giovambattista, *The Journal of chemical physics* **2017**, *147*, 074505.
- [289] C. Petuya, F. Damay, B. Chazallon, J.-L. Bruneel, A. Desmedt, *The Journal of Physical Chemistry C* **2017**.
- [290] A. Falenty, T. C. Hansen, W. F. Kuhs, *Nature* **2014**, *516*, 231.
- [291] G. McLaurin, K. Shin, S. Alavi, J. A. Ripmeester, *Angewandte Chemie* **2014**, *126*, 10597–10601.
- [292] O. Mousis, E. Chassefiere, N. G. Holm, A. Bouquet, J. H. Waite, W. D. Geppert, S. Picaud, Y. Aikawa, M. Ali-Dib, J.-L. Charlou, et al., *Astrobiology* **2015**, *15*, 308–326.
- [293] T. H. Vu, E. Gloesener, M. Choukroun, A. Ibourichene, R. Hodyss, *The Journal of Physical Chemistry B* **2014**, *118*, 13371–13377.

- [294] G. Tobie, J. I. Lunine, C. Sotin, *Nature* **2006**, *440*, 61.
- [295] J. R. Spencer, L. K. Tamppari, T. Z. Martin, L. D. Travis, *Science* **1999**, *284*, 1514–1516.